

Stream metabolism and groundwater discharge to coastal waters:  
Applications of the eddy correlation technique

Dirk Jacob Koopmans  
Charlottesville, Virginia

Master of Science, University of Georgia, 2000  
Bachelor of Science, Cornell University, 1995

A Dissertation presented to the Graduate Faculty  
of the University of Virginia in Candidacy for the Degree of  
Doctor of Philosophy

Department of Environmental Sciences

University of Virginia  
August, 2013

---

---

---

---

## **Abstract**

Inland waters receive over half of net terrestrial ecosystem production and respire or store most of this carbon en route to coastal oceans. To predict how these rates will change with climatic and land use changes improvements are needed in our ability to quantify the drivers of aquatic ecosystem metabolism and the contribution of groundwater to it. The techniques that have commonly been used to study aquatic metabolism and groundwater discharge at discrete spatial scales (tens of square meters or less) alter the in situ hydrodynamic environment and as a result incorporate biases in their measurements. With the eddy correlation technique, however, no alteration of the in situ hydrodynamic environment is made. Instead, the flux of a tracer across the sediment-water interface is determined from the turbulent fluctuation in tracer concentration and vertical velocity at a location in the water column.

Conventional seepage meters quantify groundwater discharge with polyethylene collection bags. Field and numerical tests demonstrated that the pressure required to introduce water causes the diversion of groundwater away from seepage meters under common operating conditions. By replacing collection bags with tubing through which the displacement of injected dye is measured, the diversion of groundwater was effectively eliminated. Additionally, dye displacement can be measured rapidly and in situ allowing for greater spatial and temporal resolution of groundwater discharge with a sensitivity to hydraulic gradients that is comparable to far more expensive automated seepage meters.

First order streams are the primary recipients of exported terrestrial production yet the drivers of metabolism within them are poorly quantified. Based on 103 days over which metabolic fluxes were quantified in a coastal, sand-bedded stream on the Eastern Shore of Virginia water velocity explained 90% of the variance in respiration prior to a stage-discharge shift and 96% of the variance in respiration after it. The effect of velocity on respiration rates was subject to strong site-specific control that was consistent with clogging of the hyporheic flow paths in which much of respiration in permeable sediments occurs. The combination of conventional and eddy correlation techniques allowed for a mechanistic investigation of the controls of stream respiration.

## Table of Contents

Abstract .....	ii
Acknowledgements .....	x
Chapter 1. Background and Guide to the Dissertation .....	1
Background .....	2
Objectives .....	7
Guide to the Dissertation .....	8
Literature Cited .....	10
Chapter 2. An Alternative to Traditional Seepage Meters: Dye Displacement .....	15
Abstract .....	16
Introduction .....	17
Methods .....	19
Pressure Required by Seepage Meter Bags .....	19
Pressure Required by Dye Displacement .....	21
Groundwater Diversion Model .....	23
Seepage Meter Design .....	25
Comparison of Seepage Meter Methods .....	27
Dye Displacement Measurement of Tidally-Forced SGD .....	28
Results .....	29

Pressure Required by Seepage Meter Bags .....	29
Pressure Required by Dye Displacement .....	30
Groundwater Diversion Model .....	31
Comparison of Seepage Meter Methods .....	35
Dye Displacement Measurement of Tidally-Forced SGD .....	36
Discussion .....	37
Summary .....	42
Literature Cited .....	43
Chapter 3. The Effect of Velocity on Ecosystem Metabolism in a Coastal Stream .....	58
Abstract .....	59
Introduction .....	60
Study Site .....	62
Methods .....	63
Physical and Chemical Characteristics .....	63
Dissolved Oxygen Flux .....	65
Metabolism Calculations .....	69
Results .....	71
Stream Attributes: Physical and Chemical .....	71
Stream Attributes with Stage .....	73

Variation in Metabolism on Diurnal Time-Scales.....	74
Variation in Metabolism on Seasonal Time-Scales.....	76
Variation in Metabolism with Stage Shift .....	77
Drivers of Metabolism.....	79
Discussion .....	81
Stream Attributes: Physical and Chemical Parameters .....	81
Stream Attributes with Stage .....	82
Determination of Metabolic Rates.....	84
Variation in Metabolism on Diurnal Time-Scales.....	85
Variation in Metabolism on Seasonal Time-Scales.....	86
Significance of NEM .....	88
Drivers of GPP.....	88
Drivers of Respiration .....	89
Synthesis.....	92
Literature Cited .....	93
Chapter 4. Spatial Variability in Oxygen Flux in a Coastal Stream: An Application of the Eddy Correlation Technique .....	108
Abstract .....	109
Introduction .....	110

Study Site.....	115
Methods.....	116
Data Collection .....	116
Physical and Chemical Characteristics.....	117
Oxygen Flux .....	119
Technique Footprints.....	122
Results .....	123
Physical and Chemical Characteristics.....	123
Spatial Scale of Measurement .....	124
Comparison of Reach and Site Scales .....	125
Site Specific Differences in Oxygen Flux .....	127
Confirmation of Hyporheic Oxygen Consumption .....	129
Elevated Daytime Respiration .....	130
Discussion .....	131
Suitability for Hyporheic Exchange .....	131
Comparison of Reach and Site Scales .....	132
Site-Specific Differences in Oxygen Flux.....	135
Elevated Daytime Respiration .....	138
Summary .....	139

Literature Cited .....	141
Conclusion and Synthesis .....	157
Appendix I. Identification of Groundwater Discharge to Ramshorn Channel, Hog Island Bay, and Cobb Bay by Radon Mapping .....	168
Overview .....	169
Study Site .....	170
Methods .....	171
Observations and Discussion .....	175
Literature Cited .....	179
Appendix II. Groundwater Discharge to a Coastal Stream Determined from a Heat Balance: An Application of the Eddy Correlation Technique .....	183
Overview .....	184
Methods .....	185
Observations and Discussion .....	185
Appendix III. Oxygen Exchange and Ice Melt Measured at the Ice-Water Interface by Eddy Correlation .....	195
Attribution .....	196
Abstract .....	197
Introduction .....	198



Methods .....	201
Site Description .....	201
Eddy Correlation Measurements .....	201
Data Analysis .....	202
Results .....	205
Discussion .....	209
Acknowledgments .....	216
Literature Cited .....	217

## **Acknowledgements**

My research was funded in large part by the Virginia Coast Reserve Long Term Ecological Research program but also by the Department of Environmental Sciences and the Graduate School of Arts and Sciences. I thank each of them for the opportunity to conduct this research. I applied to the Ph.D. program in Environmental Sciences at the University of Virginia after meeting Peter Berg in the summer of 2005. While testing different settings for a component of the eddy correlation system he asked me if I liked to play with scientific equipment. From that day on he has encouraged me to bring expensive equipment into rough waters. I'm grateful for those opportunities. I'm also grateful to him for the countless conversations as well as the tremendous amount of time, thoughtfulness, and resources that he has dedicated not only to my research but to my success.

I thank the faculty of the Department of Environmental Sciences, and my advisory committee members, Karen McGlathery, Patricia Wiberg, Todd Scanlon, Aaron Mills, Mike Pace, and Winston Lung for their open doors, engagement in my research, and guidance. Faculty members in the department have been mentors for research and also mentors for teaching, and I am grateful to have been supported in developing those skills. Outside the department I also thank Roland Simon for stepping in and serving as the Graduate School Dean's representative for my dissertation defense.

I am grateful to Art Schwarzschild at the Anheuser Busch Coastal Research Center for providing logistical support at the shore, including generously lending me his own car when mine was in the shop. I also thank David Boyd and Chris Buck for piloting

boat trips and providing research support early on in my dissertation work. An additional thank you goes to the whole crew there, including Donna Fauber, Sherry and Leo for making the ABCRC a home for students who stay there.

I owe a big thanks to Soeren Rysgaard and Ronnie Glud, both with co-appointments at the Greenland Climate Research Center, for seeing the potential in the eddy correlation technique at determining ice melt rates in situ. The food, the camaraderie, and the northern lights in Greenland were terrific.

Thank you to friends, housemates, graduate students in the department, and all of the above. You've been my life here. It'll be hard to move on. And finally, thank you and my love to my family for supporting me wholeheartedly in this and in so many things in life.

## Chapter 1

### Background and Guide to the Dissertation

## **Background**

This dissertation quantifies fluxes of groundwater to coastal waters and fluxes of oxygen across the sediment-water interface in a coastal stream. The two fluxes are related. As fertilizer usage increased in the United States between 1945 and 2002, the residual nitrate concentration in surficial aquifers in agricultural areas increased from 150  $\mu\text{M}$  to 1 mM (Puckett et al., 2010). The discharge of this nitrogen rich groundwater to rivers, lakes and coastal waters is a cause of eutrophication, an enhancement in the growth of primary producers that are capable of taking advantage of nutrient addition (Ryther and Dunstan, 1971). The natural fixation of nitrogen in freshwaters by cyanobacteria makes phosphorus, which cannot be fixed from the atmosphere, the nutrient which limits primary production in freshwater systems over long, i.e. multi-year, time scales (Schindler, 1977). However, freshwater systems also experience nitrogen limitation (Downing and McCauley, 1992), and the best predictors of eutrophication of stream ecosystems incorporate both nitrogen and phosphorus concentrations (Dodds et al., 2002; Biggs, 2000). As a consequence of the increase in photosynthetic production due to nitrogen addition, the enhanced production of organic matter also sustains greater rates of organic matter respiration in aquatic ecosystems (Schelske and Hodell, 1995; Zimmerman and Canuel, 2000). By these mechanisms groundwater discharge to coastal and freshwater systems is linked to the rates of photosynthesis and respiration that are observed there.

In locations where photosynthesis is limited by nutrient availability and groundwater contributions are substantial, nitrogen addition by groundwater discharge

may significantly alter ecosystem metabolism. As nitrogen and organic matter concentrations in stream waters increase, the efficiency of the natural processes of nitrogen removal in stream ecosystems declines, with the result that a greater proportion of added nitrogen flows to downstream waters (Mulholland et al., 2008). In coastal waters eutrophication is a cause of hypoxia and associated with losses of a wide range of species including seagrasses and subsequent habitat losses in coastal bays in New England (Valiela et al., 1992) and the Chesapeake Bay (Boesch et al., 2001). More pervasive hypoxic events have led to the losses of a wide range of commercially important fisheries in the Gulf of Mexico (Rabalais et al., 2002) and in the Chesapeake Bay (Kemp et al., 2005) among many other locations.

While stream metabolism has important ramifications for nutrient transport to downstream waters it also has ramifications for the carbon balance of terrestrial ecosystems. Inland waters were, until recently, viewed as passive pipes in which the carbon that they delivered to the coastal oceans equaled the carbon that they received from terrestrial ecosystems (Cole et al., 2007). Instead, inland waters play an active role in the global carbon cycle, receiving half or more of net terrestrial ecosystem production and mineralizing or storing half of that carbon during transport to the open ocean (Cole et al., 2007; Aufdenkampe et al., 2011). Because of this role terrestrial ecosystems which had been believed to be atmospheric carbon sinks may, in fact, be net carbon sources to the atmosphere when the mineralization of carbon in inland waters is taken into account (Aufdenkampe et al., 2011). Inland waters are now considered by those investigating landscape scale carbon budgets (e.g., Luyssaert et al. 2010).

For determining rates of both groundwater discharge and aquatic ecosystem metabolism standard techniques often employ a mean constituent concentration in surface waters to derive the relevant flux at temporal and spatial scales equivalent to those at which the mixing of surface water occurs. These techniques allow for the determination of broad patterns of geochemically and ecologically relevant processes. Examples includes the discovery from radium activity in surface waters of the South Atlantic Bight that brackish groundwater discharge amounts to 40% the volume of river flow to the area (Moore, 1996), or the discovery from the mean concentration of oxygen over kilometer-scale reaches in streams that they are among the most biologically productive environments on earth (Odum, 1956). But to quantify the drivers of geochemically and ecologically relevant processes in each environment may require analysis at a finer spatial scale, on the order of meters.

Groundwater discharge to coastal zones is temporally and spatially complex. Two examples of fine temporal and spatial scale control of groundwater discharge are in beach surf zones and salt marshes. Waves generate a recirculation cell of sea water within beach sands at the scale of a few meters (Gourlay, 1992; Xin 2010). Changes in tidal height also circulate seawater through beach sands at a similar spatial scale (Robinson et al., 2007). As a result of these drivers the maximum rate of recirculated seawater discharge occurs just below the exposed beach face and at a maximum rate close after low tide. Terrestrial groundwater discharge is typically displaced by this recirculation of seawater and discharges within a few meters offshore of it (Robinson et al., 2007). In salt marsh tidal creeks waves typically have little effect on groundwater discharge, however the

differences in sediment hydraulic conductivity between the rooting zone, marsh deposits, and the silt, sand, and shell deposits that lie beneath them can span three orders of magnitude or more (Harvey and Odum, 1990). As a result, tidally-driven recirculated seawater discharge may occur irregularly at locations where the more conductive deposits are exposed, such as at the base of portions of tidal creeks (Krest et al., 2000).

Complicating a determination of nutrient loading to coastal ecosystems by groundwater discharge is the high variability in groundwater pollution and the microbially-mediated removal of nitrogen in aquifers and sediments prior to discharge. On the Eastern Shore of Virginia the median concentration of nitrate in surficial aquifers beneath forests was 40  $\mu\text{M}$  ( $n = 111$  wells) in 1993, but beneath agricultural areas it was 580  $\mu\text{M}$  ( $n = 185$ ; Hamilton and Helsel, 1995). Efficient removal of agricultural nitrogen by denitrification may occur in aquifers en route to surface waters (Bottcher et al., 1990) and in submarine sediments prior to discharge (Slater and Capone, 1987). In sandy coastal stream sediments on the Eastern Shore denitrification removed 93% of nitrate in groundwater at a discharge rate of 40  $\text{cm d}^{-1}$ , but at a rate of 80  $\text{cm d}^{-1}$  the removal efficiency dropped to 63% (Gu et al., 2007). As a result, groundwater nitrate loads to surface waters may vary over orders of magnitude at spatial scale of meters, as occurs in Cherrystone Inlet, VA (Reay and Gallagher, 1992). A better understanding of the fine scale drivers of groundwater discharge would improve prediction of the contribution of groundwater to the pollution of surface waters.

Similarly, oxygen flux in freshwater ecosystems may also be driven by processes which act at fine spatial and temporal scales. In stream ecosystems both hyporheic



exchange and light availability are examples of this. Hyporheic exchange is the velocity-driven flow of surface waters through hydraulically conductive sediments before returning to the stream. Where alluvial sediments are permeable hyporheic exchange may be the primary mechanism for the respiration of organic matter (e.g. Grimm and Fisher 1985; Fuss and Smock, 1996). This is because advective flow through permeable sediments can act as both a source of oxygen and carbon to pore waters, making permeable sediments a biocatalytic filter for stream organic material (Huettel et al, 2003; Glud, 2008). As the morphology and hydraulic conductivity of alluvial sediments varies over riffle, pool, and run spatial scales (where present) oxygen flux across the sediment water interface may also vary at these scales. Pusch, (1996) using flow-through chambers submerged in riverine sediment demonstrated that oxygen consumption was twice as great in stream riffles than in pools. Spatial and temporal variation in light availability in streams is also substantial, with rapid changes that occur with the progression of patches of sunlight through a forest canopy over a stream. However, despite the high spatial heterogeneity in stream ecosystems, prior to the development of the eddy correlation technique (Berg et al., 2003) the availability of methods for investigating metabolic processes at discrete spatial scales (tens of square meters or less) were limited to enclosure studies.

To investigate the high spatial and temporal variation in both groundwater discharge and oxygen flux chambers are typically used. In studies of groundwater discharge seepage meters fitted with bags to collect inflowing groundwater are used (Lee, 1977). In studies of aquatic metabolism chambers are generally placed on the sediment

surface or are filled with the elements of the microenvironment of interest (e.g., Pusch and Schwoerbel, 1994). In both cases, however, the walls of the chamber or seepage meter interfere with ambient flow. The design of these instruments can be optimized to reduce the divergence of groundwater they may cause, or to reproduce in situ flows in benthic chambers, but a technique which is capable of resolving fluxes under in situ hydrodynamic conditions offers an advantage.

## **Objectives**

The overall objective of my research was to investigate the applicability of new technologies to the quantification of the drivers of groundwater discharge to coastal waters and of aquatic ecosystem metabolism in a coastal stream.

Specific objectives include:

1. To identify locations of groundwater discharge to coastal bays of the Virginia Coast Reserve Long Term Ecological Research site as locations for future study.
2. To investigate errors associated with the deployment of conventional groundwater seepage meters in rivers in order to develop a seepage meter that would be highly sensitive to in situ hydrodynamic conditions.
3. To quantify a heat budget at the sediment water interface of a coastal stream, to investigate the potential for quantification of groundwater discharge without seepage meters using the eddy correlation technique.

4. To quantify diurnal and seasonal variation in the drivers of metabolism in a coastal stream at a reach scale (hundreds of meters) with the conventional open water technique.

5. To quantify fine-spatial and temporal scale variation in the drivers of oxygen flux across the sediment water interface of a coastal stream with the eddy correlation technique.

### **Guide to the Dissertation**

The portions of this dissertation devoted to investigations of groundwater constitute Chapter 2, Appendix I, and Appendix II. The study of the hydraulic pressures at which conventional, bag-equipped seepage meters operate, and a modification of that design to make them more sensitive to in situ hydraulic gradients was published in the journal *Water Resources Research* and is presented in Chapter 2. The spatial extent of groundwater discharge to the coastal lagoons of the Virginia Coast Reserve Long Term Ecological Research site was investigated using radon as a groundwater tracer. Locations where radon activities were substantially in excess of other known sources are reported as likely locations of groundwater discharge in Appendix I. A novel application of the eddy correlation technique to determine fresh groundwater fluxes to a coastal stream from a heat flux balance is presented in Appendix II.

Oxygen fluxes in a coastal stream ecosystem were quantified using the conventional open water technique and the eddy correlation technique over the course of two years of field work. Investigations of the drivers of metabolism at the reach scale

using the conventional open water technique are presented in Chapter 3. Investigations of the drivers of oxygen fluxes across the sediment water interface using the eddy correlation technique are presented in Chapter 4.

Appendix III presents an exception to the objectives laid out in my dissertation. The eddy correlation technique can be employed to quantify turbulent fluxes of heat and salt over any boundary in aquatic environments. An aquatic environment in which fluxes of heat and salt are specifically relevant is in the melting and formation of sea ice. The method used to quantify groundwater discharge by a heat and salt budget using the eddy correlation technique was applied to determining a heat and salt budget at the ice water interface. The work was co-sponsored by my advisor and the Greenland Climate Research Center.

## Literature Cited

- Aufdenkampe AK, Mayorga E, Raymond PA, Melack JM, Doney SC, Alin SR, Aalto RE, Yoo K. 2011. Riverine coupling of biogeochemical cycles between land, oceans, and atmosphere. *Frontiers in Ecology and the Environment* 9:53–60.
- Berg P, Røy H, Janssen F, Meyer V, Jørgensen BB, Huettel M, De Beer D. 2003. Oxygen uptake by aquatic sediments measured with a novel non-invasive eddy-correlation technique. *Marine Ecology Progress Series* 261:75–83.
- Biggs BJ. 2000. Eutrophication of streams and rivers: dissolved nutrient-chlorophyll relationships for benthic algae. *Journal of the North American Benthological Society* 19:17–31.
- Boesch DF, Brinsfield RB, Magnien RE. 2001. Chesapeake Bay eutrophication. *Journal of Environmental Quality* 30:303–20.
- Böttcher J, Strebel O, Voerkelius S, Schmidt H-L. 1990. Using isotope fractionation of nitrate-nitrogen and nitrate-oxygen for evaluation of microbial denitrification in a sandy aquifer. *Journal of Hydrology* 114:413–24.
- Cole JJ, Prairie YT, Caraco NF, McDowell WH, Tranvik LJ, Striegl RG, Duarte CM, Kortelainen P, Downing JA, Middelburg JJ, Melack J. 2007. Plumbing the Global Carbon Cycle: Integrating Inland Waters into the Terrestrial Carbon Budget. *Ecosystems* 10:172–85.
- Dodds WK, Smith VH, Lohman K. 2002. Nitrogen and phosphorus relationships to benthic algal biomass in temperate streams. *Canadian Journal of Fisheries and Aquatic Sciences* 59:865–74.

- Downing JA, McCauley E. 1992. The nitrogen: phosphorus relationship in lakes. *Limnology and Oceanography* 37:936–45.
- Fuss C, Smock L. 1996. Spatial and temporal variation of microbial respiration rates in a blackwater stream. *Freshwater Biology* 36:339–49.
- Glud RN. 2008. Oxygen dynamics of marine sediments. *Marine Biology Research* 4:243–89.
- Gourlay MR. 1992. Wave set-up, wave run-up and beach water table: Interaction between surf zone hydraulics and groundwater hydraulics. *Coastal engineering* 17:93–144.
- Grimm NB, Fisher SG. 1984. Exchange between interstitial and surface water: implications for stream metabolism and nutrient cycling. *Hydrobiologia* 111:219–28.
- Gu C, Hornberger GM, Mills AL, Herman JS, Flewelling SA. 2007. Nitrate reduction in streambed sediments: Effects of flow and biogeochemical kinetics. *Water Resources Research* 43.
- Hamilton PA, Helsel DR. 1995. Effects of Agriculture on Ground-Water Quality in Five Regions of the United States. *Ground Water* 33:217–26.
- Harvey JW, Odum WE. 1999. The influence of tidal marshes on upland groundwater discharge to estuaries. *Biodegradation* 10:217–36.
- Huettel M, Røy H, Precht E, Ehrenhauss S. 2003. Hydrodynamical impact on biogeochemical processes in aquatic sediments. In: *The Interactions between Sediments and Water*. Springer. pp 231–6.

- Kemp WM, Boynton WR, Adolf JE, Boesch DF, Boicourt WC, Brush G, Cornwell JC, Fisher TR, Glibert PM, Hagy JD. 2005. Eutrophication of Chesapeake Bay: historical trends and ecological interactions. *Marine Ecology Progress Series* 303:1–29.
- Krest JM, Moore WS, Gardner LR, Morris JT. 2000. Marsh nutrient export supplied by groundwater discharge: Evidence from radium measurements. *Global Biogeochemical Cycles* 14:167–76.
- Luyssaert S, Ciais P, Piao SL, Schulze ED, Jung M, Zaehle S, Schelhaas MJ, Reichstein M, Churkina G, Papale D. 2010. The European carbon balance. Part 3: forests. *Global Change Biology* 16:1429–50.
- Moore WS. 1996. Large groundwater inputs to coastal waters revealed by  $^{226}\text{Ra}$  enrichments. *Nature* 380:612–4.
- Mulholland PJ, Helton AM, Poole GC, Hall RO, Hamilton SK, Peterson BJ, Tank JL, Ashkenas LR, Cooper LW, Dahm CN. 2008. Stream denitrification across biomes and its response to anthropogenic nitrate loading. *Nature* 452:202–5.
- Odum HT. 1956. Primary production in flowing waters. *Limnology and oceanography*:102–17.
- Puckett LJ, Tesoriero AJ, Dubrovsky NM. 2010. Nitrogen Contamination of Surficial Aquifers—A Growing Legacy†. *Environmental science & technology* 45:839–44.
- Pusch M. 1996. The metabolism of organic matter in the hyporheic zone of a mountain stream, and its spatial distribution. *Hydrobiologia* 323:107–18.

- Pusch, M., Schwoerbel, J. 1994. Community respiration in hyporheic sediments of a mountain stream (Steina, Black Forest). *Archiv für Hydrobiologie*:35–52.
- Rabalais NN, Turner RE, Wiseman Jr WJ. 2002. Gulf of Mexico hypoxia, AKA ‘ The dead zone’. *Annual Review of ecology and Systematics*:235–63.
- Reay WG, Gallagher DL, Simmons GM. 1992. Groundwater discharge and its impact on surface water in a Chesapeake Bay inlet. *JAWRA Journal of the American Water Resources Association* 28:1121–34.
- Robinson C, Li L, Barry DA. 2007 a. Effect of tidal forcing on a subterranean estuary. *Advances in Water Resources* 30:851–65.
- Robinson C, Li L, Prommer H. 2007 b. Tide-induced recirculation across the aquifer-ocean interface. *Water Resources Research* 43.
- Ryther JH, Dunstan WM. 1971. Nitrogen, phosphorus, and eutrophication in the coastal marine environment. *Science* 171:1008–13.
- Schelske CL, Hodell DA. 1995. Using Carbon Isotopes of Bulk Sedimentary Organic Matter to Reconstruct the History of Nutrient Loading and Eutrophication in Lake Erie. *Limnology and Oceanography* 40:918–29.
- Schindler DW. 1977. Evolution of phosphorus limitation in lakes. *Science* 195:260–2.
- Slater JM, Capone DG. 1987. Denitrification in aquifer soil and nearshore marine sediments influenced by groundwater nitrate. *Applied and environmental microbiology* 53:1292–7.
- Valiela I, Foreman K, LaMontagne M, Hersh D, Costa J, Peckol P, DeMeo-Andreson B, D’Avanzo C, Babione M, Sham C-H. 1992. Couplings of watersheds and coastal



waters: sources and consequences of nutrient enrichment in Waquoit Bay, Massachusetts. *Estuaries* 15:443–57.

Xin P, Robinson C, Li L, Barry DA, Bakhtyar R. 2010. Effects of wave forcing on a subterranean estuary. *Water Resources Research* 46.

Zimmerman AR, Canuel EA. 2000. A geochemical record of eutrophication and anoxia in Chesapeake Bay sediments: anthropogenic influence on organic matter composition. *Marine Chemistry* 69:117–37.

## Chapter 2

An Alternative to Traditional Seepage Meters: Dye Displacement

Koopmans, D., and Berg, P.

Published in the journal *Water Resources Research*

2011, V. 47

doi: 10.1029/2010WR009113

**Abstract**

A new seepage meter design that increases sensitivity to the small hydraulic gradients that drive submarine groundwater discharge was developed as an inexpensive alternative to traditional seepage meters. The new design replaces seepage meter bags with open-ended tubing through which the displacement of injected dye is a highly reproducible measure of discharge. Laboratory measurements, detailed mathematical modeling of ground water flow around seepage meters, and parallel field tests of bag and dye displacement seepage meters demonstrated that the new design can improve the precision and temporal resolution of submarine groundwater discharge measurement. In parallel field tests, groundwater discharge to 15-cm-diameter, bag-equipped seepage meters was half of the discharge to adjacent 15-cm-diameter dye displacement seepage meters. Model results confirm that similar discrepancies, caused by groundwater diversion around bag-equipped seepage meters, may occur during the deployment of 57-cm-diameter seepage meters in common field conditions. A second field deployment of 15-cm-diameter dye displacement seepage meters showed saline inflow into sandy sediments at high tide, and a high rate of discharge at low tide, similar to observations made with far more expensive, open flow-path automated seepage meters in other studies.

## **Introduction**

Submarine groundwater discharge (SGD) is fluid of terrestrial, marine, or mixed origins, that flows out of sediment pore spaces into overlying seawater (Burnett et al., 2003). In coastal waters this flow is driven by many factors including the hydraulic gradient between terrestrial aquifers and bottom water, tidal pumping, density-driven displacement of pore waters, and sediment compaction. It is a source of biologically and geochemically important compounds to seawater, as well as a driver of biologically and geochemically important processes in sediments (Riedl et al., 1972; Bokuniewicz, 1980; Simmons, 1992; Moore, 1999).

There are several approaches to determining rates of SGD. These include methods that rely on terrestrial water budgets and hydraulic gradients (both reviewed by Burnett et al., 2001), geochemical tracers (e.g., Moore, 1996), vertical profiles of tracers (such as temperature) in sediments (Taniguchi et al., 2003), eddy correlation (Crusius et al., 2008), and seepage meters (Lee, 1977). A seepage meter typically consists of a 55-gallon drum-end which is inserted into the sediment. As groundwater flows into the device, it is collected in an attached bag and later quantified. The seepage meter is a valuable and well-tested approach that has been extensively used for many years, but there are methodological problems with manually operated seepage meters and the bags they use. Empty 3.8 L polyethylene bags mechanically relax in water and may draw in 300 mL of surrounding water when submerged (Shaw and Prepas, 1990). In addition, the walls of polyethylene bags will exert a slight resistance to push or pull, requiring pressure for inflow and outflow. In highly permeable sediments this pressure cannot be neglected

relative to the pressure that is capable of diverting a fraction of the groundwater flow around the seepage meter, biasing the measured seepage rate (Murdoch and Kelly, 2003). Additionally, currents flowing across seepage meter bags can cause spurious SGD measurements, as flowing water outside of seepage meter bags may exert a suction or pressure on the walls of the bag (Libelo and MacIntyre, 1994). The errors due to these problems may be small in low-current environments with SGD greater than 2 cm/d (Cable, 2006).

Automated seepage meters use mechanical, electronic, or osmotic devices to quantify SGD in place of seepage meter bags. Automated seepage meters typically give more reproducible measurements of low rates of SGD than manual seepage meters with bags. Heat pulse and continuous heat flow (Taniguchi and Fukuo, 1993; Taniguchi and Iwakawa, 2001), ultrasonic (Paulsen et al., 2001), dye-partitioning (Tryon et al., 2001), dye-dilution (Sholkovitz et al., 2003), and electromagnetic seepage meters (Rosenberry and Morin, 2004) have shown the capacity to measure not only low rates of SGD ( $< 2$  cm/d) but in some cases also the inflow of overlying water to submarine sediments. Despite their advantages, the cost of automated seepage meters typically restricts their use to the deployment of one, or a few, at a time. The common trait that gives automated seepage meters improved sensitivity over manual seepage meters with bags is that they are designed with open flow-path detection systems with minimal physical restriction on flow into or out of the seepage meter.

To obtain similar performance for manually operated seepage meters we developed and tested a new and inexpensive open flow-path seepage meter concept based

on dye injected into a clear open-ended plastic-tube (Figure 1). In lab measurements we determined the pressure required to generate flow through the tube and, at an SGD rate of 10 cm/d, found it to be an order of magnitude smaller than that required to introduce water to a polyethylene bag. A two-dimensional model in cylindrical coordinates was developed to describe the Darcy-flow into and around seepage meters and predict the diversion of groundwater as a function of the pressure associated with the seepage meter measurement system. The new dye displacement design was field-tested alongside bag-equipped seepage meters at a Chesapeake Bay beach. The dye displacement seepage meters allowed for quantification of SGD, and also inflow of overlying water into sediments, at a higher temporal resolution and precision than traditional seepage meters.

## **Methods**

### *Pressure Required by Seepage Meter Bags*

As a reference point for our dye displacement design we determined the pressure required to introduce water into three types of bags commonly used on traditional seepage meters. These bags are: 1) 3.8 L twist-tie bags (Guaranteed Value™ Gallon Storage Bags, available at Giant® Food Stores) made from 25  $\mu\text{m}$ -thick polyethylene; 2) 3.8 L press-seal bags (Ziploc® Double Zipper Storage Bags) made from 100  $\mu\text{m}$ -thick polyethylene; and 3) condoms (LifeStyles®) made from 65  $\mu\text{m}$ -thick latex. Gallon-sized (3.8 L) polyethylene bags are commonly attached to 57-cm-diameter seepage meters to capture SGD in nearshore waters (e.g., Cable, 2006), while condoms are commonly

attached to 10-cm-diameter seepage meters, or smaller, to capture groundwater discharge in rivers (e.g., Fryar et al., 2000). Both bags and condoms were submerged in a water tank, air bubbles were removed, and then they were attached to a 1 m-long, 0.95 cm inner diameter (i.d.) PVC inlet tube. The open end of the twist-tie bag and the condom were collapsed around the inlet tube and tied water-tight, creating folds in the walls of the bag. The seal of the press-seal bag was closed and the bag was attached to the inlet tube through a barbed fitting placed in an inside corner of the bag, minimizing folds in the walls of the bag. The opposite end of the water-filled inlet tube was mounted beside the tank so that the pressure within the submerged bag could be read as a water height in the tube outside the tank. With a second similarly mounted tube, the hydrostatic pressure of the tank could also be read. The bags were incrementally filled by adding water through the inlet tube to imitate gradual filling during a seepage meter deployment. The pressure required to introduce water to the seepage meter bag was the water height in the inlet tube minus the water height in the reference tube. To improve precision, 1.8 cm i.d. borosilicate glass tubes replaced PVC tubing at the point of measurement, at the test tank water level. The borosilicate glass minimized capillary effects and magnified an attached 0.5 mm graded ruler allowing a resolution of less than 0.2 mm-H<sub>2</sub>O. For each type of collection bag, five identical trials, or filling sequences were performed with a minimum of three different bags in order to test the reproducibility of the observed pressure differences.

### *Pressure Required by Dye Displacement*

The pressure required to force SGD into dye displacement seepage meters is given by the friction of laminar flow against the walls of the dye displacement tubing. This pressure was measured at different flow rates in the laboratory by generating steady, laminar flow through 2.2 m of a 0.95 cm i.d. flexible PVC tube. Measurements were made of the pressure loss as a change in water height in attached tubes at the tube inflow and the tube outflow. The length of tubing used was greater than that used in field deployments of dye displacement seepage meters to more accurately quantify pressure differences. Laminar flows up to 130 cm<sup>3</sup>/min were applied to generate pressure differences large enough to be consistently read. The observed pressure loss for laminar flow through PVC tubing was compared to the pressure loss predicted by Poiseuille's (1846) equation for laminar discharge through smooth pipes,

$$\Delta P = \frac{8\mu QL}{\pi R^4} \quad (1)$$

where  $\Delta P$  is the pressure drop over the length of the tube,  $\mu$  is the dynamic viscosity evaluated at the temperature of the flowing water (20°C),  $Q$  is the volume discharge,  $L$  is the length of the tube, and  $R$  is the inner radius of the tube.

The laminar displacement of dye along the centerline of a tube connected to a seepage meter can be used as an effective measure of discharge. For laminar flows through pipes or tubes, friction with the wall creates a parabolic velocity profile, with the maximum velocity along the centerline of the tube, and zero velocity at the wall (Kundu



and Cohen, 2004). The velocity profile of laminar flow through a tube, integrated over the cross-section, gives the volume discharge

$$Q = \frac{\pi R^2 V_{\max}}{2} \quad (2)$$

where  $V_{\max}$  is the centerline velocity. To determine the rate of SGD to the seepage meter the volume discharge is divided by the area of the seepage meter. The precision of this approach was investigated in controlled laboratory trials. Continuous discharge at a range of 0.25 to 5 cm<sup>3</sup>/min was generated in a 2.2 m-long 0.95 cm i.d. tube. These flow rates correspond to 2 to 40 cm/d of SGD to a 15-cm-diameter seepage meter. A 2.5% solution of Rhodamine WT dye (Bright Dyes® Liquid Red FWT 25, Kingscote Chemicals), with density reduced to 1.0 g/cm<sup>3</sup> with methanol to match the density of pure water, was injected in the upstream end of the tube. The displacement of the leading edge of dye along the centerline was measured at time intervals of three to eight minutes, depending on the discharge rate, giving three or four successive dye displacement measurements for every injection. Discharge from the tube was concurrently collected to determine the actual discharge rate. Centerline dye travel time and distance were used to quantify discharge through the tube according to equation (2). The maximum dye travel time through the tube was 32 minutes, and maximum total distance was 130 cm. Successive measurements were made to examine how the reproducibility of the dye displacement method was affected by travel time and distance.

### *Groundwater Diversion Model*

To determine if the pressure required to introduce water into a seepage meter bag or a dye displacement tube could divert groundwater, we developed a two-dimensional model of the ground water flow into and around seepage meters. Cylindrical coordinates were used to take advantage of the symmetry around the central, vertical axis of the seepage meter (Figure 2). By combining Darcy's Law and a mass balance for water we obtained the equation

$$\frac{1}{r} \frac{\partial}{\partial r} \left( rK \frac{\partial h}{\partial r} \right) + \frac{\partial}{\partial z} K \frac{\partial h}{\partial z} = 0 \quad (3)$$

where  $r$  is radial distance,  $K$  is hydraulic conductivity,  $h$  is hydraulic head, and  $z$  is depth. The equation was discretized following a control volume approach (Patankar, 1980) and solved using MATLAB® computational software.

The horizontal extent of the calculation domain was to a distance of five times the seepage meter radius (Figure 2). Similarly, the vertical extent was to a depth of five times the penetration depth of the seepage meter, which was assumed to be equal to its radius. The boundary conditions imposed in the model (Figure 2) allowed no flow into or out of the model domain through the inner or outer vertical boundaries, and no flow was allowed across the seepage meter wall. Known, uniform, upward-directed SGD was imposed through the lower boundary. A pressure was imposed at the upper boundary inside the seepage meter ( $p_{\text{seep}}$  in Figure 2) according to the results of laboratory testing of seepage meter bags and dye displacement tubing. Outside the seepage meter the pressure

at the upper boundary was set to zero. The hydraulic conductivity of sediments did not vary in  $z$  or  $r$  directions. The model domain was separated into 40000 (200 x 200) equally sized control volumes.

The model, the appropriate location of the boundaries, and the control volume size were tested as follows. To confirm that mass was conserved as expressed in equation (3), it was confirmed that the integration of the imposed inflow along the bottom boundary exactly matched the integration of the calculated outflow along the top boundary. The latter included both the seepage meter and the adjacent free surface (Figure 2). Further, the boundary conditions were temporarily manipulated in two separate tests to give one-dimensional flows, first along  $r$  axis and then along  $z$  axis. For each of these unidirectional flows, analytical solutions exist and exactly matched the model results. Tests incorporating greater control volume density and model domain size yielded small changes in model results, indicating that the model was adequately dimensioned.

For the model analysis groundwater discharge through the base of the domain was varied between 0.1 and 100 cm/d and the hydraulic conductivity of the domain was varied between  $10^{-3}$  and  $10^{-5}$  m/s. Beach sands typically have hydraulic conductivities between  $10^{-3}$  and  $10^{-4}$  m/s (e.g., Urish and McKenna, 2004). For each measurement system the predicted diversion around large (57-cm-diameter) seepage meters was compared with the predicted diversion around small (15-cm-diameter) seepage meters to investigate the range of appropriate field conditions for deployment. The seepage meter error due to diversion was defined as the difference between the unrestricted groundwater

flow into a seepage meter and the predicted groundwater flow with the imposed pressure, divided by the unrestricted groundwater flow.

An additional model analysis was conducted to predict the cumulative diversion of groundwater around a seepage meter due to the increase in pressure within seepage meter bags as they fill. With a fixed SGD rate of 10 cm/d, the filling rate of a seepage meter bags during a deployment could be predicted based on laboratory measurement of the pressure within bags at incremental fill volumes. Predictions of the filling rates were made in 200 mL increments for polyethylene bags and 20 mL increments for condoms from their pre-fill volumes up to their capacities. At each incremental fill volume the known volume of SGD was compared to the predicted volume within the bag to calculate the error of SGD measurement. Polyethylene bags were assumed to be pre-filled with 1 L of water (Shaw and Prepas, 1989), and condoms were assumed to be pre-filled with 20 mL of water. Predictions were made for polyethylene bags attached to large and small seepage meters, and for condoms attached to small seepage meters. Sediment hydraulic conductivities of  $10^{-3}$  and  $10^{-4}$  m/s were tested.

### *Seepage Meter Design*

Large (57-cm-diameter) and small (15-cm-diameter) seepage meters were constructed from 208 L (55 gal) steel drums and size 10 “coffee” (3.2 L) tinplate food service cans, respectively (Figure 1). The large seepage meters were cut to a height of 32 cm and the small seepage meters were cut to a height of 12 cm, allowing them to penetrate sediments to the depth of the seepage meter radius as recommended by Murdoch and Kelly (2003).

Two ports were inserted in each seepage meter, a larger one at the center of the top for water expulsion during installation and a second, smaller one immediately below the rim to attach fittings for bags or dye displacement tubing. Press-seal bags (3.8 L) were used on both sizes of bag-equipped seepage meters. PVC tubing was attached to the bags by insertion over a barbed fitting placed in the inside corner of the bag to minimize constriction of the bag.

The seepage meters to be used for dye displacement were connected to clear, flexible PVC tubes (Figure 1). A 1.9 cm i.d., 1.5 m-long tube was attached to the large seepage meter and a 0.95 cm i.d., 1.25 m-long tube was attached to the small seepage meter. Meter sticks with mm markings were fastened to the dye displacement tubes to measure precise dye displacement distances (Figure 1). Rhodamine WT dye, in the xanthene family of dyes, was selected to indicate displacement because it is readily available, highly visible in water, and has low toxicity (Flury and Wai, 2003). The density of the dye is  $1.03 \pm 0.05 \text{ g/cm}^3$  at  $25^\circ\text{C}$ , close to the density of seawater. To more closely approximate the density of ambient water, one milliliter of 2.5% liquid Rhodamine WT dye was mixed with four milliliters of ambient water in a five milliliter syringe. The syringe needle was bent to approximately a  $90^\circ$  angle and inserted through the tube wall, allowing the syringe to be secured alongside the dye displacement tubing with the needle in place for multiple injections. Dye was typically injected at the 20 cm mark to allow measurement of dye displacement away from or towards the seepage meter, indicating groundwater discharge or inflow of overlying water respectively.

### *Comparison of Seepage Meter Methods*

We conducted field trials of bag-equipped and dye displacement seepage meters of both sizes (57-cm and 15-cm-diameter) positioned side-by-side at Sand Hill beach at the southern end of the Delmarva Peninsula on the Chesapeake Bay (37.2053 N, 76.0124 W), on the 10<sup>th</sup> of December, 2008. The beach was composed of clean, medium-grained sands. Pore water samples were collected from 10 cm below the sediment surface with a 2.4 mm diameter pore water probe (Berg and McGlathery, 2001) and salinity, defined as the conductivity ratio of a sea water sample to a standard KCl solution, was analyzed with a refractometer. The minimum pore water salinity was detected in a shore-parallel zone just offshore of the observed low tide mark. A total of 16 seepage meters, eight large and eight small, were deployed in a shore-parallel line in that zone. In each size group, four seepage meters were equipped with 3.8 L press-seal bags and four were equipped with dye displacement tubing. Large seepage meters were deployed 50 cm apart while small seepage meters were deployed 20 cm apart. The type of seepage meter alternated between bag-equipped and dye displacement from seepage meter to seepage meter along the beach.

Rates of SGD were determined after allowing one hour of equilibration following seepage meter deployment. Approximately hourly SGD measurements were made from 11:00 until 16:00 EST which included low tide at 12:45. Seepage meter bags, pre-filled with one liter of surface water, were connected for 30 minutes before they were replaced. Dye displacement readings were made in the interim and took less than 15 minutes to complete. At 15:00 the bag-equipped seepage meters were switched to dye displacement

measurement and vice versa. Water depth was logged every 10 seconds by an acoustic Doppler velocimeter (Vector, Nortek-AS, Norway).

### *Dye Displacement Measurement of Tidally-Forced SGD*

To further examine the ability of dye displacement seepage meters to measure a tidal response in SGD a second field trial was conducted using twelve small (15-cm-diameter) dye displacement seepage meters at Sand Hill beach on the 10<sup>th</sup> of February, 2009. Pore water samples were collected with a 2.4 mm diameter pore water probe (Berg and McGlathery, 2001) and salinities were determined with a refractometer. Seepage meters were deployed in a subtidal grid with three seepage meters in each of four alongshore transects. Seepage meter transect 1 was placed parallel to shore 1.5 m offshore of the observed low tide mark, in a zone where the minimum pore water salinity was observed. Transects 2, 3, and 4 were placed 1.5 m, 3 m, and 4.5 m offshore of transect 1, respectively. Seepage meters within each transect were placed 2 m apart.

Starting one hour after seepage meters were deployed, sixteen sets of dye displacement SGD measurements were made (total of 186) between 09:30 and 18:00. This interval included high tide at 09:30 and low tide at 15:20. Dye displacement measurements were initiated by injecting dye into every dye displacement tube in succession, then recording individual dye displacement distances. The maximum time interval between SGD measurements was 70 minutes and the minimum was ten minutes. To obtain an indication of marine and terrestrial contributions to SGD, porewater samples were taken from each of four seepage meter transects at six time intervals for a total of 24

observations. Water depth was logged every ten seconds by an acoustic Doppler velocimeter (Vector, Nortek-AS, Norway). The tidal range was 1.00 m.

## **Results**

### *Pressure Required by Seepage Meter Bags*

Filling sequences of seepage meter bags in laboratory tests showed that as a bag fills the pressure within the bag incrementally increases (Figure 3) requiring greater pressure for additional water to be added. As a result, an increasing amount of groundwater can be diverted around the seepage meter increasing the bias of SGD measurement. Empty polyethylene bags had a lower pressure than the hydrostatic pressure in the tank, consistent with the anomalous filling of empty seepage meter bags in stagnant water, and the recommendation of Shaw and Prepas (1989) to partially fill them before use. However, at volumes of 200 mL in twist-tie bags, and 400 mL in press-seal bags, the pressures within the bags exceeded the hydrostatic pressure within the tank (Figures 3a and 3b). At partial fill volumes between one and two liters, there were 0.2 to 0.6 mm-H<sub>2</sub>O of pressure in the twist-tie bags, and 0.1 to 0.3 mm-H<sub>2</sub>O of pressure in the press-seal bags. More pressure was observed in the thin-walled (25 µm) twist-tie bags than the thick-walled (100 µm) press-seal bags, in spite of wall thickness. Murdoch and Kelly (2003) also examined the pressure required to introduce water to seepage meter bags, and found that the average pressure required to force flow into 25 µm nylon-polyethylene bags was 0.5 mm-H<sub>2</sub>O.



In contrast to polyethylene bags, the pressure within condoms at partial-fill volumes was lower than that of the surrounding water in the test tank (Figure 3c). Specifically, relative to the test tank the pressure was -0.2 to -0.05 mm-H<sub>2</sub>O at partial fill volumes of 20 to 100 ml (Figure 3c). At a volume greater than 120 ml the inelastic threshold was reached and the pressure within the condoms exceeded hydrostatic pressure within the test tank. These observations indicate that during a deployment on a seepage meter, condoms could draw in water until they reached capacity, and thus could overestimate SGD. Our observations support Schincariol and McNeil (2002) who observed that under stagnant conditions in a test tank, condoms attached to seepage meters gained 43 mL of water over nine hours. They attributed this effect to the mechanical relaxation of the condom after it has been collapsed for attachment to the seepage meter.

#### *Pressure Required by Dye Displacement*

The measured pressure needed to force laminar flow through dye displacement tubing was similar to the pressure predicted by equation (1), and the magnitude of it suggested that less pressure would be required to measure SGD with a dye displacement seepage meter than a bag-equipped seepage meter. In laboratory observation, the pressure of the dye displacement method in mm-H<sub>2</sub>O (normalized to flow through 1.25 m of a 0.95 cm i.d. PVC tube) was 0.0121 times the flow rate in cm<sup>3</sup>/min ( $n = 6$ ,  $R^2 = 0.9444$ ). The equivalent prediction by equation (1) was 0.0107 times the flow rate in cm<sup>3</sup>/min. The difference between them was possibly caused by a bend in the test tubing to make side-

by-side measurements of the pressure difference between the inlet and outlet. As a result, equation (1) was used to predict the pressure needed to force flow through dye displacement tubing. On a large dye displacement seepage meter, with 1.5 m of a 1.9 cm i.d. tubing, equation (1) predicted an operating pressure of 0.00143 mm-H<sub>2</sub>O times the groundwater discharge in cm/d. On a small seepage meter, with 1.25 m of 0.95 cm i.d. tubing, the predicted operating pressure was 0.00132 mm-H<sub>2</sub>O times the groundwater discharge in cm/d. At an SGD rate of 10 cm/d these operating pressures are close to one-tenth the minimum operating pressures generated by partially filled polyethylene seepage meter bags (~0.1 mm-H<sub>2</sub>O, Figure 3).

Laboratory testing of the dye displacement method indicated that the location of the leading edge of dye is a highly reproducible method for quantifying discharge (Figure 4). The comparison between discharge calculated from the dye displacement method and the actual discharge agreed, with a calculated rate of 0.9998 times the actual discharge rate ( $R^2=0.9982$ ). With a maximum time interval of up to 32 minutes between dye displacement readings, and a maximum distance of up to 130 cm, only small deviations from the actual discharge were observed. The average difference between the calculated discharge and the actual discharge was  $2.6 \pm 2.1\%$  (standard deviation). This suggests that at these time and length scales the error due to dispersion of the dye is small.

#### *Groundwater Diversion Model*

The mathematical model presented in Figure 2 allowed us to quantify the diversion of SGD around seepage meters as a function of the groundwater discharge rate, the seepage

meter size, the sediment hydraulic conductivity, and the pressure required to force water into a seepage meter bag or through a dye displacement tube. In the first series of simulations, bag-equipped seepage meters were represented in the model by imposing a fixed pressure of 0.2 mm-H<sub>2</sub>O inside the top of the seepage meter, a representative pressure at a pre-fill volume of 1000 mL according to our lab tests of polyethylene bags shown in Figures 3a and 3b. Dye displacement seepage meters were represented in the model by setting the seepage meter pressure ( $p_{\text{seep}}$  in Figure 2) according to the relationships determined from equation (1), that is 0.00143 mm-H<sub>2</sub>O times the SGD rate in cm/d for large seepage meters, and 0.00132 mm-H<sub>2</sub>O times the SGD rate in cm/d for small seepage meters.

The model predicted that the pressure required for groundwater to flow into a seepage meter bag can cause substantial diversion of groundwater around seepage meters under commonly encountered field conditions. Figures 5a and 5b give the model predictions as a function of groundwater discharge rates from 0.1 to 1000 cm/d and hydraulic conductivities from  $10^{-3}$  to  $10^{-5}$  m/s (typical of coarse, clean sands to silty sands respectively (Freeze and Cherry, 1979)). The model predicted that bags attached to large seepage meters deployed in sands with a hydraulic conductivity of  $10^{-4}$  m/s, and a groundwater discharge rate of 1 cm/d, would cause the diversion of 40% of groundwater around the seepage meter (Figure 5a). Similarly, the model predicted that bags attached to small seepage meters deployed in the same conditions would divert all groundwater around the seepage meter (Figure 5b). These model predictions are consistent with the

unreliable performance of large seepage meters at discharge rates of 1 cm/day (Cable et al. 2006).

Based on observations of the lower pressure within partially-filled condoms relative to the hydrostatic pressure of the test tank (Figure 3c) it is clear that they can cause an overestimation of SGD, as demonstrated by Schincariol and McNeil (2002). The amount of this overestimation was evaluated in the model by imposing a pressure of -0.2 mm-H<sub>2</sub>O, suction, inside the top of the seepage meter ( $p_{\text{seep}}$  in Figure 2). The model predicted that because the magnitude of pressure was the same as that used for polyethylene bags (absolute value of 0.2 mm-H<sub>2</sub>O), the measurement error due to condoms would match those presented in Figures 5a and 5b but would be inverted, with error caused by SGD diversion into the seepage meter instead of diversion around it.

The smaller pressure required to move water through the tubing in dye displacement seepage meters reduces seepage meter error significantly (Figures 5c and 5d). In addition, as the rate of SGD decreases, the friction of flow through dye displacement tubing decreases. As a result, the error of dye displacement measurement does not change with the rate of SGD. Figure 5c shows model predictions that frictional resistance to flow through a large dye displacement seepage meter deployed in sands with a hydraulic conductivity of  $10^{-4}$  m/s will cause a groundwater diversion error of 0.3%. A small dye displacement seepage meter deployed in sands with the same hydraulic conductivity will cause a groundwater diversion error of 1% (Figure 5d).

Furthermore, based on our observations of the increase in pressure within seepage meter bags as they fill (Figure 3) we predict that total error due to ground water being

diverted around a seepage meter will increase with the volume collected in the attached bag. This was confirmed in the second series of model simulations in which these measured, increasing pressures were imposed. The errors shown in Figure 6 were calculated assuming an SGD rate of 10 cm/d, and pre-fill volumes of 1000 mL in polyethylene bags and 20 mL in condoms. The model predicts that if the volume contained in a twist-tie bag when it is collected from a large seepage meter deployed in sands with a hydraulic conductivity of  $10^{-4}$  m/s is 2.4 L, the measurement error is 9% (Figure 6a). If the bag was allowed to fill to a volume of 3.0 L, the predicted measurement error would increase to 19%. At volumes greater than 3.0 L we predict that the pressure within the bag would prevent further groundwater inflow. At a hydraulic conductivity of  $10^{-3}$  m/s the model predicted that the hydraulic gradient driving groundwater flow at 10 cm/d would be incapable of adding groundwater to the bag at a volume of 2.0 L (Figure 6a). Because of the smaller pressures observed within press-seal bags (Figure 3b) they caused a smaller measurement error due to groundwater diversion as they filled (Figure 6b).

In contrast to polyethylene bags, because of the low pressure within latex condoms relative to the test tank and the increase in pressure as they filled (Figure 3), the model predicted that the SGD measurement error will be smallest if condoms are collected containing a groundwater volume close to, but not exceeding, 120 mL (Figure 6c). Condoms attached to small seepage meters in sands with hydraulic conductivities of  $10^{-4}$  m/s and an SGD rate of 10 cm/d may have a measurement error of -12% at a fill volume of 40 mL (Figure 6c). The negative measurement error indicates that the

predicted rate of groundwater flow into the condom exceeds the rate of SGD. At fill volumes greater than 130 to 140 mL pressure within the condom prevented any further groundwater inflow.

### *Comparison of Seepage Meter Methods*

Field deployment of bag-equipped and dye displacement seepage meters side-by-side supported the model predictions that seepage meter bags can produce substantial SGD measurement error (Figure 7). Close to low tide, at 12:05, the large, bag-equipped seepage meters recorded  $48.1 \pm 27.0$  cm/d (mean and standard deviation,  $n = 4$  seepage meters), while the large, dye displacement seepage meters recorded a rate of  $45.2 \pm 11.0$  cm/d ( $n = 4$ ). In both sets of observations the tidal signal was evident, with a decline in SGD measured on the rising tide. Small, bag-equipped seepage meters did not reproduce the tidal signal clearly, recording  $26.6 \pm 37.8$  cm/d ( $n = 4$ ) at 12:05, and little evidence for an effect of tidal height on SGD (Figure 7b). Small, dye displacement seepage meters performed similarly to the large seepage meters with an SGD rate of  $52.6 \pm 10.6$  cm/d ( $n = 4$ ) at 12:05, and a decline in SGD on the rising tide. Integrated over the 5 hour deployment, the small, bag-equipped seepage meters measured 57% less SGD (Figure 7c), a significant difference (two sample independent t-test,  $p = 0.001$ ). This apparent error is in line with model predictions. We did not determine the hydraulic conductivity at this site but a typical range for beach sands is between  $10^{-4}$  m/s and  $10^{-3}$  m/s (e.g., Urish and McKenna, 2000). At an average SGD rate of  $35 \text{ cm day}^{-1}$ , in the middle of the hydraulic conductivity range of beach sands, the predicted measurement error caused by

bags on small seepage meters at pre-fill volumes is 22% (Figure 5b). In the same conditions the predicted measurement error caused by bags on large seepage meters at pre-fill volumes is 5% (Figure 5a). Because the SGD rate observed was greater than that represented in Figure 6, the cumulative measurement error cannot be determined directly from it, but we would expect the error to be smaller than the errors presented there. These predictions suggest that large, bag-equipped seepage meters measured a similar rate of SGD as large dye displacement seepage meters because the hydraulic pressure of SGD overcame the pressure associated with the collection bags. This was less true of the small, bag-equipped seepage meters.

#### *Dye Displacement Measurement of Tidally-Forced SGD*

The second field deployment at Sand Hill beach demonstrated the advantages in precision, sample rate, and sensitivity of dye displacement seepage meters. Small dye displacement seepage meters were used to examine fine spatial-scale variation in SGD across a seepage face. Six measurements of SGD were conducted at high tide constituting measurements from two seepage meters in each of transects one and two, and additional measurements from one seepage meter in each of transects three and four. These measurements showed a net inflow of overlying water into sediments (Figure 8a) with a mean of  $-9.8 \pm 5.4$  cm/d (standard deviation). At noon, on the falling tide, nearly uniform discharge was observed in all four transects, with a maximum of  $11.9 \pm 0.9$  cm/d in transect 1 and a minimum of  $7.7 \pm 3.1$  cm/d in transect 3 (Figure 8b). As the tide dropped, the rate of SGD increased to  $56.1 \pm 7.4$  cm/d at transect 1 and increased slightly

to  $14.5 \pm 1.4$  cm/d at transect 4 (Figure 8c). The maximum rate of discharge was observed in transect 1 at low tide with an SGD rate of  $71.7 \pm 8.7$  cm/d (Figure 8d). On the rising tide the pore water salinity reached a minimum as the rate of SGD in transect 1 decreased to  $20.5 \pm 3.6$  cm/d (Figure 8e). A saline plume was identified in the upper intertidal zone, and with fresher pore water in the narrow subtidal zone covered by seepage meter transects 1 and 2, the overall pattern was consistent with the narrow, brackish SGD zone predicted by Robinson et al. (2007).

The aggregate observations from transect 1, where the range of SGD rates was the greatest, are illustrated in Figure 9. Following high tide, at a tidal height of 0.9 m, the inflow of overlying water into sediments came to a halt. As low tide approached the rate of groundwater discharge increased, generating a brief peak in discharge at  $71.7 \pm 8.7$  cm/d (standard deviation) at low tide. The observation of inflow and the general pattern of the sharp peak in discharge at low tide were similar to observations made by automated seepage meters (Paulsen et al., 2001; Sholkovitz et al., 2003).

## **Discussion**

The laboratory test results for seepage meter bags suggests that bag thickness may not be the most important predictor of the pressures seepage meter bags impose on inflowing groundwater. Despite their thinner walls, a greater pressure was observed within twist-tie bags than within press-seal bags (Figure 3). This was possibly due to the method used for sealing the bag around seepage meter tubing. The opening of the twist-tie bags was collapsed around the tubing, reducing the maximum volume of the bag, and creating



multiple wrinkles and folds in the polyethylene. The press-seal bags, however, were attached through a barbed fitting to the seepage meter tube, minimizing constriction of the bag and the wrinkles that a constriction would create. The importance of wrinkles in polyethylene bags for generating resistance to inflow has been described previously (Murdoch and Kelly, 2003).

The increase in SGD measurement error due to the increase in pressure within seepage meter bags as they fill has direct implications for seepage meter deployments. In ideal conditions (e.g., at hydraulic conductivities of  $10^{-4}$  m/s or less, and groundwater discharge rates of greater than 10 cm/d) polyethylene bags and latex condoms may generate a measurement error of less than 10% (Figure 6). However, as our results show, the error is highly dependent on hydraulic conductivity and groundwater flow rate. To reduce the error of SGD measurement with seepage meter bags, a thin walled bag heat-sealed along the open end, as employed by Lee (1977), may offer an improvement both in the increased capacity of a bag, and in the reduced resistance to inflow that may be generated by folds in the walls. Additionally, if using polyethylene bags, a shorter time interval of SGD measurement to ensure that bag volumes do not approach capacity is likely to reduce the error of measurement (Figure 6).

Because the pressure exerted by seepage meter bags on inflowing water is capable of causing significant measurement error in common field conditions, the dye displacement method of SGD can serve as a useful alternative. A comparison of the pressure required to introduce water into seepage meter bags (Figure 3) versus the pressure required to introduce laminar flow through dye displacement tubing, given by

equation (1), demonstrates that at an SGD rate of 10 cm/d the pressure required for flow through dye displacement tubing is an order of magnitude smaller. Additionally, because the pressure required to make SGD measurements by dye displacement is a function of flow rate, the error of dye displacement measurement due to diversion will not change with SGD rate. This characteristic is shared among open path measurement systems, and so we expect that the behavior of dye displacement would be similar to the behavior of far more expensive automated seepage meters.

The groundwater diversion model confirms that the reduced pressure required by dye-displacement improves the accuracy of SGD measurement in some common field conditions (Figure 5). If an acceptable amount of groundwater diversion due to measurement pressure in a seepage meter deployment is 10%, a large seepage meter equipped with a bag containing less than 2 L of groundwater would be restricted to measuring a minimum rate of 4 cm/d in sands with a hydraulic conductivity of  $10^{-4}$  m/s (assuming a bag pressure of 0.2 mm-H<sub>2</sub>O; Figure 5a). However, a large dye displacement seepage meter would divert only 0.3% of groundwater at that site, regardless of the SGD rate (Figure 5c). Similarly, a small bag-equipped seepage meter would be restricted to measuring a minimum rate of 14 cm/d in sands with the same hydraulic conductivity (Figure 5b), while a small dye displacement seepage meter would divert less than 1% of SGD (Figure 5d). The diversion caused by the dye displacement measurement system could be further reduced with a small increase in the diameter of dye displacement tubing. A small increase will have a large effect on pressure because the friction of

laminar flow within a tube predicted by equation (1) is inversely proportional to the tube radius raised to the fourth power.

Murdoch and Kelly (2003) also developed a model of groundwater flow and diversion around seepage meters based on the pressure required to force groundwater into seepage meter bags. However, bag pressure in their model is represented as a linear function of the inflow rate, as a conductance, while we represented it as independent of flow rate, as a fixed pressure. Despite the discrepancies in formulation, the model predictions are similar. Our results support their assertion that seepage meter bags can cause the diversion of a substantial amount of SGD under common operating conditions.

The results of the field deployments indicate that the dye displacement technique improves the sensitivity of seepage meters (Figures 8 and 9). In the second trial (Figure 9), dye displacement seepage meters detected patterns similar to those determined with far more expensive, open flow-path automated seepage meters (e.g., Paulsen et al., 2001; Sholkovitz et al., 2003). Specifically, dye displacement seepage meters measured inflow of overlying water into subtidal sediments at high tide and a sharp peak in SGD at low tide. These patterns are also predicted by numerical models of tidally-forced SGD (Robinson et al., 2007; Maji and Smith, 2009), yet reproducible observations of inflow into submarine sediments with bag-equipped seepage meters are less common (e.g., Lee, 1977). We expect that an increase in the sensitivity of SGD measurement will lead to more common observations of this process.

The dye displacement method allows a relatively high number of measurements per unit time. In this study, measurements of SGD through twelve dye displacement

seepage meters were made at a rate of up to once every ten minutes, for a total of close to two hundred SGD measurements by two individuals in eight hours. The reduced time required for SGD measurement by dye displacement seepage meters allows more flexibility in sampling SGD at a greater spatial or temporal resolution than bag-equipped seepage meters. Additionally, the visual nature of the technique allows the use of submersible cameras for data recording, further reducing the time and effort required for SGD measurement.

Dye displacement seepage meters offer advantages in measuring SGD, but there is work to be done to increase the range of applications in which they can be used. One area of work is in low visibility water. We have performed dye displacement measurements of SGD with visibility as low as 40 cm, but visibilities in nearshore waters can be less than that. One approach to improve the usefulness of dye displacement in low visibility waters are submersible point-and-shoot cameras, with submersible lights, that can be held within a few centimeters of tubing to capture images. Alternately, the ends of the tubing may be clamped, or closed, and the tubing carefully lifted to the surface for potential observation of dye displacement distances.

Many other limitations of the dye displacement method match the limitations of traditional seepage meters. Substrate type, water depth, daylight, and currents affect the ease of use of all types of seepage meters. Rocky substrates are physically difficult environments to deploy seepage meters, and as water depth increases the logistical demands of deployment also increase. Currents can have a substantial effect on the bags attached to seepage meters (Libelo and MacIntyre, 1994) and alter pressure gradients

against the exposed surfaces of seepage meters. Dye displacement seepage meters should be used with care in environments with strong currents, at least until potential limitations have been investigated under such conditions. Shelters have been devised to minimize the effect of currents on seepage meter bags (Libelo and McIntyre, 1994), and the profile of seepage meters can be reduced to minimize the exposure of seepage meters to strong currents (Rosenberry, 2008). We expect similar attention would lead to reproducible measurement of SGD by dye displacement seepage meters in high current environments as well.

### **Summary**

Dye displacement seepage meters offer advantages over bag-equipped seepage meters in SGD precision, sample rate, and sensitivity for a similar construction cost. Their advantages are particularly noticeable at sites with high hydraulic conductivities (greater than  $10^{-4} \text{ m s}^{-1}$ ) and low SGD rates (less than  $10 \text{ cm day}^{-1}$ ). Furthermore, they are capable of measuring the inflow of overlying water into sediments, a trait that is typically reproduced only with far more expensive automated seepage meters.

## Literature Cited

- Berg P., and K. J. McGlathery. 2001. A High-resolution pore water sampler for sandy sediments, *Limnol. Oceanogr.*, 46(1), 203-210.
- Boehm, A. B., G. G. Shellenbarger, and A. Paytan. 2004. Groundwater discharge: Potential association with fecal indicator bacteria in the surf zone, *Environ. Sci. Technol.*, 38(13), 3558–3566.
- Bokuniewicz H. 1980. Groundwater seepage into Great South Bay, New York, *Estuar. Coast. Mar. Sci.*, 10(4), 437-444.
- Bone, S. E., M. A. Charette, C. H. Lamborg, and M. E. Gonneea. 2007. Has submarine groundwater discharge been overlooked as a source of mercury to coastal waters? *Environ. Sci. Technol.*, 41(9), 3090–3095, doi:10.1021/es0622453.
- Burnett, W. C., H. Bokuniewicz, M. Huettel, W. S. Moore, and M. Taniguchi. 2003. Groundwater and pore water inputs to the coastal zone, *Biogeochemistry*, 66(1), 3–33, doi:10.1023/B:BIOG.0000006066.21240.53.
- Burnett, W. C., M. Taniguchi, and J. Oberdorfer. 2001. Measurement and significance of the direct discharge of groundwater into the coastal zone, *J. Sea Res.*, 46(2), 109–116, doi:10.1016/S1385-1101(01)00075-2.
- Cable, J. E., J. B. Martin, and J. Jaeger. 2006. Exonerating Bernoulli? On evaluating the physical and biological processes affecting marine seepage meter measurements *Limnol. Oceanogr.-Meth.*, 4, 172–183

- Corbett, D. R., J. Chanton, W. Burnett, K. Dillon, C. Rutkowski, and J. W. Fourqurean. 1999. Patterns of groundwater discharge into Florida Bay, *Limnol. Oceanogr.*, 44(4), 1045–1055.
- Crusius, J., P. Berg, D. J. Koopmans, and L. Erban. 2008. Eddy correlation measurements of submarine groundwater discharge, *Mar. Chem.*, 109, 77-85, doi:10.1016/j.marchem.2007.12.004.
- Flury, M., and N. N. Wai. 2003. Dyes as tracers for vadose zone hydrology. *Rev Geophys*, 41(1), Art. No. 1002, doi:10.1029/2001RG000109.
- Freeze, R. A., and J. A. Cherry, *Groundwater*, Prentice-Hall, New York, 1979.
- Fryar, A. E., E. J. Wallin, and D. L. Brown. 2000. Spatial and Temporal Variability in Seepage Between a Contaminated Aquifer and Tributaries to the Ohio River. *Ground Water Monit. R.*, 20(3), 129-146, doi:10.1111/j.1745-6592.2000.tb00279.x.
- Giblin, A. E., and A. G. Gaines. 1990. Nitrogen inputs to a marine embayment: The importance of groundwater, *Biogeochemistry*, 10(3), 309-328.
- Hu, C., F. E. Muller-Karger, and P. W. Swarzenski. 2006. Hurricanes, submarine groundwater discharge, and Florida's red tides, *Geophys. Res. Lett.*, 33, L11601, doi:10.1029/2005GL025449.
- Johannes, R. E. 1980. Ecological significance of the submarine discharge of groundwater, *Mar. Ecol.-Prog. Ser.*, 3(4), 365–373.
- Kundu, P. K., and I. M. Cohen, *Fluid Mechanics*, Elsevier Academic Press, San Diego, 2004.

- Lee, D. R. 1977. A device for measuring seepage flux in lakes and estuaries, *Limnol. Oceanogr.*, 140–147.
- Libelo, E. L., and W. G. MacIntyre. 1994. Effects of surface-water movement on seepage-meter measurements of flow through the sediment-water interface, *Hydrogeology J.*, 2(4), 49–54.
- Maji, R. and L. Smith. 2009. Quantitative analysis of seabed mixing and intertidal zone discharge in coastal aquifers, *Water Resour. Res.*, 45, W11401, doi:10.1029/2008WR007532.
- Moore, W. S. 1996. Large groundwater inputs to coastal waters revealed by <sup>226</sup>Ra enrichments, *Nature* 380, 612-614.
- Moore, W. S. 1999. The subterranean estuary: A reaction zone of ground water and sea water, *Mar. Chem.*, 65, 111-125, doi:10.1016/S0304-4203(99)00014-6.
- Murdoch, L. C., and S. E. Kelly. 2003. Factors affecting the performance of conventional seepage meters, *Water Resour. Res.*, 39(6), 1163, doi:10.1029/2002WR001347.
- Nixon, S. W. 1995. Coastal marine eutrophication: A definition, social causes, and future concerns, *Ophelia*, 41, 199–219.
- Paerl, H. 1997. Coastal eutrophication and harmful algal blooms: Importance of atmospheric deposition and groundwater as “new” nitrogen and other nutrient sources, *Limnol. Oceanogr.*, 42(5), 1154-1165.
- Paulsen, R. J., C. F. Smith, D. O'Rourke, and T. F. Wong. 2001. Development and evaluation of an ultrasonic ground water seepage meter, *Ground Water*, 39(6), 904–911, doi:10.1111/j.1745-6584.2001.tb02478.x.



- Patankar, S. V. 1980. Numerical Heat Transfer and Fluid Flow, Taylor and Francis, Philadelphia, PA.
- Poiseuille J.L. 1846. Recherches expérimentales sur le mouvement des liquides dans les tubes de très petits diamètres, Mémoires presentes par divers savants étrangers a l'Academie des Sciences Paris, 9, 433-544
- Robinson, C., L. Li, and D. A. Barry. 2007. Effect of tidal forcing on a subterranean estuary, Adv. Water Resour., 30, 851-865, doi:10.1016/j.advwatres.2006.07.006.
- Rosenberry, D.O. 2008. A seepage meter designed for use in flowing water, J. Hydrol., 359, 118-130, doi:10.1016/j.jhydrol.2008.06.029.
- Rosenberry, D. O., and R. H. Morin. 2004. Use of an electromagnetic seepage meter to investigate temporal variability in lake seepage, Ground Water, 42, (1), 68–77, doi:10.1111/j.1745-6584.2004.tb02451.x.
- Riedl, R. J., N. Huang, and R. Machan. 1972. The subtidal pump: A mechanism of interstitial water exchange by wave action, Mar. Biol., 13, 210-221.
- Schincariol, R. A., and J. D. McNeil. 2002. Errors with small volume elastic seepage meter bags. Ground Water, 40(6), 649-651.
- Shaw, R. D., and E. E. Prepas. 1989. Anomalous, short-term influx of water into seepage meters, Limnol. Oceanogr., 1343–1351.
- Sholkovitz, E., C. Herbold, and M. Charette. 2003. An automated dye-dilution based seepage meter for the time-series measurement of submarine groundwater discharge, Limnol. Oceanogr.-Meth., 1, 16-28.

- Simmons, G. M. 1992. Importance of submarine groundwater discharge (SGWD) and seawater cycling to material flux across the sediment/water interfaces in marine environments, *Mar. Ecol.-Prog. Ser.*, 84, 173-184.
- Taniguchi, M., and Y. Fukuo. 1993. Continuous measurements of ground-water seepage using an automatic seepage meter, *Ground Water*, 31(4), 675–679.
- Taniguchi, M., and H. Iwakawa. 2001. Measurements of submarine groundwater discharge rates by a continuous heat-type automated seepage meter in Osaka Bay, Japan, *J. Groundwater Hydrol.*, 43(4), 271–278.
- Taniguchi, M., W. C. Burnett, C. F. Smith, R. J. Paulsen, D. O'Rourke, S. L. Krupa, and J. L. Christoff. 2003. Spatial and temporal distributions of submarine groundwater discharge rates obtained from various types of seepage meters at a site in the northeastern Gulf of Mexico, *Biogeochemistry*, 66(1), 35–53, doi:10.1023/B:BIOG.0000006090.25949.8d.
- Tryon, M., K. Brown, L. R. Dorman, and A. Sauter. 2001. A new benthic aqueous flux meter for very low to moderate discharge rates, *Deep-Sea Res. Pt. I*, 48(9), 2121–2146 doi:10.1016/S0967-0637(01)00002-4.
- Urish D.W., and T. E. McKenna. 2004. Tidal effects on groundwater discharge through a sandy marine beach, *Ground Water*, 42(7), 971-982, doi:10.1111/j.1745-6584.2004.tb02636.x.

Valiela, I., J. Costa, K. Foreman, J. M. Teal, B. Howes, and D. Aubrey. 1990. Transport of groundwater-borne nutrients from watersheds and their effects on coastal waters, *Biodegradation*, 10(3), 177–197.

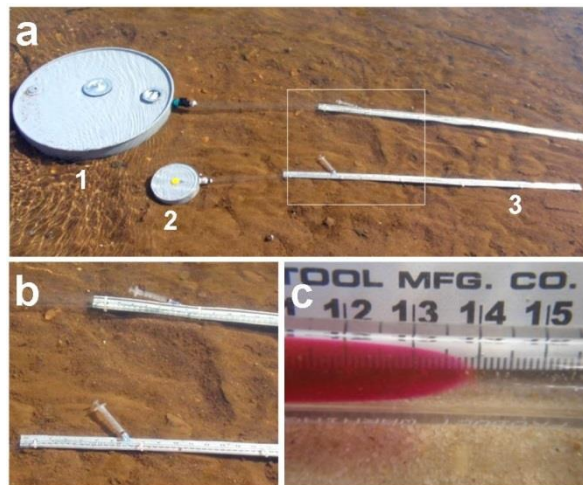


Figure 1. **A** Two sizes of dye displacement seepage meters prior to injection: a 57 cm diameter seepage meter (1) with an attached 1.5 m long PVC tube and a 15 cm diameter seepage meter (2) with an attached 1.25 m long PVC tube. An aluminum meter stick (3) was used to measure dye displacement. **B** An expanded view of 5 ml syringes with needles inserted into tubing for dye injection. **C** The leading edge of dye after ten minutes of displacement.

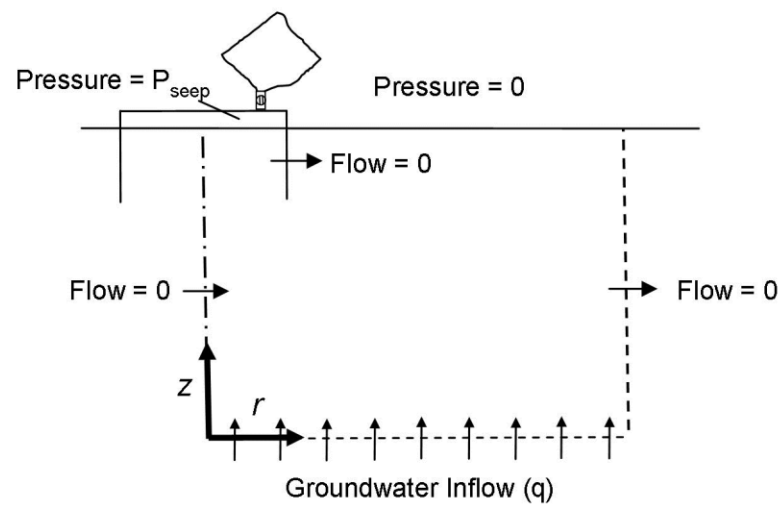


Figure 2. The domain and boundary conditions for the model used to solve the partial differential Darcy flow equation in cylindrical coordinates.

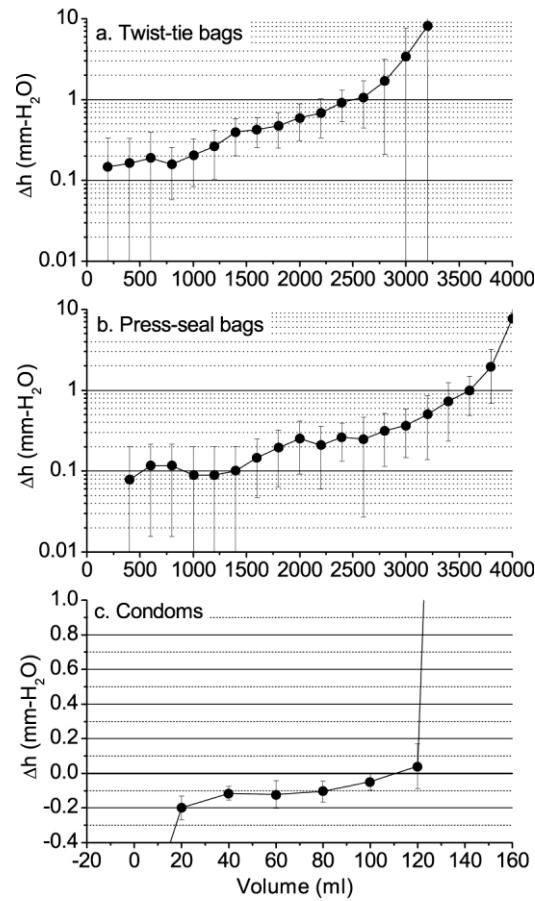


Figure 3. The hydraulic head within seepage meter bags as a function of fill volume for three commonly used types of seepage meter bags, **A** polyethylene twist-tie bags, **B** polyethylene press-seal bags, **C** latex condoms (note change in scale). Negative values indicate a negative hydraulic head relative to the test tank. Each observation is the mean of five trials, error bars represent standard deviation. At a groundwater discharge rate of 10 cm/d the fill rate for a bag attached to a 57 cm diameter seepage meter would be 1100 mL/hr.

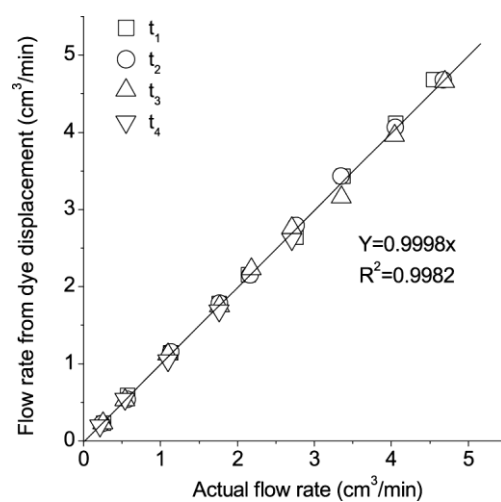


Figure 4. The volumetric flow rate calculated from displacement of the leading edge of dye as a function of the actual flow rate (0.95 cm inner diameter tube). Following dye injection three to four successive observations of dye displacement were made ( $t_1 - t_4$ ).

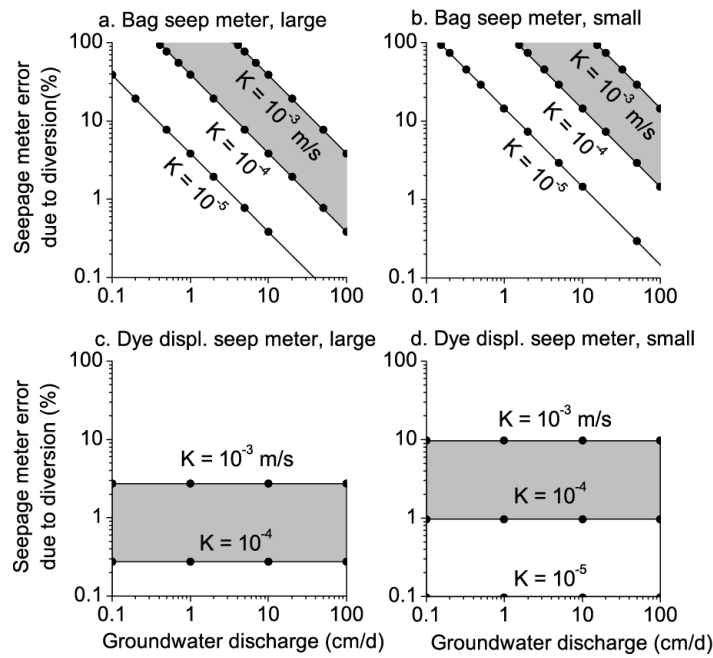


Figure 5. Model-predicted diversion of groundwater discharge around **A**, **B** bag-equipped seepage meters **C**, **D** dye displacement seepage meters plotted as a function of groundwater discharge rate. Diversion around 57 cm diameter and 15 cm diameter small seepage meters was predicted. The seepage meter error due to diversion was defined as the difference between the unrestricted and the predicted groundwater flow into a seepage meter, with the result divided by the unrestricted groundwater flow. At 100% error no groundwater discharge would be detected. A hydraulic conductivity range typical of beach sands,  $10^{-4}$  to  $10^{-3}$  m/s, is shaded.



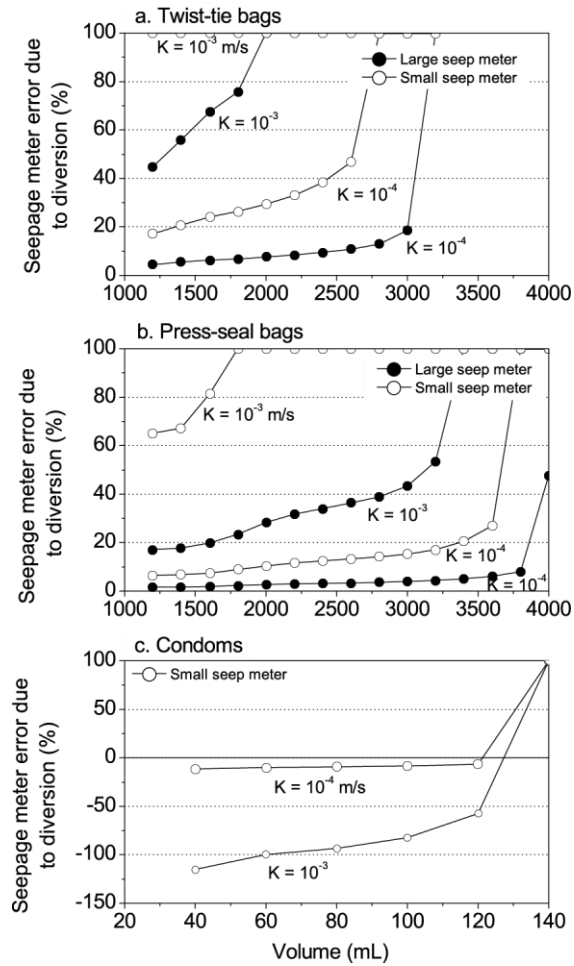


Figure 6. Model-predicted diversion of groundwater discharge as a function of bag volume at a discharge rate of 10 cm/d. Measurement error was predicted for **A** twist-tie bags, **B** press-seal bags, and **C** condoms attached to 57 cm diameter and 15 cm diameter seepage meters. Hydraulic conductivities were chosen to bracket the typical range of beach sands. Negative values indicate a greater measured rate of groundwater discharge than the actual rate.

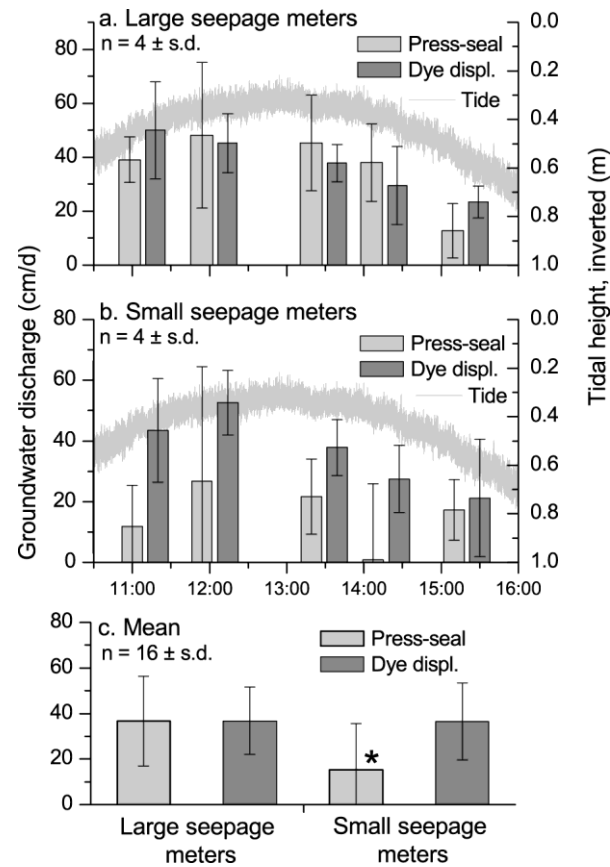


Figure 7. Intercomparison of groundwater discharge measured simultaneously with **A** 57 cm diameter and **B** 15 cm diameter seepage meters equipped with press-seal bags (light grey) or dye displacement tubing (dark grey). Bars are offset in time for clarity. Tidal height is inverted for comparison with groundwater discharge. Noise in tidal height data was caused by waves. **C** Means of discharge measurements with each method. The asterisk denotes significant difference between small bag-equipped seepage meters and the small dye displacement seepage meters (two sample independent t-test, p-value of 0.001).

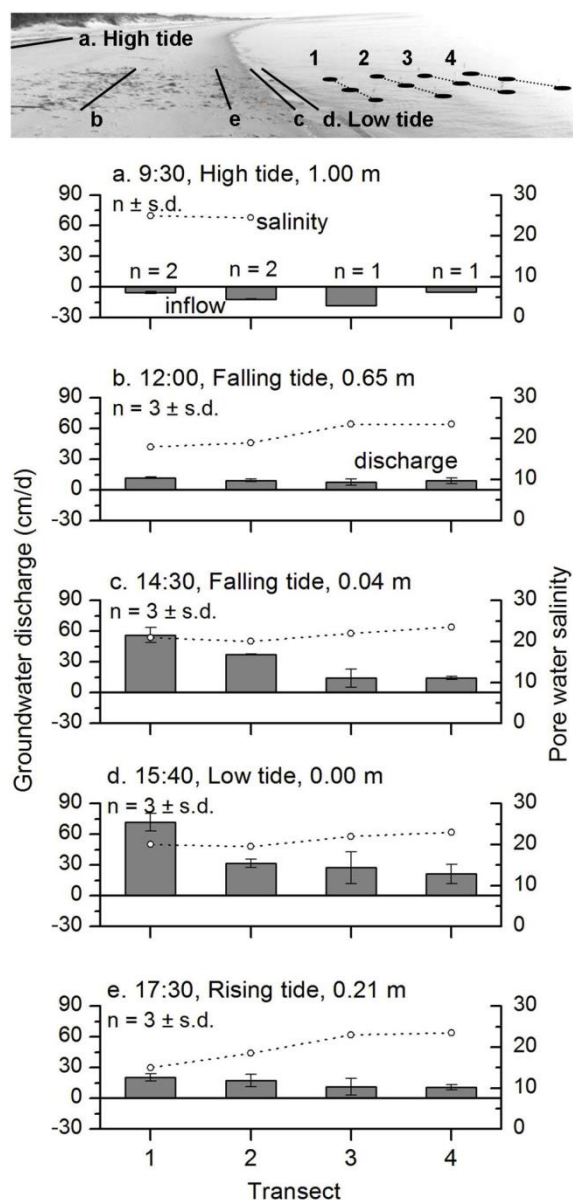


Figure 8. Tidal forcing of groundwater discharge measured with 15 cm diameter dye displacement seepage meters at Sand Hill beach, VA. The image at top indicates tidal positions and seepage meter transects 1 to 4. Tidal position plots show **A** overlying water inflow to sediments at high tide, and subsequent groundwater discharge on the **B, C, D**, falling and **E** rising tides. The salinity was 24 in overlying water.

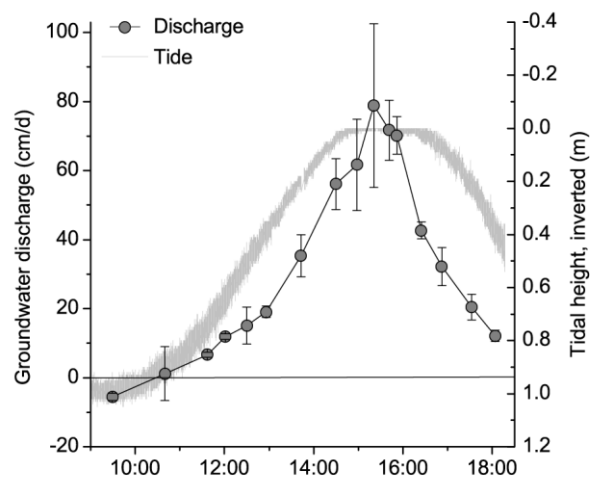


Figure 9. Tidal forcing of groundwater discharge at transect 1 measured with dye displacement seepage meters ( $n = 2$  before 1000 LT,  $n = 3$  after 1000 LT). Tidal height is inverted for comparison with discharge. At low tide the pressure transducer was exposed to atmospheric pressure in wave troughs.

## Chapter 3

### The Effect of Velocity on Ecosystem Metabolism in a Coastal Stream

Koopmans, D. and P. Berg

Document prepared for submission to the journal *Ecosystems*

**Abstract**

Inland waters are responsible for the mineralization and storage of a large portion of net ecosystem terrestrial production. Accurate prediction of these rates depends in part on our understanding of the drivers of aquatic ecosystem metabolism. The effect of changes in light, temperature, and water velocity on photosynthesis and respiration rates was examined seasonally for two years in a topographically low-gradient, nutrient-rich, sand-bedded stream in coastal Virginia, USA. The stream was consistently heterotrophic ( $-306 \pm 83 \text{ mmol m}^{-2} \text{ d}^{-1}$ , SE,  $n = 8$  seasons) with diurnal variation due to storm events that exceeded seasonal variation. A storm-driven stage-discharge shift occurred that was associated with persistent changes in stream hydrology and ecology, including suppressed rates of gross primary production. Across eight seasons the clearest driver of both photosynthesis and respiration was water velocity. Changes in water velocity explained 75% of the variance in gross primary production in the spring ( $n = 24$  days), but the effect of velocity on primary production was inconsistent in other seasons. Changes in water velocity explained 90% and 97% of the variance in rates of respiration before and after the stage-discharge shift, respectively ( $n = 63$  days and 40 days, respectively). Velocity-driven increases in hyporheic exchange were the likely cause of the increase in respiration rates. These results demonstrate that water velocity drives respiration in this alluvial stream ecosystem.

## **Introduction**

Until recently inland waters were represented in global carbon budgets as passively transporting the organic matter they received to the coastal ocean. Instead they are an active component of the global carbon cycle, receiving half of net terrestrial ecosystem production and respiring or storing half again of that carbon en route to the coastal ocean (Cole et al., 2007). While small streams were not included in the above analysis they may disproportionately contribute to the respiration of terrestrial organic matter (Battin et al., 2008). They are the initial receiving waters for most of exported terrestrial organic matter, and the high rates of respiration within them are given by their elevated partial pressure of CO<sub>2</sub> and elevated gas transfer velocities relative to downstream waters (Butman and Raymond, 2011). Improving our understanding of these systems and their response to environmental change may improve our understanding of the global carbon budget.

It has been a consistent goal of riverine ecological research to quantify the response of rivers to environmental drivers. Two drivers that have explained a lot of the variation in metabolism in streams research are the response of gross primary production (GPP) to photosynthetically active radiation and responses in ecosystem respiration (R) to seasonal changes in allochthonous carbon sources. The preponderance of research emphasizes the importance of these drivers, but it is surprising how few studies have questioned the role of water velocity in directly driving both GPP and R at the ecosystem scale. In marine environments, in contrast, water velocity has received substantial attention for its role in compressing the benthic boundary layer over cohesive sediments

and driving hyporheic exchange in permeable sediments (reviewed by Glud, 2008). The proximal drivers of metabolism in rivers are: sunlight, temperature, nutrients, labile organic matter, and water velocity. Theoretical and empirical models are available that describe the metabolic response at an ecosystem scale to changes in light (Boston and Hill, 1991), temperature (Brown et al., 2007), and nutrient addition (Hilton et al., 2006; Dodds et al., 2002). Water velocity acts as a driver of ecosystem metabolism through enhancing mixing at a broad range of spatial scales, yet observations that describe an ecosystem response to changes in water velocity are lacking.

Diffusive boundary layers are present around all surfaces in flowing waters, and they may limit both the supply of carbon dioxide and nutrients to photosynthetically active autotrophs (Fonseca and Kenworthy, 1987). The limitation may be more pronounced where macrophytes are densely concentrated. As water velocity increases the limitation of photosynthetic production by deficits of carbon dioxide or nutrients, or by an excess of oxygen (Bjorkmann, 1966) may decline. Increases in flow velocity correlate with increases in the photosynthetic rate of rooted macrophytes and seagrasses under low to moderate flow conditions (up to  $0.1 \text{ m s}^{-1}$ ; Westlake, 1967; Fonseca and Kenworthy, 1987; Madsen et al. 2001), but determined under in situ conditions with the eddy correlation technique (Berg et al., 2003), increases in gross primary production due to increases in velocity may be offset by corresponding increases in respiration rates (Hume et al., 2010; Long et al., 2013; Rheuban et al., 2013).

Water velocity is a driver of hyporheic exchange, which is responsible for the bulk of respiration in at least a few stream ecosystems including another sand-bed coastal



stream in Virginia (Fuss and Smock, 1996) and a prealpine gravel-bed river in Switzerland (Naegeli and Uehlinger, 1997). Similarly, with increases in water velocity the diffusive boundary layer over low-permeability sediments is minimized, increasing the rate of diffusion of oxygen and carbon dioxide across the sediment-water interface. Where sediments are permeable, pore water exchange is driven as a function of grain diameter and water velocity squared (Packman et al., 2004). While determining a rate of oxygen flux from the rate of pore water exchange is complicated by the limitations of bacterial enzymes, predictive relationships may not be far off. Clear relationships between water velocity and respiration in permeable sediments have been demonstrated in stirred benthic chambers (Boynton et al. 1981; Janssen et al., 2005), and under in-situ conditions (Berg et al., 2013).

The goal of this work was to examine the proximal drivers of metabolism in an alluvial stream where porous sediments are conducive to hyporheic exchange. Because organic matter respiration is the end-goal of stream metabolism measurements, neither allochthonous carbon inputs nor in situ DOC production was included in the suite of proximal drivers. We examined diurnal and seasonal changes in stream metabolism with changes in light, temperature, and water velocity.

### **Study Site**

The study site was Rattrap Branch on the eastern shore of Virginia, 5 km southeast of the town of Onley. The stream is contained within the Virginia Coast Reserve Long Term Ecological Research site. The watershed is split between agriculture (38%) and forest

(41%) with the remainder primarily in low-density residential use (Luckenbach et al., 2008). The stream has a sand-bed and a base flow discharge of  $40 \text{ l s}^{-1}$ . At baseflow conditions the width of Rattrap Branch varied from 1 to 3 m along the study reach, with stream depth in the thalweg typically 15 cm, but up to 1 m in pools. Portions of the stream conform to a riffle-pool morphology

## **Methods**

### *Physical and Chemical Characteristics*

During each sampling period concurrent measurements were made to describe temporal changes in stream stage, PAR at the stream bed, and water temperature. Changes in stream water depth over time were calculated by subtracting atmospheric pressure recorded at a local airport (4 km distant) from ambient pressure recorded at the bed of the stream by a water level logger (Onset Computers, Onset MA). Stream stage was read off a staff gauge that had been driven into streambed sediments. Stream depth data were benchmarked to stage height to ensure accurate relative measures of stream stage across sampling periods.

Photosynthetically Active Radiation (PAR) at the stream bed was determined with HOBO Pendant Temperature/Light submersible data loggers and Odyssey PAR recorders, both of which were calibrated to PAR at the streambed with a LI-COR LI 193 Underwater Spherical Quantum Sensor (Long et al., 2012). A minimum of six light

loggers were deployed with a spacing of 15 m between each one along the 100 m study reach.

Additional measurements were made of sediment and water column characteristics. Triplicate water column samples for nitrate, ammonium, phosphorous, total dissolved nitrogen, and total dissolved phosphorus analyses were collected five times over the course of the study. Nutrient samples were pre-filtered through an ashed 0.45  $\mu\text{m}$  glass fiber filter then frozen until analyzed by spectrophotometric analysis (Parsons et al., 1984) on a Lachat autoanalyzer. Organic nitrogen and organic phosphorus were determined by difference between the inorganic and total dissolved concentrations, the latter extracted by high temperature persulfate oxidation. Triplicate samples for particle size distribution and organic matter content analysis were collected from the top seven centimeters of sediment at three sand-bedded locations (the predominant bed type) within the 100 m study reach. The organic matter content of dried sediments was determined by combustion at 500°C for 4 hours. Following organic matter removal sediments were dis-aggregated with a mortar and pestle before the particle size distribution was analyzed on a Beckman Coulter LS 13 320 laser diffraction particle size analyzer. The hydraulic conductivity of the upper 10 cm of sediment was determined at a channelized and a riffle site within the study reach. Surficial sediments were transferred to a permeameter for determination of hydraulic conductivity by the constant head technique (e.g., Landon et al., 2001). Further detail on sediment characteristics at the study site may be found in Koopmans and Berg (in prep.).

### *Dissolved Oxygen Flux*

To determine metabolism with the open water technique both continuous measurement of dissolved oxygen concentrations in the stream (e.g. at 15 min intervals) and the gas transfer velocity are required. Metabolism in Rattrap Branch was determined first in the fall of 2010, then seasonally from the spring of 2011 through the fall of 2012. The duration of each sampling period varied from 4 days in the fall of 2010 to 20 days in the summer of 2012, totaling 103 days in which a complete 24 hour record of dissolved oxygen fluxes were determined. The open water technique was used to determine stream Respiration (R) and Gross Primary Production (GPP). Ecosystem metabolism was quantified as the benthic oxygen flux because the benthic community was expected to drive the changes oxygen concentration in the water column. The benthic oxygen flux was determined from a 1D vertical oxygen balance across the air-water and water-sediment interfaces,

$$j_{air} + h \frac{\Delta C}{\Delta t} - j_{benthic} = 0 \quad (1)$$

where  $j_{air}$  is the oxygen flux across the air-water interface,  $h$  is the water depth,  $C$  is the concentration of oxygen,  $t$  is time and  $j_{benthic}$  is the oxygen flux across the sediment-water interface. The flux across the air-water interface was defined as

$$j_{air} = -k([O_2]_{sat.} - [O_2]_{obs.}) \quad (2)$$

where  $k$  is the gas transfer velocity and  $[O_2]_{\text{sat.}}$  and  $[O_2]_{\text{obs.}}$  are the concentration of oxygen at saturation with air (due to temperature and pressure) and observed in the water column. During net oxygen uptake by the stream bed, oxygen crosses the air-water interface and can be stored in the water column or taken up by the benthos. The 1D balance accounted for oxygen stored in the water column as the product of water depth and the change in oxygen concentration over time. Metabolic processes occurring in the water column are incorporated into the benthic flux term.

The gas transfer velocity was calculated from the measured loss of an introduced propane gas tracer relative to the loss of a salt tracer along a 100 m study reach (Wanninkhof et al., 1990; Marzolf et al., 1994; Young and Huryn 1998). These measurements were made 11 times over the course of the study, across a wide range of stream stages and water velocities. To improve the lateral distribution of the tracers both were dispersed across the stream at the point of introduction. Salt water, with a concentration of  $100 \text{ g l}^{-1}$ , was introduced through a drip line at flow rate of  $90 \text{ l hr}^{-1}$ . Propane was introduced through a manifold of fine-pore aquarium diffusers at a flow rate of  $1.5 \text{ kg hr}^{-1}$ . Concentration changes in salt and propane were measured 45 m and 145 m downstream of the introduction point, delineating the upstream and downstream ends of the 100 m study reach, respectively. During salt and propane introduction conductivity measurements were made across the stream at the upstream end of the study reach to confirm that complete lateral mixing of salt had occurred. The mean stream velocity was determined from the travel time of an introduced salt spike.

To calculate the gas transfer velocity for propane a mass balance for salt and propane was solved segment by segment along the study reach in a Eulerian approach. A sediment transfer velocity (a counterpart to the air-water gas transfer velocity) was determined to quantify hydrodynamic losses of both the gas and salt tracer to the sediment due to dilution and diffusion. The 2D mass balance for salt was composed as

$$UC_1wd - k_{sed.} \left( \frac{C_1+C_2}{2} - C_{sed.} \right) wL - UC_2wd = 0 \quad (3)$$

where  $U$  is the mean stream velocity,  $C_1$  and  $C_2$  are tracer concentrations at the upstream and downstream ends of the study reach,  $w$  is the mean stream width,  $d$  is mean stream depth,  $k_{sed.}$  is the sediment transfer velocity,  $C_{sed.}$  is the initial tracer concentration in sediments (assumed to be zero), and  $L$  is the study reach length. Solving this equation for the sediment transfer velocity gives

$$k_{sed} = \frac{2Ud(C_1-C_2)}{L(C_1+C_2)}. \quad (4)$$

The solution to a mass balance for propane matches equation 2 but with an additional term for the transfer of propane across the water-air interface. It was composed as

$$UG_1wd - k_{sed.} \left( \frac{G_1+G_2}{2} - G_{sed.} \right) wL - k_{prop.} \left( \frac{G_1+G_2}{2} - G_{air} \right) wL - UG_2wd = 0, \quad (5)$$

where  $G_1$  and  $G_2$  are the concentrations of the gas tracer at the upstream and downstream ends of the study reach, respectively,  $k_{prop.}$  is the propane gas transfer coefficient at the air-water interface, and  $G_{air}$  is the initial concentration of tracer gas in air (assumed to be zero). Solving this balance for the propane gas transfer velocity gives

$$k_{prop.} = \frac{2Ud(G_1 - G_2)}{L(G_1 + G_2)} - k_{sed.} \quad (6)$$

This solution to the mass balance of salt and propane resulted in propane gas transfer velocities that were within 5% of those calculated using the conventional approach (from the relative ratios of the gas and salt tracer concentrations; Wanninkhof 1990; Marzolf et al., 1994). Due to the greater molecular diffusivity of oxygen relative to propane the oxygen gas transfer velocity was calculated as 1.39 \* the propane gas transfer velocity (Rathbun et al., 1978).

The timing of conductivity measurements and propane sample collection was aligned with the mean water transit time along the reach to make measurements in the same body of water. Conductivity was determined with a YSI 30 handheld conductivity sensor. Ten samples for propane analysis were collected in rapid succession at each site with a 5 ml syringe. Five milliliters of water were injected into an evacuated vacutainer and the sample was refrigerated until analyzed on a gas chromatograph with a flame-ionization detector. Stream discharge was determined according to the continuity equation from the diluted salt concentration at the upstream end of the reach given the

known rate of salt introduction (e.g. Roberts et al., 2007). A relationship between stream stage and each of the calculated rates of stream discharge, water velocity, and the gas transfer velocity was determined to extrapolate each of the calculated rates across the time series.

The oxygen concentration in the stream was measured with Hach Intellical Rugged LDO probes which logged to HQ40D handheld meters. The oxygen saturation concentration was calculated by the device as a function of stream temperature and atmospheric pressure. Linear corrections to the oxygen observations were applied to correct for sensor drift during deployment.

#### *Metabolism Calculations*

The metabolic fluxes of respiration (R), gross primary production (GPP), and net ecosystem metabolism (NEM) were determined by binning the calculated oxygen fluxes by their occurrence during the day or at night. Daytime was defined as having a detectable level of light ( $PAR \geq 0.01 \mu\text{mol m}^{-2} \text{s}^{-1}$ ). Daytime and nighttime fluxes were separately summed to determine the ecosystem metabolic fluxes. Because oxygen fluxes were calculated at a 15 minute frequency, yet were extrapolated to daily rates, the sums of nighttime and daytime oxygen fluxes were divided by 96, the number of 15 minute intervals per day. Respiration was calculated according to Hume et al., (2010) as

$$R = \frac{1}{96} \left( \sum flux_{Dark} + \frac{\sum flux_{Dark}}{h_{Dark}} h_{Light} \right), \quad (7)$$



where  $flux_{Dark}$  are the calculated oxygen flux at night every fifteen minutes,  $h_{Dark}$  are the number of nighttime hours and  $h_{Light}$  are the number of daytime hours. This calculation extrapolates nighttime respiration rates to the day, implicitly assuming that in the daytime there is no increase in respiration. The calculation of gross primary production follows from the assumption of the daytime respiration rate being equal to the nighttime respiration rate. It was calculated as

$$GPP = \frac{1}{96} \left( \sum flux_{Light} + \frac{|\sum flux_{Dark}|}{h_{Dark}} h_{Light} \right), \quad (8)$$

where  $flux_{Light}$  are the calculated rates of oxygen flux during the day every fifteen minutes. Net ecosystem metabolism, the balance of R and GPP was calculated simply as the sum of the nighttime and daytime fluxes. Specifically, NEM was defined as

$$NEM = \frac{1}{96} (\sum flux_{Dark} + \sum flux_{Light}). \quad (9)$$

Net ecosystem metabolism is the metabolic rate which describes the degree to which the system is supported by external, or previously stored, sources of organic matter. A concern with the methodology for dividing fluxes by the presence or absence of light is the surplus in dissolved oxygen concentration in the water column due to photosynthesis that may persist after dark. The contribution of this surplus dissolved oxygen to metabolic rates is small, however.

The rapid uptake of dissolved oxygen at the sediment-water interface caused by storm events is a distinct process from the usual diurnal fluctuation in dissolved oxygen in the stream and it occurs irrespective of day-night cycles. In order to accurately account for GPP and R during these intervals, daytime R was interpolated between pre-dawn and post-sunset rates (as per Houser et al., 2005; Roberts et al., 2007). Or, in the event of a daytime storm, R was interpolated from pre-dawn rates to the point where R exceeded them. In those instances R was determined simply as the average of observed and interpolated rates of oxygen uptake over the 24 hour period.

## Results

### *Stream Attributes: Physical and Chemical*

The predominant bed type in Rattrap Branch was medium-grained sands with a low (0.3%) organic matter content. The measurement error presented below and throughout this study represents the standard error. The mean grain sizes at the 10<sup>th</sup>, 50<sup>th</sup>, and 90<sup>th</sup> percentiles were  $212 \pm 14 \mu\text{m}$ ,  $380 \pm 25 \mu\text{m}$ , and  $735 \pm 102 \mu\text{m}$ , which correspond to fine, medium, and coarse sands, respectively. Finer sediments were present in the bottom of pools. The hydraulic conductivity of the sands was  $1.1 \times 10^{-4} \text{ m s}^{-1}$  at a site in the main channel and  $4.9 \times 10^{-5} \text{ m s}^{-1}$  in a stream riffle with a higher proportion of fines.

During both spring sampling periods in 2011 and 2012 abnormally-dry to moderate drought conditions were reported for the southern portion of Accomack County, the region including the study site (U.S. Drought Monitor, 2013). These

conditions recurred or intensified during the following summers, but by the fall of 2011 and 2012 soil moisture conditions had returned to normal. Soil moisture conditions were also normal in the fall of 2010. Stream discharge determined during the sampling periods followed a related seasonal pattern. Discharge was at an annual minimum during summers with a mean of  $35.6 \pm 6.6 \text{ L s}^{-1}$ , and at an annual maximum in fall with a mean of  $57.3 \pm 3.2 \text{ L s}^{-1}$ . However, the variation between fall, winter, and spring was minimal. Mean stream discharge in the winter and spring were  $50.2 \pm 0.7 \text{ L s}^{-1}$ , and  $49.6 \pm 3.0 \text{ L s}^{-1}$ , respectively.

The mean concentration of nitrate in the stream was high at  $300 \pm 35 \text{ } \mu\text{M}$ . Nitrate concentrations were not significantly different between higher flow conditions in winter and in the low flow conditions in summer. Ammonium was a small fraction of the dissolved inorganic nitrogen in the stream with a mean annual concentration of  $1.2 \pm 1.0 \text{ } \mu\text{M}$ . Organic nitrogen concentrations in the water column were generally less than 10% of the nitrate concentration. Phosphate and dissolved organic phosphorous concentrations, in contrast, did vary between low flow conditions in the summer and high flow conditions in the winter. The phosphate and dissolved organic phosphorus concentrations were greater in the summer at  $0.32 \pm 0.01 \text{ } \mu\text{M}$ , and  $0.98 \pm 0.08 \text{ } \mu\text{M}$ , respectively, than in the winter when the concentrations were  $0.17 \pm 0.02 \text{ } \mu\text{M}$  and  $0.66 \pm 0.09 \text{ } \mu\text{M}$ .

### *Stream Attributes with Stage*

Stream discharge, mean stream velocity and the gas transfer velocity were all extrapolated across the time series as a function of stream stage. This relationship was complicated by a stage-discharge shift that occurred on June 2, 2012 when an intense low pressure system passed over the study area. Six centimeters of rain fell overnight causing local flooding. Fifteen centimeters of sand removal caused by the resulting flood wave was recorded at one site in Rattrap Branch by exposure of a PVC pipe inserted into the thalweg to support a logger.

The occurrence of the storm was associated with a stage shift in the stream that caused changes in the relationship between stream discharge and stage (Figure 1A). In the summer and fall of 2011 the mean stream stages were  $15.1 \pm 0.4$  cm and  $21.2 \pm 0.7$  cm. In the summer and fall of 2012 the mean stream stages had fallen to  $10.5 \pm 0.5$  and  $17.2 \pm 0.7$  cm, respectively, drops of 4.6 and 3.9 cm. This decrease in the mean stage, however, occurred with an increase in the mean rate of discharge. In the summer and fall of 2011 mean discharge was  $23.3 \pm 1.2$  and  $49.4 \pm 2.4$  L s<sup>-1</sup>, respectively. In the summer and fall of 2012 the mean discharge was  $38.5 \pm 8.1$  and  $69.8 \pm 5.8$  L s<sup>-1</sup>. Under low-flow conditions (defined here as when changes in stream stage were less than 2 cm per day), the pattern was the same. Low flow discharge in the summer of 2011 was unchanged,  $23.3 \pm 1.2$  (n = 7), but in the fall it increased to  $40.4 \pm 0.6$  L s<sup>-1</sup> (n = 7). In the summer and fall of 2012 low-flow discharge was  $21.7 \pm 2.0$  L s<sup>-1</sup> (n = 20), and  $58.2 \pm 1.8$  L s<sup>-1</sup> (n = 7), respectively.

As with stream discharge, stream velocity was extrapolated across the time series as a function of stream stage. The change in the stage-discharge relationship co-occurred with changes in the relationship between stage and stream velocity (Figure 1B).

Following the stage shift, relatively small changes were seen in the mean non-storm stream velocity and gas transfer velocity. In the summer of 2011 a non-storm mean stream velocity of  $8.7 \pm 0.2 \text{ cm s}^{-1}$  was observed. Applying observations of the stage and stream velocity made after June 1, 2012 an increase was observed in the summer of 2012 to a mean, non-storm rate of  $13.2 \pm 0.1 \text{ cm s}^{-1}$ . A smaller increase in stream velocity was seen in the fall. In the fall of 2011 the mean stream velocity was  $13.2 \pm 0.3 \text{ cm s}^{-1}$ . In the fall of 2012 it increased to  $14.5 \pm 0.1 \text{ cm s}^{-1}$ .

The gas transfer velocity was also extrapolated across the time series as a function of stream stage. Before and after the stage-shift in June 2012 the gas transfer velocity increased with increases in stage, which corresponded with increases in both discharge and water velocity. After the stage shift, with the substantial drop in stream stage, a drop in the gas transfer velocity was also observed. The mean non-storm gas transfer velocities in the summer and fall of 2011 were  $3.4 \pm 0.2 \text{ m d}^{-1}$  and  $6.3 \pm 0.4 \text{ m d}^{-1}$ , respectively. After the stage shift these rates decreased to  $2.9 \pm 0.2 \text{ m d}^{-1}$  and  $5.9 \pm 0.3 \text{ m d}^{-1}$ .

#### *Variation in Metabolism on Diurnal Time-Scales*

In the absence of storms, oxygen concentration peaked daily in the early afternoon, generally co-occurring with a daytime peak in temperature (Fig. 2D). Oxygen concentrations responded to PAR during the day. At night there was variation in the

timing of the dissolved oxygen minimum. It generally occurred either within a few hours of dark and then increased with increasing oxygen saturation as temperatures cooled throughout the night, but at times it also occurred shortly before dawn. The oxygen concentration was generally less than saturation in the stream. In the solution for the benthic oxygen flux (Eq. 1), the flux of oxygen across the air-water interface was the dominant term. Storage of oxygen in the water column was never more than a small percentage of the benthic flux. While diurnal GPP caused substantial deviation in oxygen concentration from the nighttime rate of uptake, the amount of production was relatively small compared to rates of respiration (e.g., Figure 2D).

Net ecosystem metabolism is the balance of GPP and R. The variation in GPP and R within seasons was of a comparable magnitude to the variation across seasons (Figure 3). Throughout the study NEM was always negative with the daily magnitude of GPP never exceeding that of R. Much of the variance in NEM could be described in terms of R. The mean value of NEM was equivalent to 85% of R.

Storms were responsible for much of the variation in metabolism seen within sampling seasons. Storm-induced variation in discharge was substantial. As an example, the maximum stream stage recorded during the study interval was July 14, 2012 at 66 cm, likely corresponding to a discharge rate of greater than  $165 \text{ L s}^{-1}$  (one-half of the discharge by linear extrapolation). Four days later discharge in the stream had decreased to  $22 \text{ L s}^{-1}$ . Smaller storms also cause substantial variation in oxygen flux, and in the associated GPP, R, and NEM. With an increase in stage following a rain event there are corresponding increases the mean stream velocity and in the gas transfer velocity. As a

result, the magnitude of respiration may increase substantially following a rain event (Figure 4). Elevated respiration rates were often observed to last more than 24 hours after the storm event occurred.

#### *Variation in Metabolism on Seasonal Time-Scales*

Over seasonal time scales the greatest magnitude rates of both GPP and R were observed in the spring, while the smallest rates of GPP and R were observed in the summer (Figure 5). Metabolic processes in rivers are linked to hydrology, but the high average magnitude of GPP and R in the spring were not coincident with the greatest mean discharge or stream velocities, which occurred in the fall. The smallest magnitude GPP and R was in the summer, however, both stream discharge and stream velocity were at their annual minima in the same season. Seasonal variation in stream temperature varied from summertime midday temperatures in excess of 25 °C, and winter nighttime temperatures as low as 6 °C.

Because of the high diurnal variation in oxygen flux caused by rain events, there is potential for those observations to bias the mean seasonal rates of metabolism. While smaller storms may affect metabolic rates for a few hours, larger storms can have an impact that lasts days after the rain event occurs. In order to investigate the impact of storms on the seasonal averages, the mean low-flow metabolic rates were also determined. Low-flow was defined here as a period of two or more days in which the stream stage varied by less than 2 cm. Generally, this condition was met within 1.5 days after small storms occurred and 3 days after larger storms. The exclusion of storm events

diminished the magnitude of R from  $-307 \pm 83 \text{ mmol m}^{-2} \text{ d}^{-1}$  to  $-213 \pm 34 \text{ mmol m}^{-2} \text{ d}^{-1}$  ( $n = 8$ ), though the effect on the mean rates of GPP was small. Under low-flow conditions ecosystem respiration was smaller, and as a result NEM was also smaller in magnitude (Figure 5). The differences were significant in spring, summer, and fall. The winter included the least overall observations and among those, one small storm. As a proportion of the total, storms were responsible in the spring, summer, and fall for 42%, 41%, and 32% of NEM, contributing substantially to the heterotrophy of the system.

The ratio of GPP:R is descriptive of the proportion of community respiration that is supported by primary production within the system. The mean annual rate of GPP:R was 0.25, but seasonal variation was substantial. The ratio of GPP:R in the winter and spring were 0.32 and 0.35, while in the summer and fall the ratios were 0.12 and 0.11, respectively. These ratios are driven in large part by the changes in GPP, which declined substantially in summer and fall. Under low-flow conditions, without enhancement of respiration by storm events, the ratio of GPP:R was less heterotrophic. In winter and spring the low-flow ratios were 0.33 ( $n = 5$ ) and 0.45 ( $n = 14$ ), while in the summer and fall they were 0.20 ( $n = 27$ ) and 0.15 ( $n = 16$ ), respectively. Based on these ratios, almost half of R may be fueled by autotrophic production within the stream under low-flow conditions in the spring, but less than one-sixth is in the fall.

#### *Variation in Metabolism with Stage Shift*

Season was not the only important factor in describing interannual variation in metabolic fluxes. Coincident with the shift in the stage-discharge relationship in the stream was a



change in the mean rate of GPP which persisted from the beginning of summer sampling in 2012 through the end of sampling in the fall. In the summer of 2011 the mean rates of GPP under low-flow conditions were  $47 \pm 2 \text{ mmol m}^{-2} \text{ d}^{-1}$  ( $n = 7$  days). In the fall of 2011 the metabolic rates under low-flow conditions increased to  $59 \pm 5 \text{ mmol m}^{-2} \text{ d}^{-1}$  ( $n = 7$ ). The following summer, after the stage shift was observed, the mean rates of GPP under low-flow conditions fell to less than half of the prior summer's mean rate, at  $20 \pm 2 \text{ mmol m}^{-2} \text{ d}^{-1}$  ( $n = 20$ ). Similarly, the rate of GPP under low flow conditions in the fall of 2012 ( $23 \pm 4 \text{ mmol m}^{-2} \text{ d}^{-1}$ ;  $n = 7$ ) was less than half the rate in the fall of 2011. The reduction in GPP was evident in a reduced diurnal variation in the oxygen concentration in the water column in mid and late 2012 relative to the variation that was observed at the same time of year in 2011 (Figure 6).

The consistent decrease in GPP following the stage shift did not co-occur with consistent shifts in PAR or temperature, nor with the hydrologic property of stream discharge. No significant change in solar radiation under low flow conditions from the summer of 2011 ( $9.6 \pm 1.2 \text{ mol m}^{-2} \text{ d}^{-1}$ ) to the summer of 2012 ( $8.7 \pm 0.5 \text{ mol m}^{-2} \text{ d}^{-1}$ ), and an increase in solar radiation from the fall of 2011 ( $3.3 \pm 0.6 \text{ mol m}^{-2} \text{ d}^{-1}$ ) to the fall of 2012 ( $4.3 \pm 0.2 \text{ mol m}^{-2} \text{ d}^{-1}$ ). Similarly, temperatures did not change consistently before and after the stage shift. There was an increase in mean low-flow daytime temperatures of  $1.1 \text{ }^{\circ}\text{C}$ , to  $25.4 \text{ }^{\circ}\text{C}$ , between the summer of 2011 and the summer of 2012, but a decrease of  $1.9 \text{ }^{\circ}\text{C}$  in both daytime and nighttime mean temperatures between the fall of 2011 and the fall of 2012. As discussed under Physical Attributes, above, when storm events were included in seasonal averages there was an increase in mean discharge

for both the summer and fall observations following the stage shift. Under low-flow conditions there was no significant difference between the summer sampling periods of 2011 and 2012, but there was an increase in discharge between the fall sampling periods.

Two stream parameters which did change consistently with the change in stage were stream velocity, which increased, and the gas transfer velocity, which decreased. The pattern is evident in the non-storm, low-flow observations, in which mean water velocities increased from  $8.7 \pm 0.2 \text{ cm s}^{-1}$  in the summer of 2011 to  $13.1 \pm 0.1 \text{ cm s}^{-1}$  in the summer of 2012. Similarly, low-flow velocities increased from  $11.6 \pm 0.1 \text{ cm s}^{-1}$  in the fall of 2011 to  $14.3 \pm 0.1 \text{ cm s}^{-1}$  in the fall of 2012.

Despite the significant changes in GPP with the stage shift, the changes in R under low-flow conditions were less consistent. Between the summer of 2011 and the summer of 2012 the low-flow rate of respiration decreased from  $157 \pm 11 \text{ mmol m}^{-2} \text{ d}^{-1}$  to  $132 \pm 10 \text{ mmol m}^{-2} \text{ d}^{-1}$ . However from the fall of 2011 to the fall of 2012 there was an increase in R from  $269 \pm 12 \text{ mmol m}^{-2} \text{ d}^{-1}$  to  $331 \pm 15 \text{ mmol m}^{-2} \text{ d}^{-1}$ . This increase was consistent with increases in discharge and stream velocity over the same period.

### *Drivers of Metabolism*

Diurnal oxygen fluxes are driven by PAR and temperature. Aggregated over annual time-scales, however, PAR was a weak predictor of the daily rate of GPP. Gross primary production was at an annual minimum in the summer, and roughly doubled over that summertime rate in the fall (Figure 5). These seasons saw the lowest rates of GPP even prior to the stage shift, but the rates were reduced further following the stage shift (Figure

7). Gross primary production was greater in the winter, despite a reduction in PAR over what was measured at the stream bed in the summer and a similar amount of PAR as was observed in the fall. In the spring, however, a maximum in GPP co-occurred with a maximum in PAR.

Similar to observations of the relationship of GPP with PAR, water velocity was a weak predictor of diurnal rates of GPP aggregated over the entire time series. However, the correlation between GPP and water velocity was significant in portions of the time series. Because of the reduction in GPP that occurred with the stage shift, rates of GPP were compared not only across seasons, but also by their occurrence before or after the stage shift. No relationship was observed between non-storm GPP (days of minor storms that caused less than 0.5 cm of rain were included) and velocity for the summer, fall, or winter of 2011 (Figure 8), but there was a significant increase in non-storm GPP with water velocity in the spring (combined 2011 and 2012;  $n = 25$ ,  $r^2 = 0.728$ ,  $p < 0.0001$ ), and significant increases in non-storm GPP with water velocity in the summer and fall of 2012 ( $n = 25$ ,  $r^2 = 0.420$ ,  $p = 0.000456$ ; and  $n = 7$ ,  $r^2 = 0.926$ ,  $p = 0.00052$ ).

Most of the variation in diurnal rates of ecosystem respiration over the two-year study was explained by water velocity alone. All observations, including storm events, were included in the analysis. With the stage shift there was increase in velocity at low to moderate rates of stream discharge. Despite the divergence in stream velocities, R at these two different stream velocities was similar, indicating that processes other than velocity were also important in controlling R (Figure 9). In each case, the trajectory of R was closely linked to increases in stream velocity. Prior to the stage shift a parabolic fit of

the observations of R as a function of velocity explained 90% of the diurnal variance across six seasons (the fall of 2010, the spring, summer, fall, and winter of 2011, and the spring 2012;  $n = 63$ ). During that time, R in the spring was generally greater than that predicted by the parabolic fit to velocity, while R in the fall and winter of 2011 was less than that predicted by velocity. Following the stage shift, a linear fit of R to velocity explained 96% of the diurnal variance in R across the summer and fall of 2012 ( $n = 40$ ). As velocities increased from low-flow to storm-flow conditions the different rates of R, observed before and after the stage shift, converged. Velocity was determined from stream stage, so the parabolic and linear relationships of R as a function of velocity were matched by R as a function of stage.

## **Discussion**

### *Stream Attributes: Physical and Chemical Parameters*

The high concentration of nitrate in the stream ( $300 \pm 35 \mu\text{M}$ ) was consistent with the nitrate concentrations in the same stream determined by Luckenbach et al. (2008; referred to as Upper Finney), and places it in the range of nitrate concentrations observed in a survey of 14 eastern shore streams conducted by Stanhope et al. (2009), of which the mean concentration was in excess of  $100 \mu\text{M}$ . Because phosphate concentrations were relatively low (median of  $0.48 \mu\text{M}$ ) and far below the stoichiometric Redfield ratio with nitrogen, phosphorus may limit heterotrophic respiration and autotrophic production when conditions are otherwise favorable for growth.

### *Stream Attributes with Stage*

The observations of stream velocity that were made across moderate stream stages in Rattrap Branch indicated that velocity in this stream can be predicted accurately from stage, although velocity during storm conditions were extrapolated from this relationship. Similarly, the gas transfer velocity may also be predicted from stage (e.g., Roberts et al., 2007). The gas transfer velocity is a function of turbulence in aquatic systems, to the degree that across aquatic ecosystems the gas transfer velocity scales with the turbulent dissipation rate to the  $\frac{1}{4}$  power (Zappa et al., 2007). As stream discharge increases, turbulence increases, so we would expect to see a dependency of the gas transfer velocity on stage. Based on our observations across a range of stage heights this approximation was appropriate in Rattrap Branch.

Stage discharge shifts occur frequently in rivers and streams flowing through unconsolidated alluvial deposits (Hershy, 1995). Channel roughness (incorporating elements of channel geometry), channel sinuosity, and energy slope can all be altered by conditions that commonly occur during floods. Morphologically, the stage shift was consistent with a scouring of sands from the thalweg, as observed following the storm. As a result of this, a greater proportion of stream flow would be restricted to the smaller area of the thalweg following the stage shift. This idea can be tested by applying the continuity equation, of which the velocity and the stream discharge are known, to solve for the mean cross sectional area. Prior to the stage shift, at a stream discharges of  $15 \text{ L s}^{-1}$  and  $50 \text{ L s}^{-1}$  (to bracket the range of moderate flow), the cross sectional area of flow

would have been  $0.20 \text{ m}^3$  and  $0.38 \text{ m}^3$ , respectively. Following the stage shift, the stream cross sectional area at the low end would have decreased to  $0.12 \text{ m}^3$ . This is consistent with a greater proportion of the flow being confined to the thalweg. At the higher discharge,  $50 \text{ L s}^{-1}$ , the cross sectional area was unchanged at  $0.37 \text{ m}^3$  consistent with a greater proportion of the channel becoming incorporated in flow. As a result, cross sectional areas before and after the stage shift converge at high levels of discharge. The confinement of more flow to the thalweg was supported by observations of stream bed scouring during the June 2, 2012 storm and was also supported by visual changes in the distribution of flow across the stream bed channel. Pictures from a stream bend taken in July of 2011 and in July of 2012 illustrate that stream discharge was distributed across the stream bed channel in July of 2011 ( $Q = 30 \text{ L s}^{-1}$ ), relative to July of 2012 when stream discharge, although smaller in magnitude ( $Q = 20 \text{ L s}^{-1}$ ), was largely confined to the thalweg (Figure 10).

Morphological changes that co-occurred with the change in stream stage may offer a partial explanation for the persistent reduction in GPP in the summer and fall of 2012. The bed scour that occurred in the thalweg which allowed stream stage to drop while supporting the same discharge would have removed rooted plants and algae from that central channel. Following the storm, with the return to base flow rates of stream discharge, stream velocities remained substantially higher than they were prior to the storm. The greater rates of stream velocity, consistently in excess of  $12 \text{ cm s}^{-1}$ , would enhance bedload transport along the thalweg, making recovery of plant and algal abundance along it more difficult. Rooted aquatic plants and algae were still abundant

within the stream channel but were rooted mostly outside of the thalweg after the stage shift (Figure 10). The reduction in water level created an environment more favorable to emergent species there. State changes like these complicate prediction of ecosystem metabolism.

#### *Determination of Metabolic Rates*

The daytime rate of respiration was assumed to be equal to the nighttime rate of respiration, yet the true daytime respiration rate is likely to be greater than this. The increase in daytime R would be due to increases in daytime temperature (Brown et al., 2004), increases in respiration by primary producers, and increased respiration in heterotrophs due the production and availability of photosynthates (Kaplan and Bott, 1982; Baines and Pace, 1991). Increases in daytime respiration rates have been observed where methods capable of identifying it have been applied (e.g., Sugar Creek, Indiana; Tobias et al., 2007). Despite these known increases in daytime respiration we have assumed equality between day and night because the potential for introducing systematic error through the assumption of an enhanced rate is substantial. Because of this assumption, true GPP may be substantially greater than these reported rates. Tobias et al. (2007) observed via isotopic measurement an increase in daytime respiration rates of up to 50%. While incorporating a daytime increase in R would not affect the resulting NEM because it would be exactly offset by increases in GPP, it would reflect a greater role for the support of in stream biological processes by primary production.

*Variation in Metabolism on Diurnal Time-Scales*

The high diurnal variance in GPP, R, and NEM over the course of the study was largely due to the occurrence of rain events. The net effect of rain events was to enhance heterotrophy by both the suppression of GPP and an enhancement of R (Figure 4). While other studies have focused on major storms and have found multi-day suppression of GPP with a gradual recovery following major rain events (Uehlinger, 2006; Roberts et al., 2007), the suppression of GPP in Rattrap Branch lasted typically only the duration of the flood wave, corresponding with a suppression in PAR due to suspended material. The more important effect of rain events on NEM in Rattrap Branch was the enhancement of R. A primary mechanism for the enhancement of R following a rain event that may be overlooked is by the simple increase in water velocity. As water velocities increase with a flood wave hyporheic exchange, a dominant mechanism responsible for respiration in shallow streams, increases (Packman et al., 2004; Janssen et al., 2005). Other in-stream processes are also likely to contribute. With the increase in discharge and velocity the stream bed is mobilized, releasing stored pore water as well as exposing more pore water to exchange. Clogging layers of sediment that restrict pore water exchange are removed (Schachli, 1992), and high concentrations of organic matter are suspended which may additionally enhance in-stream and hyporheic respiration rates (Jones, Fisher and Grimm 1995; Naegeli et al., 1995, Buffam et al., 2001). Additional mechanisms for the increase in R may include the storm-induced influx of groundwater and pore water which would appear as stream R yet would be due to respiration in aquifers or surficial groundwaters. Inflowing groundwater and bankflow are likely hypoxic, and contribute a respiration



signal that occurred in the vadose zone or the aquifer to the stream. The flood wave may also cause the temporary storage of stream water in the stream banks, where oxygen may be consumed prior to its reentry to the stream (Gu et al., 2008). These processes are difficult to decompose from dissolved oxygen concentrations, but may all contribute to the high rates of respiration observed from hours to days after storm events.

The cumulative effect of storms was to significantly increase heterotrophic respiration over respiration rates observed at baseflow in every season in which storms were observed. Based on our observations, a sampling regimen in a similar stream that does not incorporate sampling during episodic storm events may underestimate heterotrophy by 40%. The high diurnal variance in oxygen fluxes due to storms document that multi-week sampling intervals are important for accurately quantifying ecosystem metabolism.

#### *Variation in Metabolism on Seasonal Time-Scales*

On an annual basis, the proportion of community respiration supported by autotrophic production in the stream was 25%; the proportion of R:GPP was 4:1. This indicates that the stream receives a high degree of subsidy from the surrounding watershed. From season to season the variation in this subsidy was substantial, following patterns that have been observed in other streams. Gross primary production was greatest in the spring, as has been observed in a stream near the Mediterranean in Spain, (Acuna et al., 2005) as well as in Piedmont and mountainous streams in Georgia and Tennessee of the southeastern U.S. (Houser et al., 2005; Roberts et al., 2007). A combination of increasing

light and ample stream stage may contribute to this pattern (e.g. Houser et al., 2005). In the summer the same factors may act to bring GPP to an annual minimum. Fully developed forest canopies restrict the penetration of light to the stream, and high rates of evapotranspiration may reduce the stream stage, reducing the volume and flow rate of water available to autotrophic organisms.

The greatest rate of respiration in Rattrap Branch was also observed in the spring, although rates were similar across winter, spring and fall. Spring peaks in respiration rates also occur in ten Piedmont streams and a blackwater river in Georgia (Houser et al., 2005; Meyer and Edwards 1987) and in a mountain stream in Tennessee (Roberts et al., 2007). The peaks in respiration in the streams, excluding the blackwater river, co-occurred with peaks in primary production, and indicate the importance of GPP as a fuel for R. The rates of R in Rattrap Branch, in contrast, were similarly high in the fall and winter. The minimum rates of R that occurred in the summer in Rattrap Branch also matched what occurs in ten Piedmont streams, a mountain stream in Tennessee, and a stream on the Spanish Mediterranean. This suggests that while temperature was a driver of respiration, it exerted less control over respiration than other factors did. Among the other common factors in all of the listed streams is a summertime minimum in stream discharge. Yet, to our knowledge, the summertime minimum in stream velocity has not been described as a cause of the co-occurring minimum in R.

### *Significance of NEM*

Marcarelli et al., (2011) examined the proportion of GPP:R in over two hundred streams for which open water oxygen fluxes were available. While the annual average ratio of GPP:R for Rattrap Branch is close to the mean GPP:R predicted by an empirical relationship with discharge that fit those observations, the magnitude of the rates is in excess of many otherwise comparable streams. Compared with the smaller Walker Branch in Tennessee (Roberts et al., 2007), and a survey of 10 tributary streams near Columbus Georgia (Houser et al., 2005), Rattrap Branch had about four times their mean rates of R. Further, in a survey of 72 streams sampled in spring and summer across eight regions of the United States, the average rate of R was  $220 \text{ mmol m}^{-2} \text{ d}^{-1}$ , less than the mean rate observed in Rattrap Branch ( $307 \pm 83 \text{ mmol m}^{-2} \text{ d}^{-1}$ ;  $n = 8$ ). One highly studied stream that does typically have a greater rate of respiration than Rattrap Branch is Sycamore Branch, in the desert southwest. Sycamore Branch has served as a study site for hyporheic exchange, as it has a sand and gravel bed which is conducive to high rates of pore water exchange which drives the high rates of respiration observed there (Valett et al., 1990).

### *Drivers of GPP*

Little of the seasonal variation in GPP could be explained by PAR. In the spring rates of production increased and PAR was at its peak, but despite the clear evidence of PAR as a driver of oxygen flux at diurnal time-scales no correlation was observed at greater time

scales. In Walker Branch Roberts et al. (2007) observed clear control of GPP by PAR in the spring, although not in other seasons. The lack of predictability in other seasons, and in Rattrap Branch, indicates that other factors exerted primary control. Among other factors that may be important are autotrophic biomass, stream stage for inundation of vegetation, and water velocity. Stream velocities did explain a significant amount of the variation in GPP in the spring of 2011 and 2012, and the summer and fall of 2012 (Figure 8). As stream velocities increased so did GPP in those seasons. In the summer and fall of 2012 increases in stream velocity would have coincided with greater inundation of vegetation. In the spring, vegetation was inundated at low to moderate flows (e.g., Figure 10 with  $30 \text{ L s}^{-1}$  of discharge). During the spring aquatic plants were at their densest and so too are aquatic algae which entwine rooted plants. These algae substantially reduce flow in their vicinity (Dodds, 2003), as a result restricting exchange between the main stream and both plants and algal tissues. With increases in flow velocity, boundary layers are compressed and greater rates of exchange of nutrients, carbon dioxide, and oxygen occur (Glud, 2008). Because of the consistency between daytime and nighttime water velocities, the velocity enhancement of GPP could be resolved from the enhancement of R by the same processes.

### *Drivers of Respiration*

Velocity was highly important in determining respiration rates in Rattrap Branch. Water velocity explained 90% of the changes in R across six seasons, and 96% of the variance across two seasons following the stage shift (Figure 9). One mechanism which would

drive an increase in  $R$  with an increase in velocity regardless of season is hyporheic exchange. Chamber experiments have shown that hyporheic exchange is responsible for most of  $R$  in a sand-bed and gravel-bed stream (Fuss and Smock, 1996; Naegeli and Uehlinger, 1997). Wondzell and Swanson (1996) identified a clear relationship between increases in stream discharge and increases in large-scale (tens of meters) hyporheic exchange in a gravel bed river in Oregon. The length scales of hyporheic exchange in Rattrap Branch would be smaller in the medium-grained sands that comprise the bed, but pore water exchange across a wide range of permeable sediments is predictable and is driven by pressure gradients which increase with the square of water velocity (Packman and Salehin, 2003).

Despite the clear mechanism of velocity driving oxygen uptake, the increase in water velocity that occurred with the stage shift did not correspond with an increase in  $R$ . Macrophyte removal and changes to the cross-sectional area of flow may explain this. Macrophytes were removed by scouring and regrowth may have been suppressed by the higher water velocity that occurred after the stage shift. The reduction in macrophytes would also lead to a reduction in  $R$ . Gross primary production represented 30% of  $R$  in the summer and 16% of  $R$  in the fall prior to the stage shift. A morphological factor which may have controlled  $R$  was the reduction in cross sectional area of flow following the shift. This would have co-occurred with a reduction in the wetted area and may have reduced the influence of hyporheic exchange on oxygen concentration. The convergence of rates of  $R$  at greater water velocities (and greater rates of discharge) may follow from the convergence of the mean cross-sectional area at greater rates of discharge.

To determine fluxes of oxygen this study relied on a determination of both velocity and gas transfer from stream stage. This approach reflects a physical relationship between stage, stream velocity, and the gas transfer velocity. To examine the degree to which variation in the gas transfer velocity could drive the relationship between velocity and R, the respiration rate was recalculated using a fixed gas transfer velocity. In effect, this calculation consistently assumes that turbulence is not enhanced by increases in water velocity. Despite this assumption, velocity explained 40 % of the variance in the recalculated R before the stage shift and 72% of the variance after it ( $p < 0.0001$  in both cases). The physical relationship between velocity and the gas transfer velocity would improve this correlation, bringing it closer to what was observed.

Water velocity drives hyporheic exchange, but there are other processes which may contribute to the relationship between velocity and R in Rattrap Branch. Rain water, via runoff and subsurface throughflow, may transport substantial highly labile organic material into streams. At higher water velocities alluvial sediments are also transported, causing resuspension of finer particles and organics. The combination of internal and external sources of organic matter increases dissolved organic carbon and dissolved organic nitrogen concentrations in the stream and enhances respiration rates (Buffam et al., 2001).

Groundwater discharge to a stream may significantly bias R (McCutchan et al., 2002; Hall and Tank, 2005), and as groundwater inflow increases with discharge it likely contributes to the relationship between velocity and R. As an estimate of the rate of consumption of oxygen due to groundwater inflow, a simple mass balance of water in the

stream was solved as follows: Groundwater discharge was assumed to be equal to the stream discharge divided by the upstream creek length (5300 m). The resulting discharge per meter of stream length was divided by the average width of the stream near the point of measurement (2 m) for a specific rate of groundwater discharge. Groundwater inflow was assumed to be anoxic as anoxic conditions were observed in sands several centimeters below the stream bed. Based on these calculations, the average rate of specific groundwater discharge was  $0.37 \text{ m d}^{-1}$  prior to the stage shift and  $0.42 \text{ m d}^{-1}$  after the stage shift. These rates of groundwater inflow could account for an average of 23% of R before the stage shift and up to 30% of R after it, when the magnitude of R was smaller.

## **Synthesis**

Streams and headwaters are the most widespread components of fluvial networks. As such they are the initial recipients of most of exported terrestrial ecosystem production and are disproportionately responsible for its oxidation (Raymond and Butman, 2011; Battin et al., 2008). Regional changes in watershed and alluvial characteristics determine how metabolic processes respond to drivers, but if velocity-driven respiration is similarly important in other headwater streams flowing through unconsolidated alluvium, then watershed carbon budgets may be substantially improved with the incorporation of relationships with stream velocity.

## Literature Cited

- Baines SB, Pace ML. 1991. The production of dissolved organic matter by phytoplankton and its importance to bacteria: Patterns across marine and freshwater systems. *Limnology and Oceanography* 36:1078–90.
- Battin TJ, Kaplan L a., Findlay S, Hopkinson CS, Marti E, Packman AI, Newbold JD, Sabater F. 2009. Biophysical controls on organic carbon fluxes in fluvial networks. *Nature Geoscience* 2:595–595.
- Berg P, Long MH, Huettel M, Rheuban JE, McGlathery KJ, Howarth RW, Foreman KH, Giblin AE, Marino R. 2013. Eddy correlation measurements of oxygen fluxes in permeable sediments exposed to varying current flow and light. *Limnol Oceanogr* 58:1329–43.
- Berg P, Røy H, Janssen F, Meyer V, Jørgensen B, Huettel M, De Beer D. 2003. Oxygen uptake by aquatic sediments measured with a novel non-invasive eddy-correlation technique. *Marine Ecology Progress Series* 261:75–83.
- Björkman O. 1966. The effect of oxygen concentration on photosynthesis in higher plants. *Physiologia Plantarum* 19:618–33.
- Boynton W, Kemp W, Osborne C. 1981. Influence of water circulation rate on in situ measurements of benthic community respiration. *Marine Biology*.
- Boston H, Hill W. 1991. Photosynthesis-light relations of stream periphyton communities. *Limnology and oceanography* 36:644–56.
- Brown J, Gillooly J, Allen A, Savage V, West G. 2004. Toward a metabolic theory of ecology. *Ecology* 85:1771–89.



- Buffam I, Galloway JN, Blum LK, Mcglathery KJ. 2001. A stormflow / baseflow comparison of dissolved organic matter concentrations and bioavailability in an Appalachian stream. :269–306.
- Butman D, Raymond P a. 2011. Significant efflux of carbon dioxide from streams and rivers in the United States. *Nature Geoscience* 4:839–42.
- Cole JJ, Prairie YT, Caraco NF, McDowell WH, Tranvik LJ, Striegl RG, Duarte CM, Kortelainen P, Downing J a., Middelburg JJ, Melack J. 2007. Plumbing the Global Carbon Cycle: Integrating Inland Waters into the Terrestrial Carbon Budget. *Ecosystems* 10:172–85.
- Fonseca M, Kenworthy W. 1987. Effects of current on photosynthesis and distribution of seagrasses. *Aquatic Botany* 27:59–78.
- Fuss C, Smock L. 1996. Spatial and temporal variation of microbial respiration rates in a blackwater stream. *Freshwater Biology*:339–49.
- Gu C, Hornberger GM, Herman JS, Mills AL. 2008. Effect of freshets on the flux of groundwater nitrate through streambed sediments. *Water Resources Research* 44:1-12.
- Herschey R. 1995. *Streamflow Measurement*. Second edition. Taylor & Francis.
- Hilton J, O'Hare M, Bowes MJ, Jones JI. 2006. How green is my river? A new paradigm of eutrophication in rivers. *The Science of the total environment* 365:66–83.
- Houser J, Mulholland P, Maloney K. 2005. disturbance and stream metabolism: patterns in ecosystem respiration and gross primary production along a gradient of upland

soil and vegetation disturbance. *Journal of the North American Benthological Society* 24:538–52.

Jones J, Fisher S, Grimm N. 1995. Vertical hydrologic exchange and ecosystem metabolism in a Sonoran Desert stream. *Ecology*.

Kaplan L, Bott T. 1982. Diel fluctuations of DOC generated by algae in a piedmont stream. *Limnology and oceanography* 27:1091–100.

Hume AC, Berg P, Mcglathery KJ. 2011. Dissolved oxygen fluxes and ecosystem metabolism in an eelgrass ( *Zostera marina* ) meadow measured with the eddy correlation technique. 56:86–96.

Janssen F, Faerber P, Huettel M, Meyer V, Witte U. 2005. Pore-water advection and solute fluxes in permeable marine sediments (I): Calibration and performance of the novel benthic chamber system Sandy. *Limnology and Oceanography* 50:768–78.

Long M, Rheuban J, Berg P, Zieman J. 2012. A comparison and correction of light intensity loggers to photosynthetically active radiation sensors. *Limnol Oceanogr: Methods*:1–25.

Long M, Berg P, de Beer D, Zieman J.C. 2013. In situ coral reef oxygen metabolism: An eddy correlation study.

Luckenbach M, Ross P, Curry A, McKay L. 2008. Evaluating the relationship between impervious surfaces within watersheds and coastal water quality on Virginia's eastern shore. Report submitted to the Coastal Zone Management Program, Virginia Department of Environmental Quality. Richmond, VA.

- Landon M, Rus D, Harvey F. 2001. Comparison of instream methods for measuring hydraulic conductivity in sandy streambeds. *Ground Water* 38:870–85.
- Madsen J, Chambers P, James W. 2001. The interaction between water movement, sediment dynamics and submersed macrophytes. *Hydrobiologia*:71–84.
- Marzolf E, Mulholland P, Steinman A. 1994. Improvements to the diurnal upstream-downstream dissolved oxygen change technique for determining whole-stream metabolism in small streams. *Canadian Journal of Fisheries Science* 51.
- Naegeli MW, Uehlinger U. 2011. Contribution of the Hyporheic Zone to Ecosystem Metabolism in a Prealpine Gravel-Bed-River Contribution of the hyporheic zone to ecosystem metabolism in a prealpine gravel-bed river. 16:794–804.
- Packman AI, Salehin M, Zaramella M. 2004. Hyporheic Exchange with Gravel Beds: Basic Hydrodynamic Interactions and Bedform-Induced Advective Flows.:647–56.
- Parsons T, Maita Y, Lalli C. 1984. A manual of chemical and biological methods for seawater analysis. Pergamon Press. 173 pp.
- Rathbun R, Tai D, Shultz D, Stephens D. 1978. Laboratory studies of gas tracers for reaeration. *Journal of the Environmental Engineering Division* 104:3.
- Rheuban JE, Berg P, McGlathery K. 2013. Ecosystem metabolism along a colonization gradient of eelgrass (*Zostera marina* L.) measured by eddy correlation.
- Roberts BJ, Mulholland PJ, Hill WR. 2007. Multiple Scales of Temporal Variability in Ecosystem Metabolism Rates: Results from 2 Years of Continuous Monitoring in a Forested Headwater Stream. *Ecosystems* 10:588–606.

- Schälchli U. 1992. The clogging of coarse gravel river beds by fine sediment. *Hydrobiologia* 235/236:189-197.
- Stanhope JW, Anderson IC, Reay WG. 2002. Base flow nutrient discharges from lower delmarva peninsula watersheds of virginia, USA. *Journal of environmental quality* 38:2070–83.
- Tobias C, Bohlke J, Harvey J. 2007. The oxygen-18 isotope approach for measuring aquatic metabolism in high productivity waters. *Limnology and oceanography* 52:1439–53.
- Uehlinger U. 2006. Annual cycle and inter-annual variability of gross primary production and ecosystem respiration in a floodprone river during a 15-year period. *Freshwater Biology* 51:938–50.
- Wanninkhof R. 1990. Gas exchange rates for a first-order stream determined with deliberate and natural tracers. *Water Resources Research* 26:1621–30.
- Westlake D. 1967. Some effects of low-velocity currents on the metabolism of aquatic macrophytes. *Journal of Experimental Botany* 18:187–205.
- Young RG, Huryn AD. 1998. Comment: Improvements to the diurnal upstream-downstream dissolved oxygen change technique for determining whole-stream metabolism in small streams. *Canadian Journal of Fisheries and Aquatic Sciences* 55:1784–5.
- Zappa CJ, McGillis WR, Raymond P a., Edson JB, Hintsa EJ, Zemmelen HJ, Dacey JWH, Ho DT. 2007. Environmental turbulent mixing controls on air-water gas exchange in marine and aquatic systems. *Geophysical Research Letters* 34:L10601.

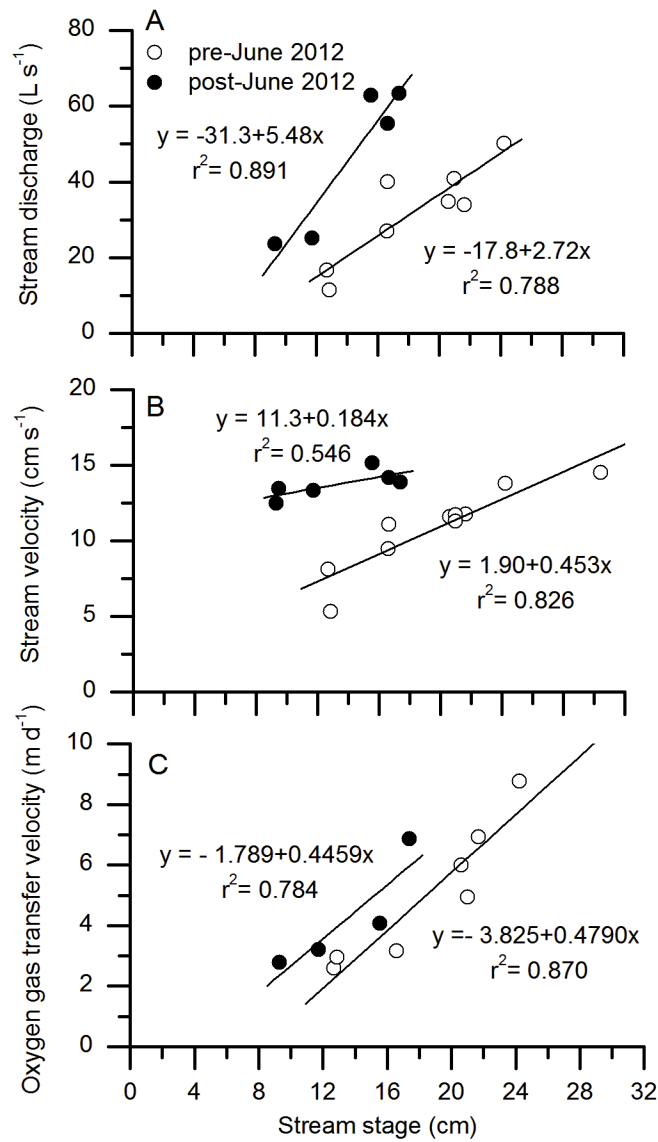


Figure 1. From stream stage the rates of **A** stream discharge, **B** the mean stream velocity, and **C** the oxygen gas transfer velocity were determined. A stage-discharge shift occurred in June of 2012.

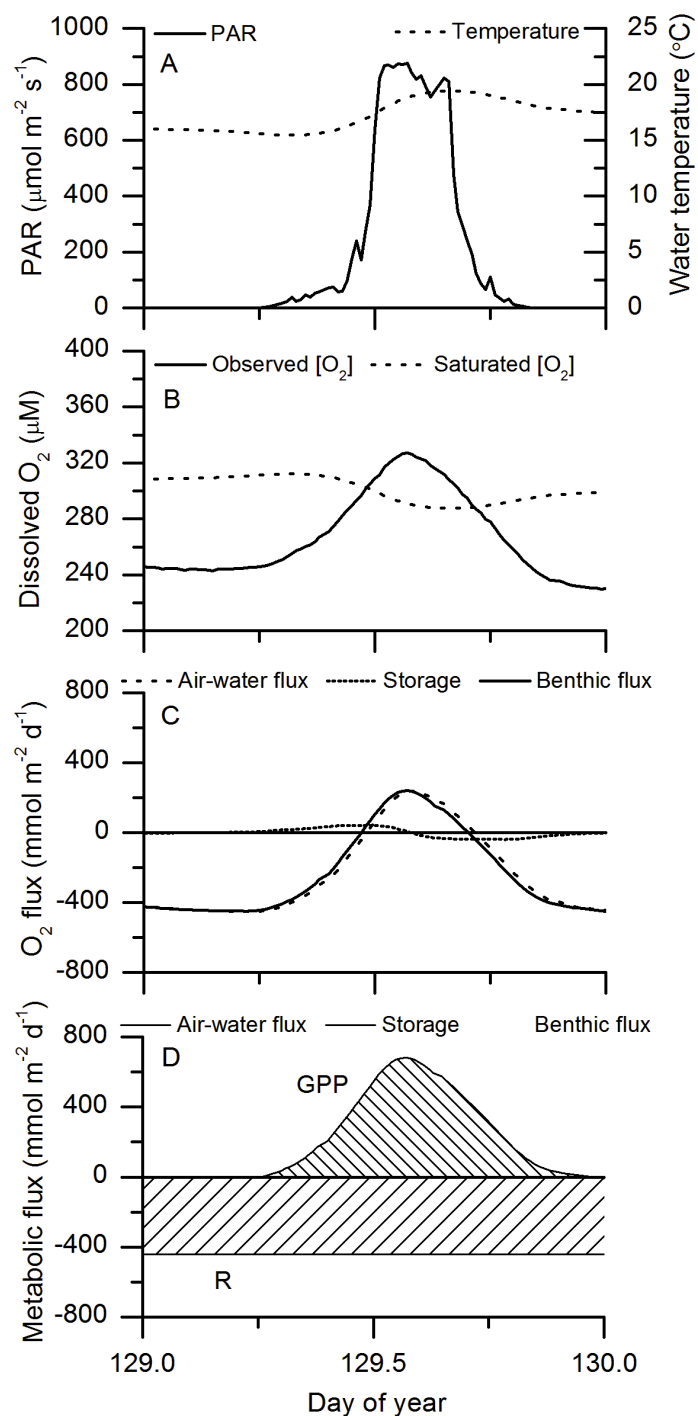


Figure 2. An example of diel change (in May of 2012) of **A** photosynthetically active radiation (PAR) and water temperature, **B** the concentration of dissolved oxygen in the stream and the predicted concentration at saturation, **C** the resulting oxygen flux, and **D** the metabolic fluxes of gross primary production (GPP) and respiration (R), represented by area.

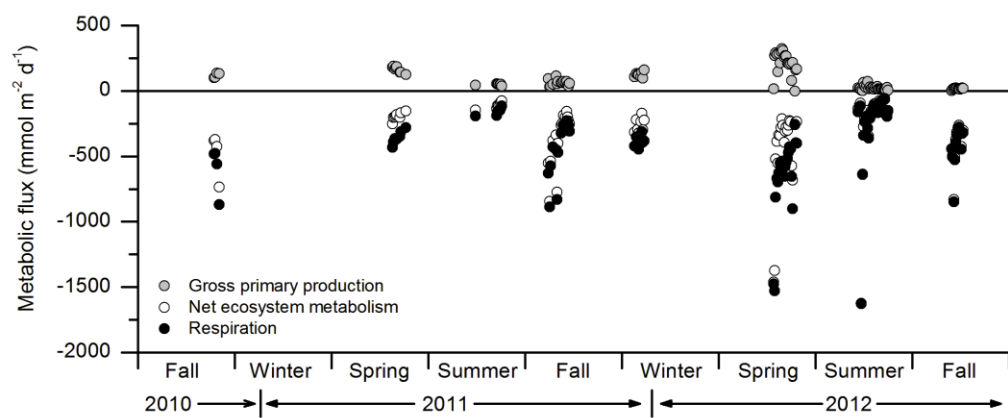


Figure 3. The diurnal metabolic flux presented by sample date. Rainstorms are responsible for the greatest rates of respiration.

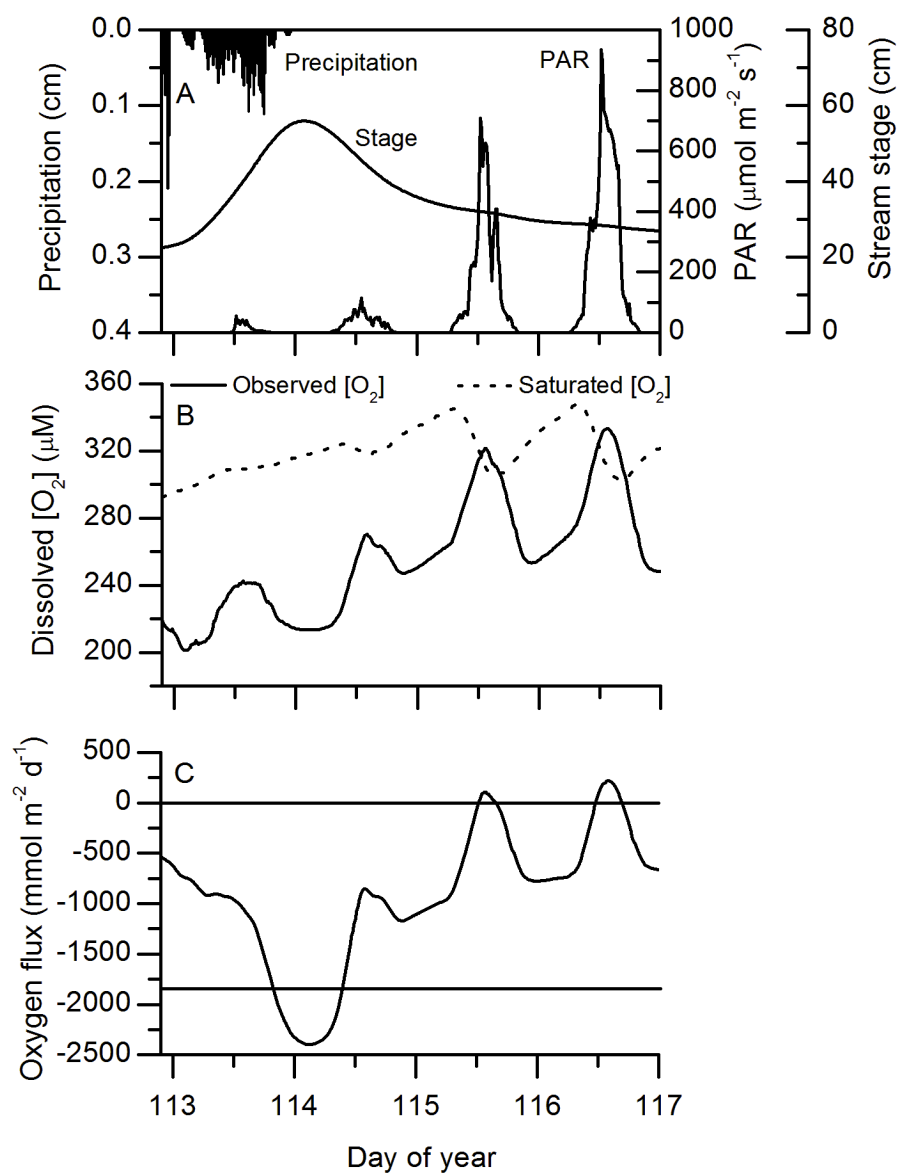


Figure 4. Over four days in April, 2012, the effect of a storm on **A** stream stage and PAR, **B** the observed oxygen concentration and the concentration at saturation, and **C** the resulting oxygen flux.



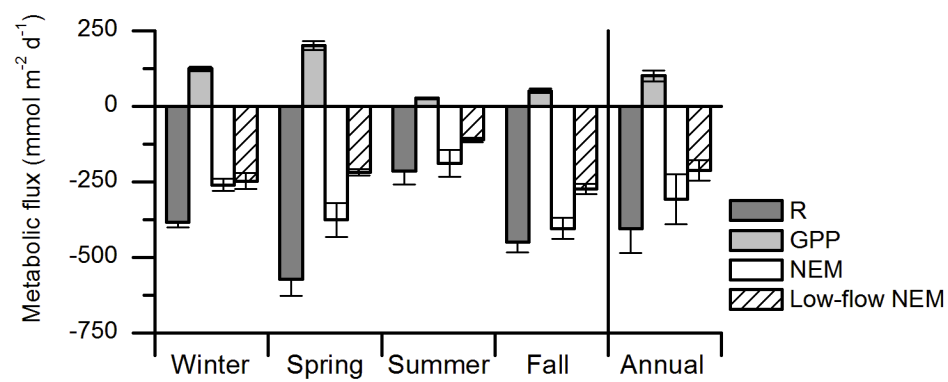


Figure 5. Average seasonal rates of respiration (R), gross primary production (GPP), net ecosystem metabolism (NEM) and NEM under low-flow (approximating base flow) conditions. Error bars represent standard error.

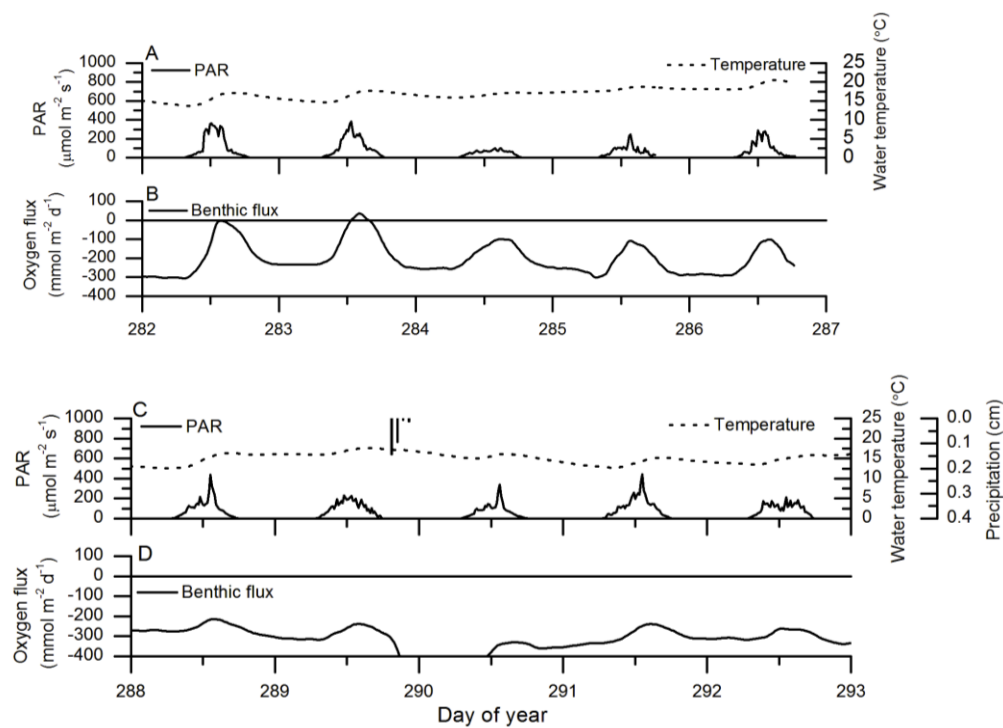


Figure 6. Five days of diurnal variation in PAR and water temperature **A** prior to the stage-shift in October of 2011, and **C** after the stage shift in October 2012. The resulting oxygen fluxes from the same time intervals **B** prior to the stage-shift and **D** after it. Note the minimal diurnal variation in oxygen flux in **D** with the exception of an increase in oxygen consumption on day 290 caused by precipitation.

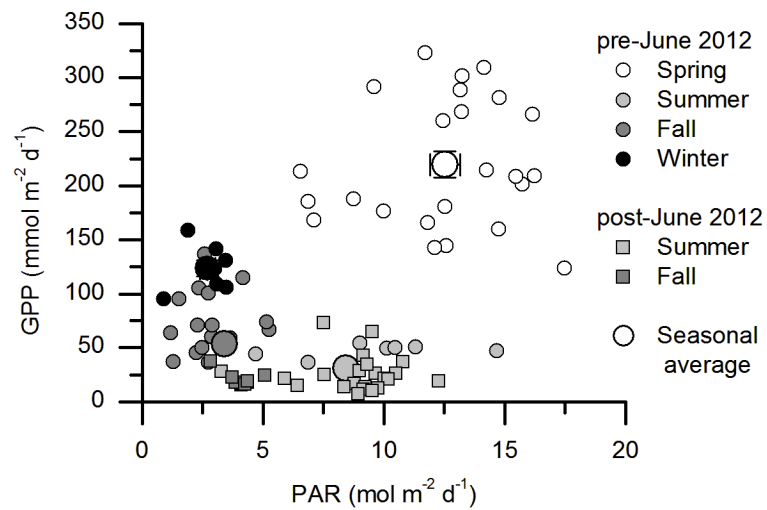


Figure 7. Seasonal gross primary production expressed as a function of photosynthetically active radiation (PAR) at the stream bed. Days with greater than 0.5 cm of rain were excluded. Larger symbols represent mean seasonal values. Error bars represent standard error. Error bars are smaller than symbol size in summer and fall.

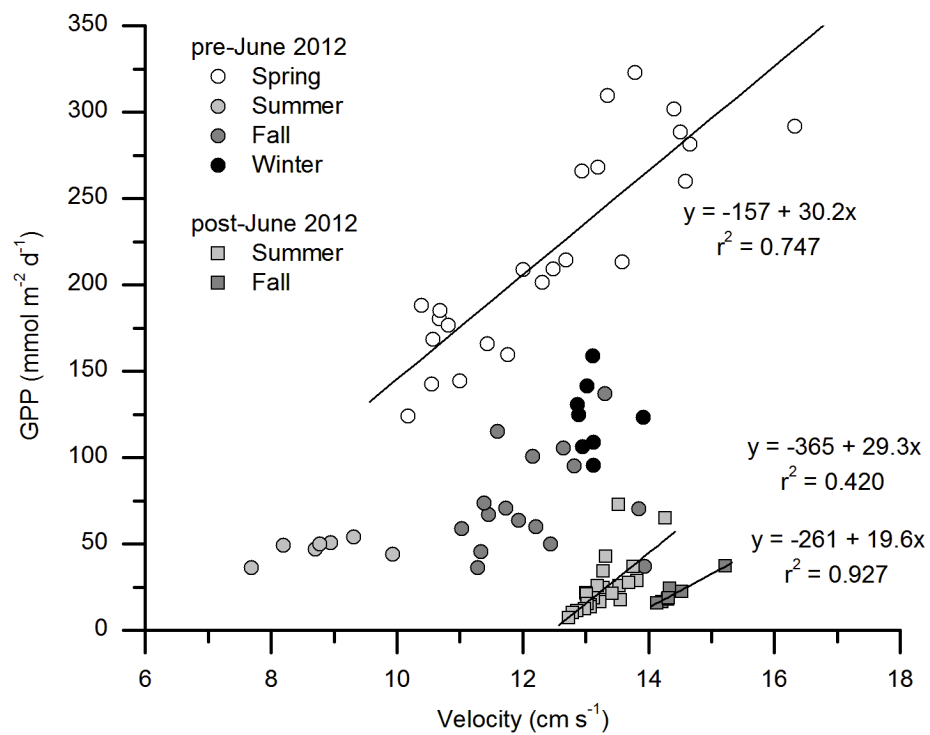


Figure 8. The relationship between gross primary production (GPP) and the mean stream velocity for non-storm conditions. Days with greater than 0.5 cm of rain were excluded. Symbols represent daily values and are separated by season and by their occurrence before and after the June 2012 stage shift.

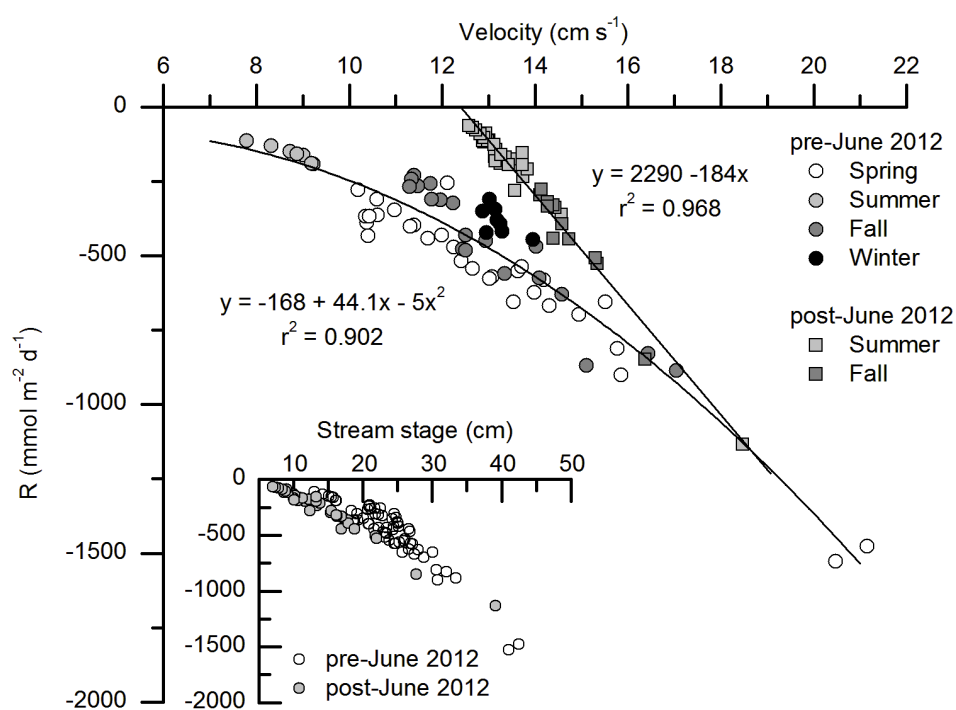


Figure 9. The relationship between the stream respiration rate ( $R$ ) and the mean stream velocity. Linear fits are to rates before and after the stage shift that occurred in June 2012. The inset displays  $R$  as a function of stream stage.



Figure 10. A stage shift occurred on June 2, 2012 caused by rainfall from a severe thunderstorm. In July of 2011 **A** flow was distributed across the stream channel (discharge =  $30 \text{ l s}^{-1}$ ). Following the stage shift in July of 2012 **B** a greater proportion of the flow was restricted to the thalweg (discharge =  $20 \text{ l s}^{-1}$ ).

## Chapter 4

### Spatial Variability in Oxygen Flux in a Coastal Stream: An Application of the Eddy Correlation Technique

Koopmans, D., and Berg, P.

Document prepared for submission to the journal Ecosystems

**Abstract**

This study applied the eddy correlation technique to examine in situ oxygen fluxes across the sediment-water interface at a site-specific scale at a riffle, pool, run (channelized flow), and freshwater tidal site in a sand-bedded coastal stream. The open water technique was applied simultaneously to determine oxygen fluxes over an integrated reach scale. The eddy correlation oxygen flux at the run site was the most similar to the reach scale with a relationship that was one-to-one. At the reach scale, however, the rate of oxygen consumption was greater both at night and during the day. This difference cannot be due to the gas transfer velocity, but instead reflects different metabolic processes in the sampling areas of the techniques. At the pool, riffle, and tidal sites nighttime oxygen consumption was one order of magnitude smaller than at the reach scale. The low rates of oxygen consumption may be explained by local suppression of hyporheic exchange. At the pool site the silt content would impede advection. Sediments at the riffle and tidal sites were medium-grained sands with a low silt content, but low rates of oxygen consumption there were consistent with pore water clogging by fine sediments and benthic algal exudates. Other factors, such as a site-specific limitation of bioavailable carbon, may contribute. The order of magnitude differences in oxygen flux are indicative of strong site-specific control of oxygen flux in this sand-bed stream ecosystem.



## **Introduction**

Complementary theoretical approaches to stream ecology are presented in the river continuum concept (Vannote et al., 1980) and the hierarchical classification of discrete fluvial habitats by Frissell et al. (1986). The river continuum concept predicts a continuum in the behavior of a fluvial ecosystem due to the gradient in physical conditions that occur with river order. The discrete classification of stream habitats, in contrast, provides a theoretical structure with which high spatial heterogeneity can be examined. The most commonly used approach for studying stream metabolism, the conventional open-water technique, is well suited to investigating changes in stream processes based on the larger continuum in physical gradients of which the stream is a part. Measurements of metabolism with the technique incorporate length scales of hundreds of meters or more. The technique has been routinely applied since it was presented by Odum (1956) yet predictive relationships between the drivers of metabolism and the stream ecosystem response are lacking. A partial explanation may be the high spatial and temporal heterogeneity of metabolic processes in stream ecosystems (e.g., Cooper et al., 1997; Reichert et al., 2009), in which reach-scale metabolism may be a function of dissimilar processes occurring in close proximity. For example, it may be that water velocity enhances respiration, yet the site-specific conditions which determine those rates include differences in grain size, water depth (as it relates to velocity), bedforms, vegetation, organic matter availability and other variables. In light of the site-specific complexity at which the drivers of stream ecosystem metabolism act, a site-

specific approach to the measurement of oxygen flux across the sediment-water interface may improve quantification of the drivers of stream metabolism.

A focal point of site-specific stream research has been hyporheic exchange. Hyporheic exchange can be defined as water which originates in the stream and enters interstitial spaces within sediment before returning to the stream. Respiration in shallow streams in unconsolidated sediments is driven by the interaction of overlying water and streambed sediment, where the greatest rates of bacterial activity occur (Fischer and Pusch, 2001). As stream water flows through permeable sediments it exposes benthic heterotrophic bacteria to oxygen, stimulating respiration. Stream water also carries suspended particulate and dissolved organic material which may serve as a fuel for respiration; particulates are selectively filtered out of the water column in flow over permeable sand beds (Huettel et al., 1996). As a result of these processes much of the mineralization of organic matter in streams with permeable beds may be attributed to hyporheic exchange (e.g., Grimm and Fisher, 1984; Fuss and Smock, 1996; Pusch and Schwoerbel, 1994).

The flux of oxygen across the sediment-water interface is studied as the inverse of carbon across the same because of the ease of detection of dissolved oxygen in aquatic environments. The assumption that the oxygen flux is the inverse of the carbon flux is subject to errors, however. Carbon mineralization in sediments occurs in the absence of oxygen by a cascade of terminal electron acceptors. Many of the reduced products of anaerobic respiration ( $\text{Mn}^{2+}$ ,  $\text{Fe}^{2+}$ ,  $\text{HS}^-$ ,  $\text{CH}_4$ ) accumulate in sediments at night and subsequently react with oxygen when it is produced at the sediment surface during the

day. As a result, oxygen fluxes across the sediment-water column interface may underestimate not only nighttime respiration but also daytime photosynthesis (Fenchel and Glud, 2000).

Hyporheic exchange encompasses a spectrum of flow interactions with the bed that includes the flow of stream water through alluvial aquifers adjacent to the stream (Wroblickey et al., 1998) or through exposed sand and gravel bars (Zarnetske et al., 2011). Numerical simulation of stream beds, however, indicates that hyporheic exchange in streams may be dominated by flow through small, centimeter-scale path lengths (Stonedahl et al. 2010; Kasahara and Wondzell, 2003) and it also includes a contribution from flow through infinitesimally short path lengths (Cardenas et al., 2008). Extrapolated to a natural stream bed this relationship predicts a wide range of hyporheic carbon mineralization rates along a stream reach that are dependent on changes in water velocity, grain size, and bedforms. In a natural stream the pool, riffle, run morphology creates variation in both water velocities and predominant grain sizes represented in sediments. The variation in hyporheic exchange across these environments has been investigated with benthic chambers (e.g. Pusch, 1996), pore water probes (e.g. Hendricks and White, 1991), and numerical modeling (Kasahara and Wondzell, 2003) confirming that hyporheic exchange induced by hydraulic pressure gradients across these features can be significant to ecosystem respiration.

The drivers of hyporheic exchange in stream ecosystems are well described from numerical simulation and flume studies. Hyporheic exchange scales with the square of water velocity and the square of sediment grain size (Packman and Salehin, 2003;

Packman et al., 2004). This scaling holds under a wide range of conditions, regardless of whether a streambed is flat, undulating, or rippled, and composed of fine sands or gravels. The mechanism is due to a combination of pore water advection and turbulent diffusion (Packman et al., 2004). Over flat, permeable surfaces the no-slip condition of zero velocity at the boundary may not hold, with the result that advection of stream water through pore spaces occurs. Additionally, hyporheic exchange can be induced across the boundary by a coupling of turbulence in the overlying water with pore water (Zhou and Mendoza, 1993; Packman and Salehin, 2003). Bedforms introduce an additional mechanism of pore water exchange; higher pressures on the upstream side of a bedform relative to low pressures caused by flow separation on the downstream side will induce a Darcy flow of pore water through the bedform (Huettel et al., 1997), although non-Darcy flow also contributes (Elliott and Brooks, 1997; Packman et al., 2004).

Complicating prediction of hyporheic exchange in natural systems is attenuation by pore water clogging and groundwater discharge. Benthic algal mats suppress hyporheic exchange both by their patterns of growth across the sediment surface and with extracellular exudates (Battin and Sengschmitt, 1999; Larned et al., 2013). Additionally, as with conventional biocatalytic sand filters, excess suspended organic matter can also contribute to sediment clogging (Huettel, 1996). Barring complications of sediment clogging, however, the greatest rates of oxygen flux would be expected where small scale features are present and exposed to higher water velocities, as in a rippled bed (Worman et al., 2007; Stonedahl et al., 2010). Groundwater can cause the diversion of hyporheic flowpaths and a reduction in the area through which hyporheic exchange occurs

(Wroblickey et al., 1998; Boano et al., 2009). This reduction in hyporheic area, however, may be offset by increase in the rate of hyporheic exchange through the remaining, shorter, flow paths (Cardenas and Wilson, 2006). Permeable surface sediments can also be clogged by fine particles which attenuate hyporheic flow (Schalchli 1992; Battin and Sengshmitt, 1999; Rosenberry and Healy, 2012).

In this study we introduce a novel technique to the study of site-specific metabolic processes in a stream ecosystem, eddy correlation. The eddy correlation technique is the standard for calculating land-atmosphere and sea-atmosphere fluxes of mass, momentum, and energy (e.g., Baldocchi, 2003), and has been adapted to underwater applications to measure oxygen flux across the sediment-water interface in aquatic systems (Berg et al., 2003). The technique has also been used to determine salt and heat fluxes across the sediment-water interface in aquatic systems (Crusius et al., 2008). Turbulence is the mechanism responsible for the vertical transport of mass, momentum, and energy in rivers and streams. The eddy correlation technique takes advantage of this property to quantify the flux of oxygen with the high frequency measurement of both the tracer concentration and the vertical velocity at a point in the water column. No water-atmosphere oxygen exchange coefficient is needed for the eddy correlation technique, making this method the closest we can come today to measuring oxygen flux across the sediment-water interface *in situ*.

The design of this study was to investigate the drivers of hyporheic oxygen flux at a spatial scale at which site-specific responses were expected due to differences in sediment type, bedforms, and water velocities. Because bedforms and water velocities

interact to generate hyporheic exchange (Huettel et al., 1996; Stonedahl et al., 2012) riffles, with higher water velocities and rippled beds, are sites where greater hyporheic exchange may occur and greater oxygen consumption would be expected. Using buried flow-through chambers Pusch (1996) determined that respiration rates in the riffle of a mountain stream were twice as great as respiration rates in a neighboring pool. The eddy correlation technique was applied to examine oxygen flux at a run, riffle, and pool of a coastal stream. Simultaneous measurements of oxygen flux were made with the open water technique to identify differences in oxygen flux at a greater spatial scale. In addition a freshwater tidal portion of the stream was included as a study site to examine the effect of a wide and reproducible range of water velocities on oxygen flux in a natural system over a short period of time.

### *Study Site*

The study site was Rattrap Branch on the eastern shore of Virginia, 5 km southeast of the town of Onley. The stream is contained within the Virginia Coast Reserve Long Term Ecological Research site. The watershed is split between agriculture (38%) and forest (41%) with the remainder primarily in low-density residential use (Luckenbach et al. 2008). The stream has a sand-bed and a base flow discharge of  $40 \text{ l s}^{-1}$ . At baseflow conditions the width of Rattrap Branch varied from 1 to 3 m along the study reach, with stream depth in the thalweg typically 15 cm, but up to 1 m in pools.

The pool, riffle, and run locations selected for the eddy correlation deployments were within 150 m of a forested portion of the stream reach (Figure 1). A farm road

passed over the creek just upstream of the pool site, but the studied portion was beneath the forest canopy. The dissolved oxygen concentration, required for calculating the oxygen flux by the open water technique, was determined just upstream of the riffle site. At the downstream end of Rattrap Branch the stream flows into a tidally-filled freshwater basin before entering the downstream salt marsh. The tidal basin served as the location for additional eddy correlation measurement of the oxygen flux across the sediment-water interface.

## **Methods**

### *Data Collection*

Oxygen flux measurements were conducted at the run site in the fall of 2010 and the spring of 2011. Between sampling in the spring of 2011 and the summer of 2011 the migration of a submerged sandbar into the run site caused us to cease measurements of fluxes at that location. Oxygen flux measurements were conducted at the pool and riffle sites in the spring and fall of 2012. During all sampling events at the pool, riffle, and run sites measurements for the determination of oxygen flux by the open water technique were collected continuously while measurements for the determination of eddy correlation oxygen fluxes were made at a rate of a few hours per day due to interruptions caused by particle-induced fouling of the oxygen microelectrodes. Oxygen flux at the tidal site was determined using the eddy correlation technique in the fall of 2012.

*Physical and Chemical Characteristics*

The proximal drivers of metabolism were determined over two different spatial scales to accommodate the two different oxygen flux techniques being applied; average conditions were determined over a 100 m study reach (reach scale) for the open water technique while point measurements were made for the eddy correlation technique. The proximal drivers were PAR at the streambed, water velocity, and water temperature. The mean water velocity at the scale of the study reach was determined experimentally and then extrapolated as a linear function of stream stage across observations. Changes in stream water depth over time were calculated by subtracting atmospheric pressure recorded at a local airport (4 km distant) from ambient pressure recorded at the bed of the stream by a water level logger (Onset Computers, Onset MA). Stream stage was determined with a staff gauge that had been driven into streambed sediments. Stream depth data were benchmarked to stage height to ensure accurate relative measures of stream stage across sampling periods. Water velocities were determined from the transport time for a peak in conductivity associated with the addition of saline water. Water velocity measurements at the point scale, for the eddy correlation technique, were determined from the mean velocities recorded by the ADV. While the measuring heights applied in this study varied from 5 to 12 cm, and were not aligned with the ideal 4/10ths height at which the mean water column velocity would be expected (USGS, ), the recorded velocities were indicative of the mean water column velocities at each site.

Photosynthetically Active Radiation (PAR) at the stream bed was determined with HOBO Pendant Temperature/Light submersible data loggers and Odyssey PAR



recorders, both of which were calibrated to PAR at the streambed with a LI-COR LI 193 Underwater Spherical Quantum Sensor (Long et al., 2012). Six light loggers were deployed with a spacing of 15 m between each one along the 100 m study reach. Additional HOBO loggers were placed on either side of the eddy correlation footprint or just downstream of the eddy correlation instruments.

Additional measurements were made of sediment and water column characteristics. Triplicate samples for particle size distribution and organic matter content analysis were collected from the top seven centimeters of sediment at the riffle, pool, and run, and tidal site as well as other representative, sand-bedded locations within the study reach. The organic matter content of dried sediments was determined by a change in mass with combustion at 500°C for 4 hours. Following organic matter removal sediments were dis-aggregated with a mortar and pestle before the particle size distribution was analyzed on a Beckman Coulter LS 13 320 laser diffraction particle size analyzer. The sediment hydraulic conductivity was determined at the run, riffle, and tidal sites by transferring the upper 10 cm of sediments to a permeameter and quantifying the rate of water flow through the sands under constant head pressure (e.g., Landon et al., 2001). The grain size at the pool site was too fine for a permeameter application, so the hydraulic conductivity was estimated based on the representative particle sizes from published values (Hornberger et al., 1998). The concentration of active chlorophyll *a* in the top centimeter of surface sediment was determined by suspending the pigments in a methanol/acetone solution and determining the difference in the absorbance at 665 and 750 nm before and

after acidification, to discriminate it from phaeopigment (Lorenzen 1967; with calibration by Pinkney and Zingmark 1994).

### *Oxygen Flux*

To determine the oxygen flux with the open water technique a 1D vertical oxygen mass balance across the air-water and sediment-water interfaces was developed as

$$j_{air} + h \frac{\Delta C}{\Delta t} - j_{benthic} = 0 \quad (1)$$

where  $j_{air}$  is the oxygen flux across the air-water interface,  $h$  is the water depth,  $C$  is the concentration of oxygen,  $t$  is time and  $j_{benthic}$  is the oxygen flux across the sediment-water interface. The flux across the air-water interface was defined as the product of the gas transfer velocity ( $k$ ) and the difference between the dissolved oxygen concentration at saturation (accounting for temperature and pressure) and the observed oxygen concentration. The gas transfer velocity was determined by the loss of an introduced propane gas tracer relative to the loss of a salt tracer along a 100 m study reach (Wanninkhof et al., 1990; Marzolf et al., 1994; Young and Huryn 1998). This determination was made eleven times under varying flow conditions. These gas transfer velocities were fit to stream stage before and after a stage shift occurred ( $n = 7$ ,  $r^2 = 0.870$ ; and  $n = 4$ ,  $r^2 = 0.784$ ). These linear fits were used to predict the gas transfer

velocity across the range of observed stream stages. Further details on the calculation of open water fluxes may be found in Koopmans and Berg, (in prep).

The eddy correlation technique was used to determine oxygen flux in Rattrap Branch at site-specific scales of a riffle, pool, and run. The eddy correlation technique relies on the measurement of the vertical water velocity and the dissolved oxygen concentration in the same measurement volume. A Nortek Vector acoustic Doppler velocimeter (ADV) was attached to a three-legged stainless steel frame which was placed in the stream. A fast-responding oxygen microsensor made by Unisense (Ox-Eddy; Revsbech, 1989) was mounted directly to a submersible amplifier and also attached to the frame. The tip of the microsensor was aligned 5 mm upstream or downstream of the center of the measuring volume of the ADV to simultaneously determine the oxygen concentration ( $C$ ) in the same volume. The height of the ADV was adjusted so that the measuring volume ranged from 5 cm to 12 cm above the sediment surface. The geometry of the ADV instrument places the center of the measurement volume 15.7 cm from the transmit source. As a result, the vertical deployments of the ADV were restricted to water depths of ~20 cm or greater. Water depths in the riffle of the creek were frequently shallower than this and on those occasions the ADV was attached to the frame lying on its side at the stream bed (Fig. 2E).

The microelectrode was powered by an attached, submersible picoamplifier which continuously logged the microelectrode output to the ADV (see Berg et al., 2003 for more details). The ADV recorded observations of velocity and input from the picoamplifier at 64 Hz. These high frequency observations were averaged down to 16 Hz

for data processing. The velocity field was rotated so that the mean current was in the x-direction and mean velocities were zero in both the transverse (y) and vertical (z) axes. The fluctuating components of vertical velocity ( $u_z'$ ) and oxygen ( $C'$ ) were isolated from their mean values by a Reynolds decomposition, with the mean values determined with a least-square linear fitting to the observations in 14.5 minute increments. The benthic oxygen flux was calculated as the mean of the product of the fluctuating components ( $\overline{u_z' C'}$ ).

Oxygen measurements made with the microelectrode were calibrated in oxygen-depleted and oxygen-saturated water prior to deployment. This calibration was also used to verify that the 90% response time of the microelectrode was 0.4 s or faster. The eddy correlation system was deployed with a PME miniDOT optical oxygen sensor mounted to the frame at the same height as the measurement volume which was used to identify and correct for drift in microelectrode measurement of oxygen concentration. Microelectrode applications in streams and rivers with high water velocities and high concentrations of suspended sediments and debris can be impeded by microelectrode fouling and breakage. The success rate for reliable, high frequency oxygen determination in stream water improved with the development by Unisense of a thicker-tipped, 100  $\mu\text{M}$ , Ox-Eddy microelectrode.

### *Technique Footprints*

To compare the oxygen flux techniques the footprint of each technique, defined as the minimum area that contributes 90% of the flux, was determined. The footprint of the open water technique has been described as a function of the mean stream velocity ( $U$ ) and the reaeration coefficient ( $K$ ; which is the gas transfer velocity divided by stream depth) as equal to  $3u/K$  (Chapra and di Toro, 1991). To our knowledge the derivation of this equation and the conditions under which it can be applied have not been made clear in the literature, however. To independently quantify the length of the open water footprint a two-dimensional mass balance for oxygen concentration was solved as

$$C_i u w h + k_{O_2} \left( DO_{sat.} - \frac{C_i + C_{i+1}}{2} \right) l w - C_{i+1} u w h - j_{benthic} l w = 0 \quad (2)$$

where  $C_i$  and  $C_{i+1}$  are the oxygen concentrations at the upstream and downstream ends of the study reach, respectively,  $w$  is the stream width,  $h$  is the stream depth,  $k_{O_2}$  is the oxygen gas transfer coefficient,  $DO_{sat.}$  is the saturating concentration of oxygen in the stream and  $l$  is the stream length. The solution was determined iteratively, where the output oxygen concentration over a short stream cell (1 m) was applied as the input oxygen concentration to the next, downstream, cell.

The footprint of the eddy correlation technique is a function of the measurement height, the water depth, the surface roughness, and at shallow water depths also of the gas transfer velocity also has an effect (Berg et al., 2007). Below depths at which  $h < 6.7z$ , where  $h$  is the water depth and  $z$  is the measuring height, the footprint is less well

defined. The water depth in Rattrap Branch was shallow enough that many of the eddy correlation deployments fell in this category. Accordingly, the flux footprint was calculated without incorporating the water depth-dependent factor, giving a first order estimate of the footprint length. A mean surface roughness was determined across all sites from the Reynolds stress which was calculated from velocity observations as described by Berg et al., (2007).

## **Results**

### *Physical and Chemical Characteristics*

The pool, run, and riffle sites were located within 150 m of each other, yet the differences in physical characteristics between the sites were substantial. The pool site was unvegetated with fine organic-rich sediment forming a generally smooth bed (Figure 2, A and B). The run site was most representative of the stream reach as a whole, with an irregular, undulating bed that supported dense plant (*Vallisneria sp.*) and algal abundance in the spring and summer (Figure 2B). In the fall and winter algal abundance diminished at the site and throughout the reach. The bed of the riffle site supported sparse plant and algal growth in the spring of 2012, but these were removed from this site by storm-induced scouring in the summer of 2012. Ripples were consistently present at the site, however. At the tidal site no plants were supported at the bed, but benthic algae were present. The bed geometry was generally smooth with undulations, but without characteristic ripples. The sediment surface was unbroken by other roughness elements.

The median particle size at all sites was a medium sand, although the pool site had a larger proportion of silt at 25% than the run, riffle, and tidal sites with 0.42%, 1.3%, and 3.0% silt, respectively. The range of grain diameters at the 10<sup>th</sup>, 50<sup>th</sup> and 90<sup>th</sup> largest percentiles reflected the greater fine sediment content at the pool, and the greater coarse sediment content at the run (Figure 3). The average diameter of the 84<sup>th</sup> largest percentile ( $D_{84}$ ) can be useful in characterizing hydrodynamic conditions at the streambed. At the pool, run, riffle, and tidal sites  $D_{84}$  was 450  $\mu\text{m}$ , 787  $\mu\text{m}$ , 542  $\mu\text{m}$ , and 494  $\mu\text{m}$ , respectively. The organic matter content at the same sites was 33%, 0.3%, 0.5%, and 0.8%. The sediment hydraulic conductivity at the pool site was estimated to be  $5 \times 10^{-6} \text{ m s}^{-1}$ , while the hydraulic conductivities at the riffle, run, and tidal sites were measured as  $1.1 \times 10^{-4} \text{ m s}^{-1}$ ,  $4.9 \times 10^{-5} \text{ m s}^{-1}$ , and  $4.4 \times 10^{-5} \text{ m s}^{-1}$ . The concentration of chlorophyll *a* at the pool, run, and riffle sites was  $28.7 \pm 0.9 \text{ mg m}^{-2}$  (mean  $\pm$  s.e.),  $40.8 \pm 5.3 \text{ mg m}^{-2}$ , and  $47.6 \pm 5.6 \text{ mg m}^{-2}$ , respectively (throughout this manuscript errors are reported as the standard error). The concentration of chlorophyll *a* in surficial sediments at the tidal site was substantially higher with a mean of  $104 \pm 34 \text{ mg m}^{-2}$  in the stream center where benthic algal abundance was minimal, and a mean of  $298 \pm 20 \text{ mg m}^{-2}$  to the side, where benthic algal abundance was greater.

### *Spatial Scale of Measurement*

For the open water technique, under conditions that were typical of the fall of 2012 (a water depth of 10 cm, a gas transfer velocity of  $5.8 \text{ m d}^{-1}$ , and a stream velocity of  $0.14 \text{ m s}^{-1}$ ) 90% of the equilibrium oxygen flux was observed at 480 m downstream

from the sediment flux transition (Figure 4). Projected upstream from the point of measurement the footprint would have extended through the pool site and an additional 300 meters into the forested buffer upstream of the farm road at the northern end of study reach (Figure 1). The length of the footprint increases exponentially with decreases in the gas transfer velocity and increases proportionately with increases in the water velocity and water depth (Figure 5). As a result the footprint would have been substantially longer in the summer, 1090 m (assuming a gas transfer velocity of  $2.1 \text{ m d}^{-1}$ , a water velocity of  $13 \text{ cm s}^{-1}$ , and a water depth of 0.9 m). These model results are directly proportional to  $3u/K$  (Chapra and DiToro, 1991) but are smaller, corresponding to  $2.3 u/K$ .

The bed roughness and measuring height determine the length of the eddy correlation footprint, with a contribution due to the shallow water depth in this stream. The mean bed roughness determined from the roughness Reynolds number was 0.01 m and the mean measuring height was 0.07 m. Without inclusion of a depth correction described by the Berg et al., (2007) model, the length and width of the eddy correlation footprint were 5 m and 0.45 m, respectively. The true length of the eddy correlation footprint would have been greater than this, but that length is poorly defined in these very shallow waters.

#### *Comparison of Reach and Site Scales*

A total of 76 hours of high quality oxygen fluxes were determined at the pool, run, and riffle sites, with 6.8 additional hours determined at the tidal site (Figure 6).



Because the tidal fluxes were not accompanied by open water flux measurements, those analyses are presented separately. The observations at the pool, run, and riffle sites were binned into 48 observations with a mean duration of 95 minutes. The relationship between reach-scale, open water fluxes and site-specific, eddy correlation fluxes depended on the eddy correlation measurement location. Of the pool, run, and riffle sites the pool site fell furthest from a 1:1 correspondence with fluxes at the reach scale ( $y = -28.8 + 0.0678x$ ,  $n = 27$ ,  $r^2 = 0.299$ ,  $p = 0.0031$ ; Figure 6). The change in oxygen flux at the riffle site were also small and positively correlated with a change at the reach scale ( $y = 93.6 + 0.325x$ ,  $n = 10$ ,  $r^2 = 0.823$ ,  $p = 0.00029$ ). The change in oxygen flux at the run site was more similar to the change in oxygen flux at the reach scale, with a relationship that was close to 1:1 but with an offset towards greater oxygen production in the run ( $y = 185 + 0.958x$ ,  $n = 10$ ,  $r^2 = 0.859$ ,  $p = 0.00013$ ).

While the aggregate analysis provides a perspective on the relationship between reach-scale and site-specific oxygen fluxes, these measurements were taken across seasons with respective changes in the processes driving oxygen flux. A time-series comparison of the techniques controls for their temporal differences. One-and-a-half days of reach-scale and patch-scale fluxes at each site are given in Figure 7. Although oxygen fluxes from the spring are presented for all three sites the fluxes at the run were determined in the spring of 2011 while fluxes at the pool and riffle were determined three days apart in the spring of 2012. The oxygen fluxes at the pool and riffle sites were both one order of magnitude smaller than the oxygen fluxes determined at the reach scale. That difference in magnitude persisted during nighttime and daytime (the daytime data

from the riffle site include four hours after dawn). The average nighttime rate of oxygen flux in the pool was  $-27.4 \pm 1.2 \text{ mmol m}^{-2} \text{ d}^{-1}$  between day 124.8 and 125.3, while the open water flux for the same time interval was  $-540 \pm 9 \text{ mmol m}^{-2} \text{ d}^{-1}$  (all measurement errors presented here are standard errors). Similarly, at the riffle site the average nighttime oxygen flux was  $-24.9 \pm 0.75 \text{ mmol m}^{-2} \text{ d}^{-1}$  between day 121.8 and 122.3, while the open water flux for the same time interval was  $-506 \pm 12 \text{ mmol m}^{-2} \text{ d}^{-1}$ .

Oxygen fluxes at the run, however, were comparable in magnitude to the reach scale. At night oxygen fluxes at the site were smaller than at the reach scale with a mean of  $-127 \pm 5 \text{ mmol m}^{-2} \text{ d}^{-1}$  between day 131.75 and 132.25 and  $-237 \pm 11 \text{ mmol m}^{-2} \text{ d}^{-1}$  at the reach scale. During the day oxygen fluxes at the site exceeded those at the reach scale with a mean of  $408 \pm 24 \text{ mmol m}^{-2} \text{ d}^{-1}$  between day 132.49 and 132.65 and  $90 \pm 7 \text{ mmol m}^{-2} \text{ d}^{-1}$  at the reach scale. The net effect of these differences was as observed above, that the oxygen fluxes at the run were more positive than those at the reach scale, but the difference was greater during the middle of the day than at night.

#### *Site Specific Differences in Oxygen Flux*

Velocity is a driver of hyporheic exchange, so to control for differences in velocity across sites nighttime oxygen fluxes were also expressed as a function of stream velocity. Increases in water velocity were correlated with an increase in magnitude of nighttime oxygen flux at the pool, run, riffle, and tidal sites and also in the simultaneous measurements at the reach scale (Figure 8,  $p < 0.05$  in all cases). The water velocities at the site scale were determined by the ADV while the water velocities at the reach scale

were determined from the relationship between stream stage and tracer transport time. Across all nighttime observations the mean velocity at the pool site was  $7.1 \pm 0.7 \text{ cm s}^{-1}$  and the associated oxygen flux was  $-68.1 \pm 8.7 \text{ mmol m}^{-2} \text{ d}^{-1}$ . The water velocity and oxygen flux at the reach scale for the same time intervals were  $14.7 \pm 0.4 \text{ cm s}^{-1}$  and  $-550 \pm 59 \text{ mmol m}^{-2} \text{ d}^{-1}$ , or eight times the oxygen fluxes at the pool (Figure 8A;  $n = 14$ , 29.8 hrs). The mean water velocity at the run site was  $12.3 \pm 1.2 \text{ cm s}^{-1}$  with an associated oxygen flux of  $-206 \pm 46 \text{ mmol m}^{-2} \text{ d}^{-1}$ . The water velocity and oxygen flux for the reach scale at the same time were  $12.4 \pm 0.9 \text{ cm s}^{-1}$  and  $-417 \pm 66 \text{ mmol m}^{-2} \text{ d}^{-1}$ , or twice the nighttime oxygen flux at the run (Figure 8B;  $n = 6$ , total of 9.8 hours). At the riffle site the oxygen flux was statistically similar to the pool over much of the range, but at greater velocities. At water velocities between 12 and 17  $\text{cm s}^{-1}$ , with a mean of  $15.3 \pm 0.6 \text{ cm s}^{-1}$ , the mean oxygen flux was  $-44.6 \pm 10.7 \text{ mmol m}^{-2} \text{ d}^{-1}$ . Across the same range the mean water velocity at the reach scale was  $14.4 \pm 0.4 \text{ cm s}^{-1}$  with an associated oxygen flux of  $-537 \pm 53 \text{ mmol m}^{-2} \text{ d}^{-1}$  (Figure 8C;  $n = 6$ , total of 18.3 hours). An additional measurement of oxygen flux was conducted at the riffle site during a storm induced peak in stream stage. At a water velocity of  $22.3 \text{ cm s}^{-1}$  the mean oxygen flux at the site was  $-398 \pm 10.6 \text{ mmol m}^{-2} \text{ d}^{-1}$ , ten times the rate observed at a velocity of  $15 \text{ cm s}^{-1}$  at the same site. At the same time interval the reach scale water velocity was  $18.9 \text{ cm s}^{-1}$  with a mean oxygen flux of  $-1300 \text{ mmol m}^{-2} \text{ d}^{-1}$  (total 35 minutes).

Oxygen fluxes were determined at the tidal site under a wide range of water velocities (0.9 to  $18.1 \text{ cm s}^{-1}$ ). The mean daytime oxygen flux,  $26 \pm 3.4 \text{ mmol m}^{-2} \text{ d}^{-1}$  ( $n = 23$ , total of 3.5 hours), was similar to daytime fluxes at the pool and riffle sites. Oxygen

flux during the day did not show a clear relationship with velocity, perhaps due to mixed effects of the stimulation of both photosynthesis and respiration by increases in velocity (e.g. Hume et al., 2010). There was a correlation, however, between oxygen flux and water velocity at night (Figure 8D). The mean nighttime oxygen flux at the tidal site,  $-11.2 \pm 1.7 \text{ mmol m}^{-2} \text{ d}^{-1}$  ( $n = 20$ , total of 3.2 hours), was smaller than the oxygen flux observed at any of the other sites. Over the nighttime range of water velocities, from  $1.2 \text{ cm s}^{-1}$  to  $18.1 \text{ cm s}^{-1}$ , the magnitude of the oxygen flux increased from  $-4.2 \text{ mmol m}^{-2} \text{ d}^{-1}$  to  $-27 \text{ mmol m}^{-2} \text{ d}^{-1}$  ( $r^2 = 0.616$ ,  $p < 0.0001$ ).

#### *Confirmation of Hyporheic Oxygen Consumption*

The rapid changes in water velocity at the tidal site allowed for an independent calculation of the sediment-water oxygen flux and evidence for the contribution of hyporheic exchange to oxygen consumption. A miniDOT optode was buried just beneath the sediment surface (center of membrane at 1 cm depth) at the tidal site, aligned perpendicular to the predominant flow direction to minimize its resistance to flow. At high tide, when overlying water was stagnant, the pore water at this depth was anoxic. As the tide dropped water velocities increased. When the water velocity reached  $20 \text{ cm s}^{-1}$ , near the peak velocity of  $24 \text{ cm s}^{-1}$ , the velocity was great enough to generate hyporheic exchange at the depth of the buried optode, the oxygen concentration increased to 160 mM (Figure 9). Hyporheic exchange continued to deliver oxygen to these pore spaces as stream water flowed at this peak rate over the sediment surface. On the rising tide, however, the water velocity decreased below  $20 \text{ cm s}^{-1}$ , hyporheic exchange stopped and

the residual oxygen in pore water was consumed at a linear rate. Integrating the rate of oxygen consumption ( $60 \text{ mM h}^{-1}$ ) to a depth of 1 cm gives an oxygen flux of  $-14 \text{ mmol m}^{-2} \text{ d}^{-1}$ . At the water velocity that initiated this depth of hyporheic exchange,  $20 \text{ cm s}^{-1}$ , the observed relationship between water velocity and oxygen flux at the site (Figure 8D) would predict twice the oxygen flux,  $-27 \text{ mmol m}^{-2} \text{ d}^{-1}$ .

### *Elevated Daytime Respiration*

The high temporal and spatial resolution of the eddy correlation technique was also valuable in describing site-specific responses to sunlight. In the spring of 2012 the stream bed at the pool site was only exposed to direct sunlight for two hours at midday when the angle of the sun was great enough to shine through a break in the canopy directly over the stream. During the night of May 3<sup>rd</sup> and the early morning of May 4<sup>th</sup> the mean rate of oxygen flux was  $27.4 \pm 1.2 \text{ mmol m}^{-2} \text{ d}^{-1}$  (Figure 10). The midday peak in solar irradiance co-occurred with a peak in oxygen production between 12:15 and 12:30. With increased shading the oxygen fluxes rapidly shifted from net production to net consumption of oxygen, with a maximum rate of consumption between 14:30 and 14:45. The mean rate of oxygen flux during the period of indirect sunlight in the afternoon (between 13:45 and 16:00) was  $-50.1 \pm 4.2 \text{ mmol m}^{-2} \text{ d}^{-1}$ , 1.8 times the rate of oxygen flux during the previous night. After sundown on May 4 the magnitude of the rate of oxygen flux diminished to  $-26.2 \pm 2.2 \text{ mmol m}^{-2} \text{ d}^{-1}$ , an indistinguishable rate from the previous night.

## Discussion

### *Suitability for Hyporheic Exchange*

The physical characteristics of Rattrap Branch sediments at the run, riffle, and tidal sites are consistent with those in which hyporheic exchange occurs. The dominant sediment grain size at all sites was medium-grained sand, however the high proportion of silt by volume at the pool site (25%) would be expected to impede pore water advection. The hydraulic conductivity at the run, riffle, and tidal sites ( $1.1 \times 10^{-4} \text{ m s}^{-1}$ ,  $4.9 \times 10^{-5} \text{ m s}^{-1}$ , and  $4.4 \times 10^{-5} \text{ m s}^{-1}$ , respectively) was consistent with hydraulic conductivities at which extensive hyporheic exchange occurs. By examining tracer breakthrough curves in shallow wells in the beds headwater streams Morrice et al., (1997) found a high degree of connectivity between pore water and overlying stream water in a mountain headwater stream with a sediment hydraulic conductivity of  $4 \times 10^{-5} \text{ m s}^{-1}$ . Additionally, at a permeability of  $2.9 \times 10^{-11} \text{ m}^2$  (equivalent to a hydraulic conductivity of  $2.9 \times 10^{-4} \text{ m s}^{-1}$  at 20 °C) Huettel et al., (1996) observed the advection of overlying water to a depth of 4.5 cm in pore spaces in sands over 16.5 hours. The hydraulic conductivities determined for Rattrap Branch sediments do not rule out accrual of fine sediments in hyporheic flow paths resulting in clogging, however (e.g. Schalchli 1992). Hydraulic conductivities were determined by the transfer of sand from the stream bed into a permeameter, as a result the re-sorting of sediments would have opened hyporheic flowpaths in which organic matter had accumulated.

Based on observations of velocity-driven penetration of oxygen into pore waters at the tidal site there is evidence that hyporheic exchange occurs at this site (Figure 9).

Further, the rate of oxygen flux across the sediment-water interface determined from the rate of change of pore water oxygen concentration to a depth of 1 cm ( $-14 \text{ mmol m}^{-2} \text{ d}^{-1}$ ) was similar to the corresponding rate of oxygen flux ( $-27 \text{ mmol m}^{-2} \text{ d}^{-1}$ ) calculated using the eddy correlation technique at a comparable velocity ( $20 \text{ cm s}^{-1}$ ). The similarity in these rates indicates that oxygen flux in this system is driven in part by hyporheic exchange. The proximity and similar sediment grain sizes and hydraulic conductivities to the run and riffle sites suggest that oxygen consumption at those sites is also driven, in part, by hyporheic exchange.

#### *Comparison of Reach and Site Scales*

Because of the different footprints of the two techniques direct comparisons between sediment-water oxygen fluxes measured by each one are difficult to make. The modeled size of the open water footprint is large enough that processes occurring at the scale of pools, runs, and riffles would not be resolved with the technique. Based on model prediction, the footprint of the open water technique was 480 m long under common conditions in which oxygen flux was determined in the fall and spring ( $k = 5.8 \text{ m d}^{-1}$ ,  $u = 0.14 \text{ m s}^{-1}$ , depth = 0.1 m) and the footprint length would increase with decreases in stream stage and the gas transfer velocity in summer (Figure 5). The predictions of the footprint length were a factor of  $2.3u/k$  instead of those predicted by  $3u/k$  (Chapra and DiToro, 1991). For Rattrap Branch this footprint would incorporate 150 m of study reach on the south side of the farm road and continue north of it, past irrigation ponds that lie adjacent to the stream, and into a marginal wetland (Figure 1). That long footprint

presents a challenge in the application of the open water technique to the study of site-specific processes in streams and rivers, even in using a two station approach where oxygen flux is determined from the difference in concentration observed between upstream and downstream locations. The effect of processes occurring within a 20 m reach length on an oxygen flux that is contributed from a 500 m footprint would be a technical challenge to resolve, although Grimm and Fisher (1985) present a promising alternative to do so by manipulating exchange across the air-water and sediment-water boundaries with a plastic sheet.

The relative similarity in oxygen flux between the run and the rest of the reach (Figure 6, 7) reflect the similarity between characteristics of the site and the rest of the stream. Yet there were distinct differences in sediment-water oxygen flux between the two. During both day and night oxygen flux determined at the reach scale was more negative, with an average difference of  $185 \text{ mmol m}^{-2} \text{ d}^{-1}$  (Figure 6). A limitation of the open water technique is the need to estimate a gas transfer velocity in order to calculate the oxygen flux through the ecosystem. Changes in the gas transfer velocity, however, cannot explain differences in the fluxes observed at the run and the reach scale. Instead there is an offset between the two that may be explained by the differential representation of metabolic processes occurring in their footprints. Two characteristics that may be the most descriptive were the abundance of plant and algae at the site and the channelized, as opposed to riffle and pool, morphology. Daytime measurements of oxygen flux at the run site were made in the spring of 2011. At this time plant and algal abundance were high, although patchily distributed, throughout the stream reach. The run site was also located



within a meter downstream of a dense patch of plants and algae, unlike the other sites (Figure 2), which explains the large diurnal variation in oxygen flux observed at the site. The channelized flow at the run site was also the predominant morphology of the stream. With this morphology coarser-grained sediments may also occur along much of the stream reach, as was observed at the run site (Figure 3). The presence of coarser grained sediments is indicative not only that the hydraulic conductivity of the sediments is greater, but also that stream flow applies greater energy to the bed at the site. As a result, the enhancement of hyporheic exchange at the site would be greater than that due to the increase in sediment permeability with the increase in grain size alone.

The oxygen flux determined at the run and at the reach scale were not the same, however. At night, during spring sampling, oxygen fluxes at the run site were half as great at the site scale as they were at the reach scale ( $127 \pm 5 \text{ mmol m}^{-2} \text{ d}^{-1}$  and  $-237 \text{ mmol m}^{-2} \text{ d}^{-1}$ , respectively; Figure 7). During the day oxygen fluxes at the run site were more than four times that observed at the reach scale ( $408 \pm 24 \text{ mmol m}^{-2} \text{ d}^{-1}$  and  $90 \pm 7 \text{ mmol m}^{-2} \text{ d}^{-1}$ , respectively). These differences may be due to greater rates of photosynthesis and greater flow reduction due to high abundance of plants and algae in the footprints. The footprint of the eddy correlation technique was centered on an abundant plant and algal community, while the footprint of the open water technique would reflect the lower mean plant and algal abundance of the reach. The abundance of plants and algae in the run footprint may also explain the smaller magnitude nighttime oxygen fluxes at the site. Dense plant growth is known to slow water velocities near the

bed (e.g. Madsen et al., 2001), this effect may also reduce hyporheic exchange at the site and as a result may locally reduce the magnitude of respiration.

Another difference between the open water footprint and the eddy correlation footprint may be their incorporation of groundwater discharge. Groundwater discharge to a stream can significantly affect calculated rates of respiration (McCutchan et al., 2002; Hall and Tank, 2005), and the rates of inflow would generally increase with increases in water velocity and stream discharge. As the ultimate source of stream water is groundwater a simple mass balance based on stream length can be performed to estimate the contribution of groundwater to the observed oxygen flux. More detail is provided in Koopmans and Berg (in prep). The resulting oxygen fluxes would account for less than 25% of the oxygen fluxes determined with the open water technique at the run site. This may contribute to the differences in oxygen flux observed at the run and reach scales as groundwater discharge through stream edges and cut banks due to enhanced horizontal rather than vertical hydraulic conductivity in stream bed sediments (Chen et al., 2000) would not have been incorporated in the footprint of the eddy correlation technique.

#### *Site-Specific Differences in Oxygen Flux*

Hyporheic exchange scales with the square of grain diameter and water velocity (Packman et al., 2004). Because of this it is not surprising that the magnitude of oxygen flux is small at the pool relative to the reach scale. The mean grain size was smaller and the water velocities were lower than other locations in the reach (Figure 3 and Figure 8, respectively). In sediments with a sufficient fine particle content pore spaces do not

permit hyporheic flow. In these conditions oxygen flux is controlled by the gradient in oxygen concentration and the diffusive boundary layer thickness, which is compressed by increases in water velocity. The rates of oxygen flux observed in the pool ( $-27.4 \pm 1.2$  mmol m<sup>-2</sup> d<sup>-1</sup>), where silts composed 25% of the sediments by volume, was an order of magnitude less than the rate of oxygen consumption at the reach scale at the same time ( $-540 \pm 9$  mmol m<sup>-2</sup> d<sup>-1</sup>; Figure 7). This low rate of oxygen flux may be indicative of benthic exchange that is limited by the diffusion of oxygen through a boundary layer.

At the riffle and tidal sites the water velocities and the sediment grain sizes were conducive to hyporheic exchange, but the rates of oxygen flux were similar to the pool. At water velocities between 12.5 and 17.5 cm s<sup>-1</sup> the mean nighttime oxygen flux at the riffle site was  $-24.9 \pm 0.75$  mmol m<sup>-2</sup> d<sup>-1</sup> (Figure 8C). For comparison, the oxygen flux at the tidal site at a representative velocity (15 cm s<sup>-1</sup>) predicted from the relationship with water velocity (Figure 8D) was a similar  $-21.6$  mmol m<sup>-2</sup> d<sup>-1</sup>. Despite these low rates of oxygen flux, hyporheic exchange appeared to be a dominant mechanism for oxygen consumption at the tidal site. Pore water flushing was generated by an increase in water velocity, and the rate of oxygen consumption quantified at the membrane of the buried optode (Figure 9) was similar to the rate of oxygen flux observed in the water column (Figure 8 D).

An explanation for the low rates of oxygen flux that occurred at the tidal site may be clogging by algal exudates. At the tidal site the surficial sands were discolored by benthic algae (Figure 2, G and H). Exudates released by these algae may have impeded hyporheic exchange. The clogging of pore spaces in Danube River sediments by benthic

algal exudates and associated microbial growth caused a four-fold reduction in the rate of surface water exchange (Battin and Sengshmitt, 1999; measured as a function of the hydraulic conductivity of affected sediments divided by the depth of their occurrence). The concentration of chlorophyll a in those sediments, determined to a depth of 10 cm, was  $0.75 \mu\text{g g}^{-1}$ . To compare the concentration of chlorophyll a at the Rattrap Branch tidal site with the Danube, a simplifying assumption can be applied to tidal sediments that no chlorophyll a was present at a depth greater than 1 cm. This gives a concentration to a depth of 10 cm of  $0.4 \mu\text{g g}^{-1}$  in the center of the channel where benthic algae was minimal and  $1.1 \mu\text{g g}^{-1}$  in the remainder of the channel where benthic algae were in greater abundance. The general similarity in chlorophyll a concentrations suggests that benthic algae may have caused a substantial reduction in hyporheic exchange.

Similarly, the clogging of pore spaces by sediment may explain the low rates of oxygen flux observed at the riffle site. The reduction in hyporheic exchange by the clogging of pore spaces with fine sediments is cumulative, as stream water with suspended material passes into pore spaces the suspended material is left behind. By this mechanism suspended material will accumulate in hyporheic flow paths and restrict flow through them. Bed mobilization, however redistributes the accumulated fine particles in sediments and allows hyporheic exchange to reoccur unimpeded (Schalchli 1992; Rehg et al., 2005). An indication that this process may be responsible for the reduced oxygen fluxes observed at the riffle site are the high rates of oxygen flux determined during a bed-moving storm. The peak in the magnitude of oxygen flux of  $-390 \text{ mmol m}^{-2} \text{ d}^{-1}$  that was observed at the riffle site with a water velocity of  $22 \text{ cm s}^{-1}$  co-occurred with a

migration of ripples across the stream bed, which was recorded that night by the downward-facing ADV as cyclic changes in the distance-to-bed. This step-change in the rate of oxygen consumption from a minimal rate to a high rate with turnover of the stream bed is consistent with the sediment clogging model of hyporheic exchange (Rehg et al., 2005).

Other mechanisms that may contribute to the low rates of oxygen flux across the sediment-water interface at the riffle and tidal sites including carbon bioavailability and the reduction of alternate electron acceptors in riverine sediments at the sites. The low rates of oxygen flux may reflect the local limitation of carbon mineralization due to low bioavailability of benthic organic matter at the sites. In marine sediments, for example, it has generally been found that rate of oxygen consumption in cohesive (fine) sediments exceeds that in permeable sediment due to low organic matter concentrations and availability at the latter (Glud et al., 2008). Coastal streams on the Eastern Shore of Virginia typically carry high concentrations of dissolved organic matter, however, (200 to 540  $\mu\text{M}$ ; Stanhope et al., 2009). The reduction of alternate electron acceptors ( $\text{NO}_3^-$ ,  $\text{Mn(IV)}$ ,  $\text{Fe(III)}$ ,  $\text{SO}_4^{2-}$ , and  $\text{CH}_4$ ) instead of oxygen may also contribute to the relatively low rates of oxygen flux observed at these sites.

#### *Elevated Daytime Respiration*

While the advantages of the high spatial resolution of the eddy correlation technique have been presented, the technique has a similar advantage in the capacity to resolve oxygen fluxes at high temporal resolution, for example over ten minutes, as well (Hume et al.,

2010). Because of the high temporal resolution of the technique discrete oxygen fluxes could be determined at the tidal site where water velocities changed rapidly. In addition the high temporal resolution of the technique was valuable in examining the metabolic response to rapidly changing light conditions at the pool. These observations provide additional evidence for a photosynthate-fueled enhancement of ecosystem respiration (Baines and Pace, 1991). The rate of increase in respiration following a peak in photosynthetic production was 50%. Tobias et al. (2007) used oxygen isotopes to identify daytime rates of respiration in a river and calculated a similar increase of close to 50%. These results would not change the rates of net ecosystem metabolism in streams, but they are evidence that gross primary production may be underestimated. At the pool site in Rattrap Branch the 50% increase in the rate of daytime respiration corresponds to an increase in gross primary production of 50% also. By including more accurate rates of respiration during the day these results suggest greater rates of both autotrophic production and heterotrophic respiration in stream ecosystems.

## **Summary**

Site specific studies of stream ecosystems have been fundamental to understanding the metabolic processes that occur within them. As an example, site-specific studies of hyporheic exchange demonstrated that it may be the primary mechanism responsible for organic matter mineralization in streams (Grimm and Fisher, 1985). While the drivers of hyporheic exchange are well understood, the scales at which it is driven may not be

appropriate for the open water technique with a footprint length of hundreds of meters or more. Using the eddy correlation technique this study investigated site specific (at a scale of square meters) variation in oxygen flux in situ for the first time in a stream. Hyporheic exchange was demonstrated to contribute to the rates of carbon mineralization at a freshwater tidal site. An order of magnitude variation in oxygen flux across the sediment-water interface were determined within a 150 m stream reach and was consistent with site-specific minima in hyporheic exchange due to silt content and clogging of pore spaces by fine sediments and algal exudates. This high spatial variability indicates that stream metabolism is the product of a high degree of heterogeneity in the physical forcing of carbon mineralization in sand-bedded streams.

## Literature Cited

- Baines SB, Pace ML. 1991. The production of dissolved organic matter by phytoplankton and its importance to bacteria: Patterns across marine and freshwater systems. *Limnology and Oceanography* 36:1078–90.
- Baldocchi D. 2003. Assessing the eddy covariance technique for evaluating carbon dioxide exchange rates of ecosystems: past, present and future. *Global Change Biology*:479–92.
- Battin TJ, Sengschmitt D. 1999. Linking Sediment Biofilms, Hydrodynamics, and River Bed Clogging: Evidence from a Large River. *Microbial Ecology* 37:185–96.
- Bayani Cardenas M, Wilson JL, Haggerty R. 2008. Residence time of bedform-driven hyporheic exchange. *Advances in Water Resources* 31:1382–6.
- Bayani Cardenas M, Wilson JL. 2006. The influence of ambient groundwater discharge on exchange zones induced by current–bedform interactions. *Journal of Hydrology* 331:103–9.
- Berg P, Røy H, Janssen F, Meyer V, Jørgensen B, Huettel M, De Beer D. 2003. Oxygen uptake by aquatic sediments measured with a novel non-invasive eddy-correlation technique. *Marine Ecology Progress Series* 261:75–83.
- Berg P, Røy H, Wiberg PL. 2007. Eddy correlation flux measurements: The sediment surface area that contributes to the flux. *Limnology and Oceanography* 52:1672–84.
- Boano F, Revelli R, Ridolfi L. 2009. Quantifying the impact of groundwater discharge on the surface–subsurface exchange. *Hydrological Processes* 2116:2108–16.



- Chapra S, Toro D Di. 1991. Delta method for estimating primary production, respiration, and reaeration in streams. *Journal of Environmental Engineering* 117:640–55.
- Chen X. 2000. Measurement of streambed hydraulic conductivity and its anisotropy. *Environmental Geology* 39:1317–24.
- Crusius J, Berg P, Koopmans DJ, Erban L. 2008. Eddy correlation measurements of submarine groundwater discharge. *Marine Chemistry* 109:77–85.
- Elliott A, Brooks N. 1997. Transfer of nonsorbing solutes to a streambed with bed forms: Theory. *Water Resources Research* 33:123–36.
- Findlay S. 1995. Importance of surface-subsurface exchange in stream ecosystems: the hyporheic zone. *Limnology and Oceanography* 40:159–64.
- Fischer H, Pusch M. 2001. Comparison of bacterial production in sediments, epiphyton and the pelagic zone of a lowland river. *Freshwater Biology* 46:1335–48.
- Frissell C a., Liss WJ, Warren CE, Hurley MD. 1986. A hierarchical framework for stream habitat classification: Viewing streams in a watershed context. *Environmental Management* 10:199–214.
- Fuss, Carolyn L, Smock, Leonard A. 1996. Spatial and temporal variation of microbial respiration rates in a blackwater stream. *Freshwater Biology* 36:339–49.
- Grimm N, Fisher S. 1984. Exchange between interstitial and surface water: implications for stream metabolism and nutrient cycling. *Hydrobiologia* 111:219–28.
- Hall R, Tank J. 2005. Correcting whole-stream estimates of metabolism for groundwater input. *Limnology and Oceanography: Methods* 3:222–9.

- Hornberger GM, Raffensperger JP, Wiberg PL, Eshleman KN. 1998. Elements of physical hydrology. Johns Hopkins University Press. 1998. 312 pp.
- Huettel M, Ziebis W, Forster S. 1996. Flow-induced uptake of particulate matter in permeable sediments. *Limnology and Oceanography* 41:309–22.
- Jørgensen B, Revsbech N. 1985. Diffusive boundary layers and the oxygen uptake of sediments and detritus. *Limnology and Oceanography* 30:111–22.
- Kasahara T, Wondzell SM. 2003. Geomorphic controls on hyporheic exchange flow in mountain streams. *Water Resources Research* 39: 3–14.
- Landon M, Rus D, Harvey F. 2001. Comparison of instream methods for measuring hydraulic conductivity in sandy streambeds. *Ground Water* 38:870–85.
- Larned ST, Packman a. I, Plew DR, Vopel K. 2011. Interactions between the mat-forming alga *Didymosphenia geminata* and its hydrodynamic environment. *Limnology and Oceanography: Fluids and Environments* 1:4–22.
- Long MH, Rheuban JE, Berg P, Zieman JC. 2012. A comparison and correction of light intensity loggers to photosynthetically active radiation sensors. *Limnology and Oceanography: Methods* 10:416–24.
- Lorenzen C. 1967. Determination of chlorophyll and phaeo-pigments: spectrophotometric equations. *Limnology and Oceanography* 12:343–6.
- Luckenbach M, Ross G, Birch A, Curry A. 2008. Evaluating the Relationship Between Impervious Surfaces Within Watersheds and Coastal Water Quality on Virginia's Eastern Shore: Final Report.

- Madsen J, Chambers P, James W. 2001. The interaction between water movement, sediment dynamics and submersed macrophytes. *Hydrobiologia* 444:71–84.
- Marzolf E, Mulholland P, Steinman A. 1994. Improvements to the diurnal upstream-downstream dissolved oxygen change technique for determining whole-stream metabolism in small streams. *Canadian Journal of Fisheries and Aquatic Science* 51:1591-1599.
- McCutchan J, Saunders J. 2002. Effects of groundwater flux on open-channel estimates of stream metabolism. *Limnology and Oceanography* 47:321–4.
- Morrice J, Valett H. 1997. Alluvial characteristics, groundwater–surface water exchange and hydrological retention in headwater streams. *Hydrological Processes* 11:253–67.
- Naegeli M, Uehlinger U. 1997. Contribution of the hyporheic zone to ecosystem metabolism in a prealpine gravel-bed-river. *Journal of the North American Benthological Society* 16:794–804.
- Packman A, Salehin M, Zaramella M. 2004. Hyporheic exchange with gravel beds: Basic hydrodynamic interactions and bedform-induced advective flows. *Journal of Hydraulic Engineering* 130:647–56.
- Packman AI, Salehin M. 2003. Relative roles of stream flow and sedimentary conditions in controlling hyporheic exchange. *Hydrobiologia* 494:291–7.
- Pinckney J, Papa R, Zingmark R. 1994. Comparison of high-performance liquid chromatographic, spectrophotometric, and fluorometric methods for determining chlorophyll a concentrations in estuarine sediments, *Journal of Microbiological Methods* 19:59–66.

- Pusch M, Schwoerbel J. 1994. Community respiration in hyporheic sediments of a mountain stream (Steina, Black Forest). *Archiv für Hydrobiologie* 130:35–52.
- Pusch M. 1996. The metabolism of organic matter in the hyporheic zone of a mountain stream, and its spatial distribution. *Hydrobiologia* 323:107–18.
- Rehg KJ, Packman AI, Ren J. 2005. Effects of suspended sediment characteristics and bed sediment transport on streambed clogging. *Hydrological Processes* 19:413–27.
- Revsbech N. 1989. An oxygen microsensor with a guard cathode. *Limnology and Oceanography* 34:474–8.
- Schälchli U. 1992. The clogging of coarse gravel river beds by fine sediment. *Hydrobiologia* 235/236:189–97.
- Stonedahl SH, Harvey JW, Wörman A, Salehin M, Packman AI. 2010. A multiscale model for integrating hyporheic exchange from ripples to meanders. *Water Resources Research* 46:n/a–n/a.
- Tobias C, Bohlke J, Harvey J. 2007. The oxygen-18 isotope approach for measuring aquatic metabolism in high productivity waters. *Limnology and Oceanography* 52:1439–53.
- Vannote R. 1980. The river continuum concept. *Canadian Journal of Fisheries and Aquatic Sciences* 37:130–7.
- Wanninkhof R. 1990. Gas Exchange Rates for a First-Order Stream Determined With Deliberate. *Water Resources Research* 26:1621–30.

- Wörman A, Packman AI, Marklund L, Harvey JW, Stone SH. 2007. Fractal topography and subsurface water flows from fluvial bedforms to the continental shield. *Geophysical Research Letters* 34:L07402.
- Wroblicky G, Campana M, Valett HM, Dahm CN. 1998. Seasonal variation in surface-subsurface water exchange and lateral hyporheic area of two stream-aquifer systems. *Water Resources Research* 34:317–28.
- Young RG, Huryn AD. 1998. Comment: Improvements to the diurnal upstream-downstream dissolved oxygen change technique for determining whole-stream metabolism in small streams. *Canadian Journal of Fisheries and Aquatic Sciences* 55:1784–5.
- Zarnetske JP, Haggerty R, Wondzell SM, Bokil V a., González-Pinzón R. 2012. Coupled transport and reaction kinetics control the nitrate source-sink function of hyporheic zones. *Water Resources Research* 48:n/a–n/a.
- Zhou D, Mendoza C. 1993. Flow through porous bed of turbulent stream. *Journal of Engineering Mechanics* 119:365–83.

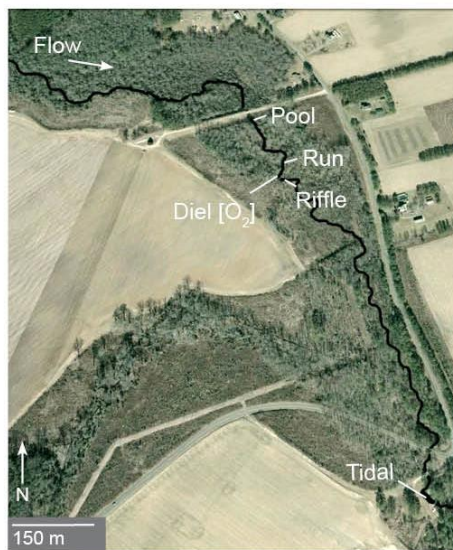


Figure 1. Map of the Rattrap Creek study area in Accomack County on the eastern shore of Virginia ( $37^{\circ} 39' 15$  N,  $75^{\circ} 41' 25$  W). The pool, riffle, run and tidal sites are where the eddy correlation technique was applied. Diel oxygen concentration changes were used to independently determine oxygen flux with the open water technique.



Figure 2. Locations of site-specific eddy correlation measurement of oxygen flux shown above (left) and below water (right). **A** and **B** are the pool site, **C** and **D** are the run site, **E** and **F** are the riffle site, **G** and **H** are the tidal site.

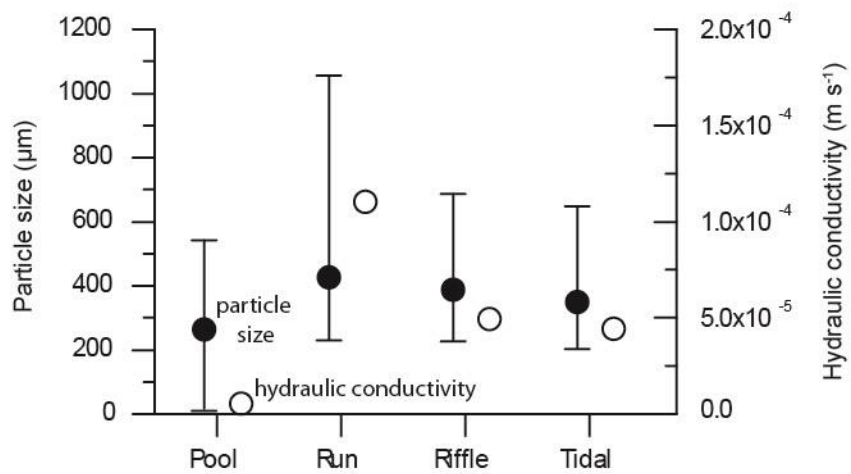


Figure 3. The grain size distribution and hydraulic conductivities to a depth of 7 cm at the study sites. The filled circles represent the median grain diameter. The diameter at the 10th percentile and 90th percentile are represented by the lower and upper bounds. The hydraulic conductivities are represented by the open circles.



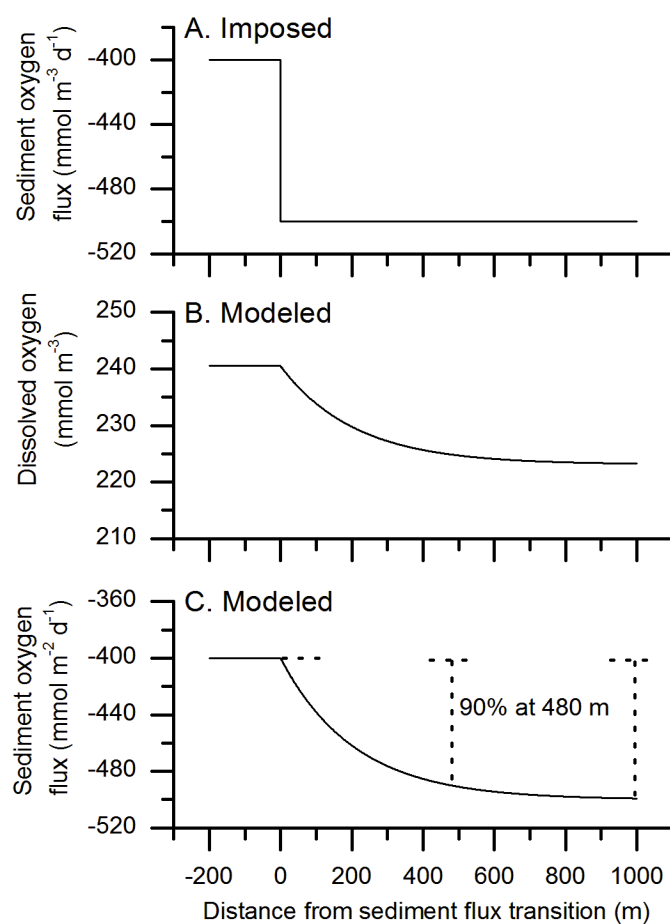


Figure 4. Modeled prediction of the downstream distance at which a measured oxygen flux reaches 90% of the imposed flux. **A** A transition in the oxygen uptake rate of riverine sediments was imposed at 0 m. The effect on **B** the  $\text{O}_2$  concentration and **C** the sediment  $\text{O}_2$  flux was predicted. The closest point at which 90% of the imposed flux was observed was at a distance of 480 m.

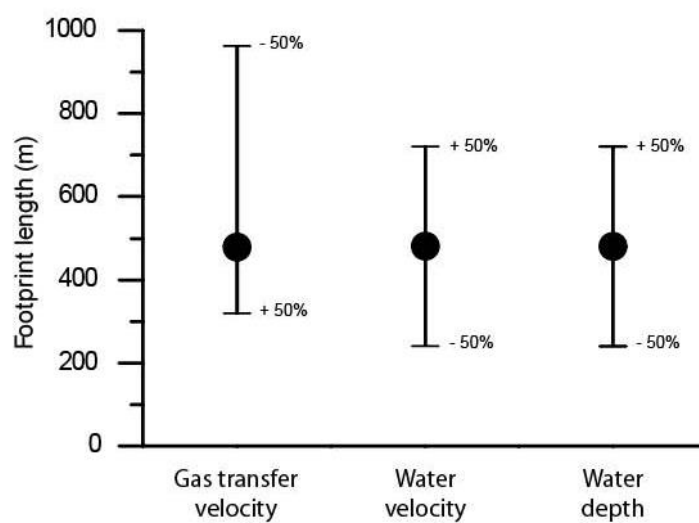


Figure 5. Dependency of the modeled 90% flux footprint on the gas transfer velocity, the water velocity, and the water depth with central values of 5.8 m d<sup>-1</sup>, 0.14 m s<sup>-1</sup>, and 0.1 m depth.

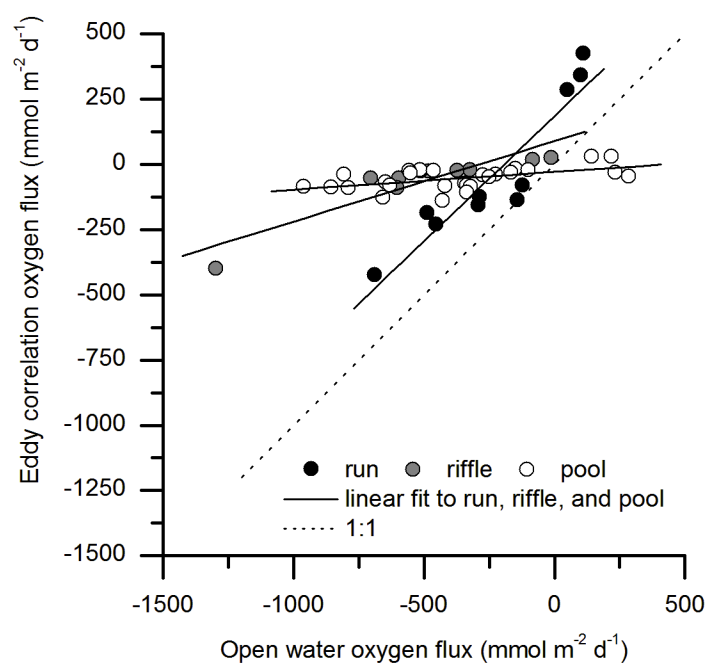


Figure 6. Site-specific oxygen flux determined with the eddy correlation technique at the run, riffle, and pool sites presented as a function of the reach scale open water oxygen flux.

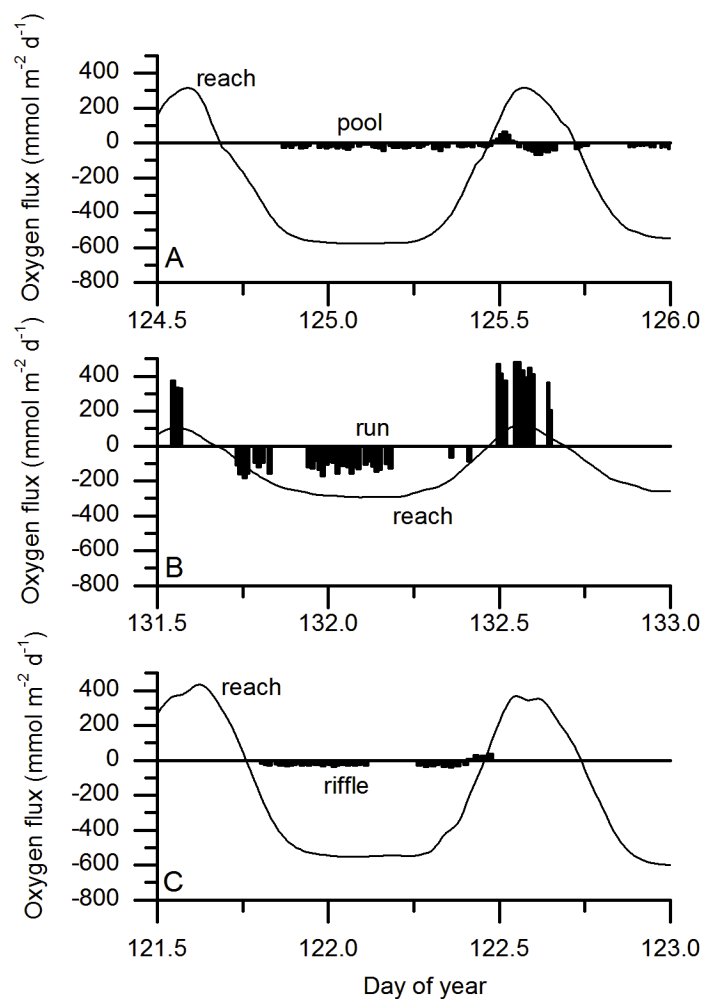


Figure 7. Examples of the diurnal changes in site-scale and reach-scale oxygen fluxes at the **A** pool, **B** run, and **C** riffle, sites. The fluxes at the run site were determined in May of 2011 while those at the pool and riffle sites were determined in May of 2012.

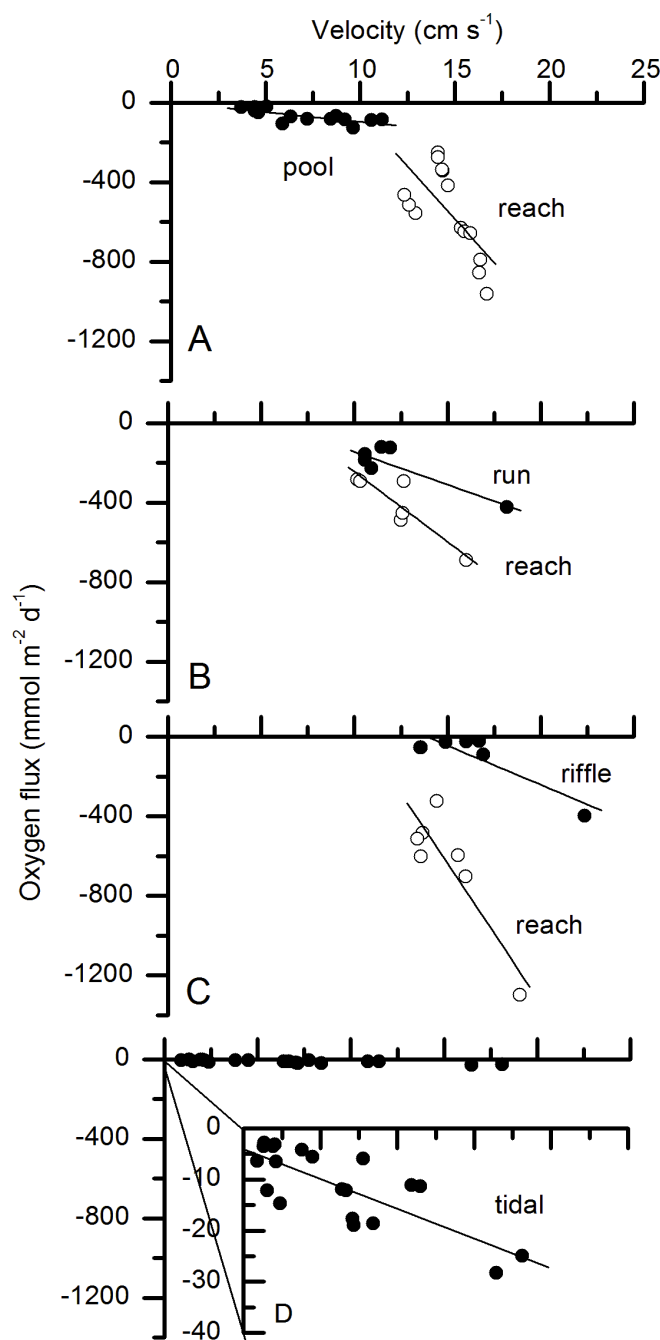


Figure 8. Simultaneous, nighttime oxygen fluxes presented as a function of mean water velocity at the reach scale (open circles) and site-scale (closed circles). Comparative data are presented at the **A** pool, **B** run, **C** riffle, and **D** tidal sites. Each symbol in **A**, **B**, and **C** represents a mean duration of 95 minutes. Each symbol in **D** represents a mean duration of 10 minutes.

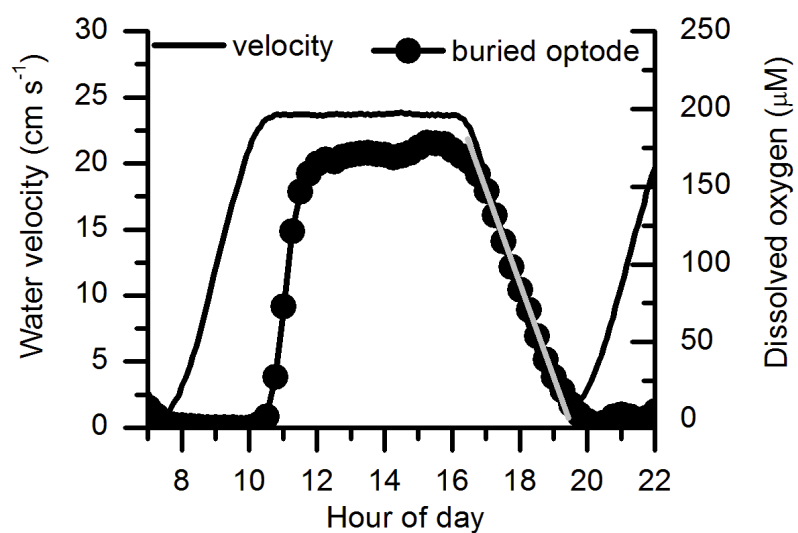


Figure 9. The oxygenation of sediment pore water to a depth of 1 cm presented with water velocity at the freshwater tidal site. The linear change in dissolved oxygen concentration from hour 17 to 19 extrapolated to 1 cm depth corresponds to an oxygen flux of  $-29 \text{ mmol m}^{-2} \text{ d}^{-1}$ .

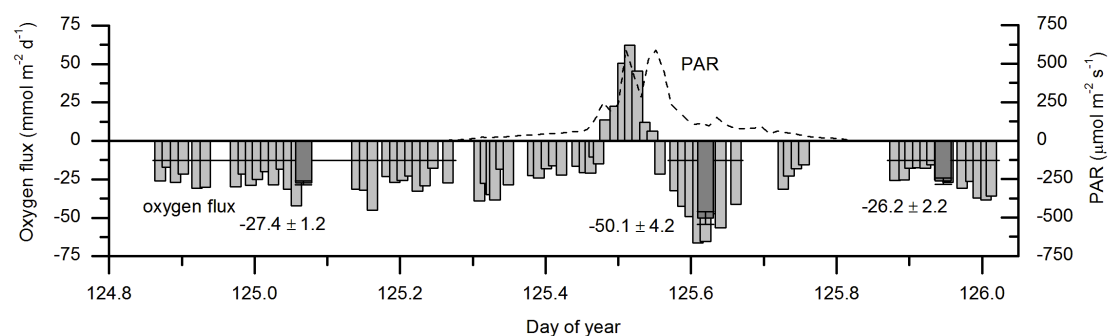


Figure 10. Oxygen flux determined with the eddy correlation technique at the pool site in the spring of 2012. The site received direct solar irradiation for two hours at midday. An enhancement in the respiration rate was observed in the afternoon shade (dark grey bars represent mean and standard error, horizontal lines represent the averaging interval).

## Chapter 5

### Conclusion and Synthesis



The scientific impacts of this dissertation include the efficacy of novel experimental approaches employed and the quantification of drivers of groundwater discharge and oxygen flux. The experimental approach was designed to examine both groundwater discharge and oxygen flux at high spatial resolution (tens of square meters or less) and a high temporal resolution (15 minutes or less) using techniques that minimized or eliminated interference with in situ flow, including dye displacement seepage meters and eddy correlation. The high spatial and temporal resolution techniques were complemented by techniques which integrated processes over spatial scales of kilometers (radon mapping) or hundreds of meters (open water technique). The drivers of groundwater discharge and oxygen flux were then evaluated using techniques at both scales.

At a coarse spatial scale, groundwater discharge to portions of the lagoons of the Eastern Shore of Virginia was the greatest within a kilometer of shore, occurring in the fully saline Castle Ridge Creek and the Machipongo River at rates of  $3.9 \text{ cm d}^{-1}$  and  $2.5 \text{ cm d}^{-1}$ , respectively. The activity of radon in surface waters indicated that groundwater discharge to the outer lagoons was less significant, although the high water velocities along tidal channels in the lagoons may obscure relatively small groundwater input to the area (Appendix I).

At a fine temporal and spatial scale, groundwater discharge to Sand Hill Beach reached a short-lived peak of  $80 \text{ cm d}^{-1}$  at low tide, and the inflow of overlying water into submarine sediments occurred across the subtidal measurement area ( $70 \text{ m}^2$ ) at high tide (Chapter 2). Neither the short-lived peak nor the inflow of overlying water, to our

knowledge, have been previously observed with manually operated seepage meters, only with their automated counterparts whose expense limits the spatial resolution of their deployments. The confirmation of these processes and the spatial extent of their occurrence may allow more accurate modeling of the rates of seawater recirculation through intertidal sands. This process is relevant to coastal and marine geochemistry as the interaction of reduced terrestrial groundwaters and oxygenated seawater in submarine sediments creates redox gradients that cause the accumulation of redox sensitive minerals such as phosphorus and thorium (a radioactive parent of radium; Moore 1999; Charette et al., 2005; Charette and Sholkovitz, 2006 ).

Oxygen flux across the sediment-water interface in a coastal stream was also subject to control at fine spatial and temporal scales. Physical drivers of ecosystem processes were important in the stream with changes in water velocity accounting for 90% and 97% of the variation in respiration before and after a stage shift (Chapter 4). The pre and post stage shift relationships, however, indicate that there is a complexity to velocity driven respiration that may not be resolved at the reach scale of hundreds of meters. Contributing factors may include spatial and temporal variation in water depth, stream geometry, grain size, groundwater inflow, and organic matter bioavailability among other factors.

The gas transfer velocity alone could not explain the differences in oxygen flux observed at the reach and site specific scales. While oxygen fluxes at the riffle and pool sites were an order of magnitude smaller than oxygen fluxes at the reach scale, oxygen fluxes at the run site had a 1:1 correspondence with fluxes at the reach scale but were

consistently more positive (by  $180 \text{ mmol m}^{-2} \text{ d}^{-1}$ ; Chapter 5, Figure 6). The latter relationship cannot be reconciled by an alteration of the gas transfer velocity, indicating that the differences are due to the different metabolic processes represented in the footprints of the two techniques.

The footprint of the eddy correlation technique was approximately ten meters in length, aligned with the thalweg of the stream, and half a meter in width. The footprint of the open water technique incorporated the stream width for many hundreds of meters upstream of the point of measurement. An enhancement of respiration at the stream margins relative to the stream thalweg could explain the differences observed between the two scales of measurement. Fine sediments are generally winnowed from the thalweg to the stream margins due to the gradient in downstream water velocities in a stream cross section (e.g., Julien and Anthony, 2002). As a result, sediments at the stream margin would be expected to be finer than at the thalweg and would have a greater organic matter content. It may be that these characteristics, or others, enhance rates of oxygen consumption there. While finer sediments at the stream margins would be expected to attenuate rates of hyporheic exchange, a mechanism which allows for a highly efficient respiration of organic matter (Huettel et al., 2003), coarse sediments may also limit benthic respiration by limiting the surface area available for bacterial attachment (Jones, 1995). Additionally, carbon limitation controls benthic respiration in some stream ecosystems (e.g., Pusch and Schwoerbel 1994; Jones 1995).

A longitudinal variation in oxygen consumption in streambed sediments may also contribute to the greater rates of oxygen consumption determined at the reach scale. Of

the four sites at which the eddy correlation system was deployed a mechanism was identified which may have suppressed hyporheic exchange and oxygen consumption at each of the four sites. Those mechanisms include the lack of hyporheic flow through cohesive sediments at the pool site, the attenuation of water flow around benthic macroalgae at the run site, and the clogging of medium grained sands by fine particles and a benthic algal mat at the riffle and tidal sites respectively (Chapter 5). It may be that greater rates of respiration occur due to hyporheic exchange through medium-grained sands in the thalweg of the stream where neither benthic macroalgae nor ripples were present, as would describe most of the stream bed.

Alternately, point sources of low oxygen water to the stream may also contribute to the greater rates of oxygen consumption determined at the reach scale. Dent et al., (2001) identified locations of subsurface upwelling of groundwater to Sycamore Creek AZ that in many cases altered nutrient concentrations hundreds of meters downstream of the point of occurrence. They also identified a point source of nutrients from which the nutrient concentration in the stream was elevated for thousands of meters downstream. An uneven distribution in the upwelling of groundwater at Rattrap Branch or the inflow of water from an irrigation pond upstream of the point of measurement may contribute to the differences observed. Diminishing the strength of this explanation, however, little variation in oxygen flux (<10% difference) was found when oxygen fluxes were calculated based on oxygen concentrations measured 200 meters downstream from the primary point of measurement.

This study conclusively demonstrated fine spatial and temporal scale variation in oxygen flux across the sediment-water interface (Chapter 5). Oxygen consumption in permeable sediments is driven by hyporheic exchange (Glud, 2008). Bedforms may act as hot spots for hyporheic exchange as the pressure differential on the upstream and downstream sides will induce hyporheic flow through them (Huettel, 1996). Based on chamber studies in permeable marine sediments, little oxygen consumption occurs in pore waters despite flow in overlying water when bedforms are not present (Cook et al., 2007). Yet nighttime oxygen consumption at a portion of the stream with a rippled bed and medium-grained sands was one-twentieth of simultaneous fluxes at the reach scale ( $-25 \text{ mmol m}^{-2} \text{ d}^{-1}$  and  $-500 \text{ mmol m}^{-2} \text{ d}^{-1}$ , respectively), and one-fifth of the rate of nighttime oxygen consumption at the run site ( $-127 \text{ mmol m}^{-2} \text{ d}^{-1}$ ; Chapter 5, Figure 7). These are among the first investigations of spatial variation in site specific oxygen flux under in situ hydrodynamic conditions in streams and they revealed a greater variance in oxygen flux than was indicated by chamber investigations, for example a two-fold differences from a riffle to a pool (Pusch, 1997).

The results are consistent with a strong site-specific control of oxygen flux, perhaps by site specific control of hyporheic exchange through clogging of pore spaces in permeable sediments. The availability of pore spaces for hyporheic exchange and their clogging by fine mineral or organic particles may be integral to the behavior of sand-bedded stream ecosystems. Stream ecosystem respiration declines with disturbance intensity (Houser et al., 2009) and the decline may be in part due to the clogging of sediment pore spaces by terrestrial fine-grained sediment. Additionally, with

eutrophication of stream ecosystems the abundance of particulate organic matter in suspension increases. This material may also clog pore spaces in permeable sediments, just as biocatalytic filters clog under excessive organic matter loads (Huettel et al., 2003). This may cause a reduction in the capacity of the stream to mineralize organic carbon with a direct effect on nitrogen cycling as well. The reduced efficiency of nitrate removal from eutrophic streams (Mulholland et al., 2008) may include this as a mechanism. Yet while the physical effects of clogging on pore water exchange have been examined in flume studies, the ecological effects have not been examined in situ in stream ecosystems. With the eddy correlation technique, these and other processes can be examined at a finer spatial scale corresponding to the scales over which many morphological characteristics of streams vary.

At the terrestrial-atmosphere interface over four hundred eddy covariance towers are currently recording carbon flux (Fluxnet, 2013). With a median record length of six years these towers have quantified 2400 years of land-atmosphere exchange. Some of these towers incorporate aquatic ecosystems in their footprint, but given that freshwater ecosystems receive 50% to 75% of net terrestrial ecosystem production and that twice as much carbon is mineralized or stored within them as they export to the oceans (Cole et al., 2007; Battin et al., 2008; Aufdenkampe et al., 2011), greater sampling of oxygen fluxes through freshwater ecosystems is warranted. In the largest dataset on stream metabolism, the USGS has quantified oxygen flux across the air-water interface in 460 reaches of 166 streams in 23 states (Melching and Flores, 1999). These data, in combination with approximately 300 other studies, constitute the available dataset on

oxygen fluxes based on trace gas addition (Raymond et al., 2012). Oxygen fluxes determined seasonally and at multiple spatial scales in Rattrap Branch are representative of observations of oxygen flux in aquatic ecosystems that will improve our understanding of their role in global carbon and nutrient cycles.

## Literature Cited

- Aufdenkampe AK, Mayorga E, Raymond PA, Melack JM, Doney SC, Alin SR, Aalto RE, Yoo K. 2011. Riverine coupling of biogeochemical cycles between land, oceans, and atmosphere. *Frontiers in Ecology and the Environment* 9:53–60.
- Battin TJ, Kaplan LA, Findlay S, Hopkinson CS, Marti E, Packman AI, Newbold JD, Sabater F. 2008. Biophysical controls on organic carbon fluxes in fluvial networks. *Nature Geoscience* 1:95–100.
- Charette MA, Sholkovitz ER, Hansel CM. 2005. Trace element cycling in a subterranean estuary: Part 1. Geochemistry of the permeable sediments. *Geochimica et Cosmochimica Acta* 69:2095–109.
- Charette MA, Sholkovitz ER. 2006. Trace element cycling in a subterranean estuary: Part 2. Geochemistry of the pore water. *Geochimica et Cosmochimica Acta* 70:811–26.
- Cole JJ, Prairie YT, Caraco NF, McDowell WH, Tranvik LJ, Striegl RG, Duarte CM, Kortelainen P, Downing JA, Middelburg JJ. 2007. Plumbing the global carbon cycle: integrating inland waters into the terrestrial carbon budget. *Ecosystems* 10:172–85.
- Cook PL, Wenzhöfer F, Glud RN, Janssen F, Huettel M. 2007. Benthic solute exchange and carbon mineralization in two shallow subtidal sandy sediments: Effect of advective pore-water exchange. *Limnology and Oceanography* 52:1943–63.



- Dent CL, Grimm NB, Fisher SG. 2001. Multiscale effects of surface-subsurface exchange on stream water nutrient concentrations. *Journal of the North American Benthological Society* 20:162–81.
- Glud RN. 2008. Oxygen dynamics of marine sediments. *Marine Biology Research* 4:243–89.
- Houser JN, Mulholland PJ, Maloney KO. 2009. Catchment disturbance and stream metabolism: patterns in ecosystem respiration and gross primary production along a gradient of upland soil and vegetation disturbance.
- Huettel M, Røy H, Precht E, Ehrenhauss S. 2003. Hydrodynamical impact on biogeochemical processes in aquatic sediments. In: *The Interactions between Sediments and Water*. Springer. pp 231–6.  
[http://link.springer.com/chapter/10.1007/978-94-017-3366-3\\_31](http://link.springer.com/chapter/10.1007/978-94-017-3366-3_31). Last accessed 06/07/2013
- Huettel M, Ziebis W, Forster S. 1996. Flow-induced uptake of particulate matter in permeable sediments. *Limnology and Oceanography* 41:309–22.
- Jones JB. 1995. Factors controlling hyporheic respiration in a desert stream. *Freshwater Biology* 34:91–9.
- Julien PY, Anthony DJ. 2002. Bed load motion and grain sorting in a meandering stream. *Journal of Hydraulic Research* 40:125–33.
- Melching CS, Flores HE. 1999. Reaeration equations derived from US Geological Survey database. *Journal of Environmental Engineering* 125:407–14.

- Meysman FJR, Galaktionov OS, Cook PLM, Janssen F, Huettel M, Middelburg JJ. 2007. Quantifying biologically and physically induced flow and tracer dynamics in permeable sediments. *Biogeosciences* 4:627–46.
- Moore WS. 1999. The subterranean estuary: a reaction zone of ground water and sea water. *Marine Chemistry* 65:111–25.
- Mulholland PJ, Helton AM, Poole GC, Hall RO, Hamilton SK, Peterson BJ, Tank JL, Ashkenas LR, Cooper LW, Dahm CN. 2008. Stream denitrification across biomes and its response to anthropogenic nitrate loading. *Nature* 452:202–5.
- Pusch M. 1996. The metabolism of organic matter in the hyporheic zone of a mountain stream, and its spatial distribution. *Hydrobiologia* 323:107–18.
- Pusch M, Schwoerbel J. 1994. Community respiration in hyporheic sediments of a mountain stream (Steina, Black Forest). *Archiv für Hydrobiologie* 130:35–52.
- Raymond PA, Zappa CJ, Butman D, Bott TL, Potter J, Mulholland P, Laursen AE, McDowell WH, Newbold D. 2012. Scaling the gas transfer velocity and hydraulic geometry in streams and small rivers. *Limnology & Oceanography: Fluids & Environments* 2:41–53.

## Appendix I.

Identification of Groundwater Discharge to Ramshorn Channel, Hog Island  
Bay, and Cobb Bay by Radon Mapping

## Overview

Submarine groundwater discharge has been defined as referring to all pore water discharge into overlying seawater, whether the pore water is fresh, brackish, or saline (Burnett et al., 2003). Regardless of the source of water, groundwater discharge is generally highly enriched in nutrients relative to the water column. Recirculated seawater may carry high concentrations of nitrate or ammonium as a result of organic matter mineralization in sediments. This may be an especially important pathway for the delivery of nutrients to coastal waters adjacent to salty marshes, where organic matter is abundant in pore water (e.g. Krest et al., 2000). Terrestrially-derived groundwater discharge may carry anthropogenic nutrient sources in addition to those that occur naturally. As a result, groundwater discharge has been implicated in the eutrophication of many coastal waters (Johannes, 1980; Paerl, 1997; Valiela et al., 1999; Giblin and Gaines, 1999).

On the eastern shore of Virginia the small watersheds of the Delmarva Peninsula make substantial groundwater discharge to the coastal lagoons unlikely, however the enrichment of surficial aquifers with fertilizer-derived nitrogen (Hamilton and Helsel, 1995) as well as substantial salt marshes make groundwater discharge a likely source of nutrients to coastal waters, as has been documented on the Chesapeake Bay side of the Delmarva Peninsula (Reay and Gallagher, 1995).

To identify groundwater discharge to coastal waters many studies have utilized radon as a naturally occurring groundwater tracer. Radon-222 is a gas and is part of the uranium-238 decay series. It has a half-life of 3.8 days and is a daughter of radium-226 .

Radium-226 itself may be enriched in coastal aquifers by dissolution-sorption reactions which occur at the redox interface which between oxygenated surface waters recirculating through sediments and anoxic waters of terrestrial origin (Charette and Sholkovitz, 2006).

### **Study Site**

The Virginia Coast Reserve is comprised of 110 km of uninhabited barrier islands, shallow lagoons, and extensive mudflats and marshes abutting rural agricultural watersheds on the Atlantic side of the lower Delmarva Peninsula. The population density of the region is low, with a mean of 28 km<sup>-2</sup> (U.S. Census Bureau, 2000). Future residential and commercial development of barrier islands is limited by the extent of the Nature Conservancy's Virginia Coast Reserve, but nutrient and fecal coliform pollution of surface waters and surficial groundwaters puts the bays at risk of habitat and fishery loss due to eutrophication. The average nitrate concentration of surficial groundwaters beneath agriculture on the Delmarva Peninsula is 580 µm (n = 296; Hamilton and Helsel, 1992), two orders of magnitude greater than dissolved inorganic nitrogen concentrations in Hog Island Bay (Tyler et al., 2001). Biological and hydrologic conditions which aid in removing nutrients and fecal coliform bacteria in these environments are important to the economic growth of the region.

## Methods

The enrichment of radon in the water column in Cobb Bay, Ramshorn Channel, and Hog Island Bay was quantified in March of 2007. On March 12<sup>th</sup> radon mapping was conducted along the primary channel in Cobb Bay. On March 13<sup>th</sup> an extensive transect was conducted from the Ramshorn Channel north of Oyster Virginia, through the shallow waters of Castle Ridge Creek and Fowling Point Gut to Red Bank Creek and finally the inner portion of the Machipongo River in Hog Island Bay. On March 30<sup>th</sup> a transect was conducted shore-ward from near the mouth of Hog Island Bay, across the bay along the channel formed by the Machipongo River that continued inland to Willis Wharf. It is worth noting that discharge through the Machipongo River is predominantly tidal, with only a minimal freshwater contribution. A discussion of sediments and the flow environment in Hog Island Bay is available in Lawson et al. (2007).

In order to quantify radon activity in the water column of the channels and lagoons, six RAD7 instruments were placed in the cabin of a research boat and connected through a manifold in-line with a water-air exchanger which sat on the gunnel. As transects were conducted water was continually pumped in to the air-water exchanger allowing continuous determination of the radon concentration in water (Burnett and Dulaiova, 2003). Simultaneous measurements of water temperature and salinity were also made using a YSI instruments salinity and temperature sensor and logger (YSI 3380). Radon, salinity and temperature data were logged simultaneously with the GPS coordinates of their observation to a shipboard computer. Radon activities were recorded

every three minutes and binned into 20 minute intervals to improve the statistical strength of each observation (64 counts in 20 minutes is equivalent to  $30 \text{ Bq m}^{-3}$ ).

Radon activity in groundwater in the region surficial groundwater samples were collected from two freshwater wells in Northampton County at the hillslope beside Cobb Mill Creek (A,B; Figure 1) and from five brackish wells in Accomack County at Phillips Creek (C through G; Figure 1). These samples were used to identify the concentration of radon in source groundwater to the coastal lagoons. To quantify radon in those samples water was collected in a 120 ml serum vial according to appropriate gas sampling techniques (gas tight collection tubing was used to introduce water slowly the base of the vial, and the displaced volume of water was twice the fill volume). Immediately after collection the serum vials were sparged in-line with a DurrIDGE Instruments Rad7 radon gas detector.

The radioactive decay series of radon-222 is both a source and a sink for radon in the water column. The immediate parent of radon-222 is radium-226 which may be enriched in surface waters. To account for radon supplied by radium in suspension, twelve samples in excess of 60 l each were collected to quantify the concentration of parent radium 226 in the water column. These water samples were gravity-drained (at rates of less than 1 liter per minute) through manganese impregnated acrylic fibers. Radium-226 adsorbs to the fiber, and the resulting production of radon-222 by radioactive decay was quantified by in-line gas exchange through a RAD7 instrument (Moore and Arnold, 1996). Similarly the radioactive decay of radon-222 to polonium-218 at a rate given by the half-life of radon-222 is a relevant sink for radon in coastal waters.

In order to quantify groundwater discharge to the water column using radon-222 the relevant sources and sinks of radon-222 must be accounted for. Assuming steady state conditions these can be expressed as a mass balance where the sources of radon equal the sinks, specifically

$$gw + pw + {}^{226}Ra = evasion + mixing + {}^{218}Po \quad (1)$$

where *gw* is the groundwater input, *pw* is the pore water input,  ${}^{226}Ra$  is the in situ decay of radium-226 into radon-222, *evasion* is the loss of radon across the air-water interface, *mixing* is the loss of radon to neighboring waters, and  ${}^{218}Po$  is the loss due to radioactive decay of radon-222. Pore waters that actively exchange with overlying waters can be an additional source of radon to coastal waters. Because this locally recirculated water would generally be a pathway for the remineralization of nutrients, as opposed to a nutrient subsidy, accounting for this source was relevant to the study. While the rate of delivery of pore water radon-222 was not determined in this study, it is generally expected to be small. Literature values support this assumption. In 2-m deep waters of the St George Sound of the Gulf of Mexico, where the radon-222 activity of surficial sediments was 2170 Bq m<sup>-3</sup>, the diffusion of pore water radon-222 to surface waters was 2.8 Bq m<sup>-2</sup> d<sup>-1</sup> (Lambert and Burnett, 2003). Despite differences in lithology, that same rate of pore water diffusion of radon-222 was assumed for this study.

Radon losses both to the atmosphere and due to mixing are site specific. In this study we applied relevant gas transfer velocities from literature models of carbon dioxide



gas transfer in estuarine systems based on water depth and tidal velocity (Raymond and Cole, 2001). Groundwater discharge was not determined to the lagoon directly, where the large fetch would suggest that wind speed would control rates of gas exchange. The gas transfer rates of carbon dioxide were converted to the relevant gas transfer rates for radon-222 by their Schmidt number, which is a proportion of the viscous to molecular diffusivity of a gas in water at a known temperature, as follows

$$k_{Rn} = k_{CO_2} \left( \frac{Sc_{Rn}}{Sc_{CO_2}} \right)^{-n} \quad (2)$$

where  $k_{Rn}$  and  $k_{CO_2}$  refer to the gas transfer velocities of radon and carbon dioxide, respectively, and  $Sc_{Rn}$  and  $Sc_{CO_2}$  refer to their Schmidt numbers. The exponent  $n$  can take a value between 1/2 and 2/3 depending on the turbulent state of the water, where 1/2 applies to highly turbulent water in rivers where gas exchange occurs approximates a surface renewal model and 2/3 reflects gas transfer in conditions with low turbulence (Jahne et al., 1987). The latter value was assumed to better approximate the calm waters sampled during this study. In order to determine the rate of radon flux to the atmosphere the resulting gas transfer velocities for radon were multiplied by the observed radon activities in surface waters. This calculation assumes that the background activity of radon above surface waters is zero. The other relevant losses of radon due to mixing at the study locations were assumed to be minimal due to the extensive length-scale over which radon enrichment was observed (3 to 4 kilometers).

## Observations and Discussion

Greater activities of radon-222 were observed in near shore waters within a hundred meters of terrestrial fringing marshes than in offshore waters (Figure 1). Radon in surficial groundwater was enriched 250 times relative to the activity in the water column of the outer portions of the lagoons indicating its usefulness as a terrestrial groundwater tracer. Groundwater samples had an average activity of  $3350 \pm 590 \text{ Bq m}^{-3}$ ,  $n = 7$ , while in the outer portions of both Cobb Bay and Hog Island Bay the radon activity was  $13 \text{ Bq m}^{-3}$  or lower. Of the well samples, the lowest radon activities ( $1630$  and  $1430 \text{ Bq m}^{-3}$ ) were observed in water samples at the lowest and highest salinities ( $0$  and  $5.5$  parts per thousand, respectively), suggesting that radium-226 may be enriched at the lowest salinities in the studied surficial aquifer.

Continuous measurements of radon concentrations were made with one exception. In the shallow waters of Fouling Point Gut algal abundance was high and the surfactant qualities of algal exudates were the likely cause of fouling of the air-water exchanger. The exchanger was emptied and rinsed then reconnected but the substantial temporal averaging is inherent in the radon mapping technique, and as a result the suppressed radon activities observed in Fouling Point Gut are due in part to this interruption in measurement. With that one exception radon activities were almost uniformly greater nearshore than offshore. The amount of radon activity supported by radioactive decay of radium-226 in situ was small throughout the transects with a mean of  $0.8 \pm 0.11 \text{ Bq m}^{-3}$  ( $n = 10$ , mean  $\pm$  s.e.), indicating that inputs of radon-222 due to saline, brackish, or fresh groundwater inflow were important.

The observation of increased groundwater discharge within a few hundred meters of shore is consistent with observations at many coastal sites. Groundwater discharge predominantly occurs near shore decreases exponentially with distance from it at scales of tens to hundreds of meters (Cable et al., 1997; Taniguchi et al., 2003). The relatively low radon activity in lagoon waters supports those observations. Exceptions occur, however, where geologic features restrict the exchange of the surficial aquifer with the overlying water (Cherkauer and Nader, 1989). Due to the prevalence of fine sediments which have an associated low hydraulic conductivity similar process may contribute groundwater to, for example, the Machipongo River Channel hundreds of meters or more from shore. The volume of tidally exchanged water in the channel, however, would dilute groundwater inputs of radon if they do occur there.

The rate of groundwater discharge was quantified for two locations, Castle Ridge Creek, just north of the northern end of Ramshorn Channel, and the inner portion of the Machipongo River between Red Bank Creek and Willis Wharf. While these areas are not specifically delineated in Figure 1 they correspond to five observations of radon activities with a mean of  $65.7 \pm 1.8 \text{ Bq m}^{-3}$  (mean  $\pm$  s.e.) in Castle Ridge Creek and four observations of radon activity with a mean of  $56.5 \pm 3.3 \text{ Bq m}^{-3}$  in the Machipongo River. The losses of radon due to in situ radioactive decay are a function of the half-life of radon and the radon concentration. Taking into account the water depth of the two sites of 1 m for the Castle Ridge Creek and 10 m for the inner portion of the Machipongo River these terms account for losses of  $8.6 \text{ Bq m}^{-2} \text{ d}^{-1}$  and  $74 \text{ Bq m}^{-2} \text{ d}^{-1}$  at the two sites respectively. Based on water depth and tidal velocities, the predicted gas transfer velocities for Castle

Ridge Creek (assumed 1 m deep with tidal velocities of  $0.1 \text{ m s}^{-1}$ ) and the inner Machipongo River (10 m deep with tidal velocities of  $0.2 \text{ m s}^{-1}$ ) were  $2.0 \text{ m d}^{-1}$  and  $0.39 \text{ m d}^{-1}$ , respectively. The corresponding air-water radon fluxes at the sites were  $130 \text{ Bq m}^{-2} \text{ d}^{-1}$  and  $22 \text{ Bq m}^{-2} \text{ d}^{-1}$ , respectively. Based on a mass balance for radon-222 the resulting groundwater fluxes were  $3.9 \text{ cm d}^{-1}$  to Castle Ridge Creek and  $2.5 \text{ cm d}^{-1}$  to the Machipongo River.

Delivery of nitrogen to these sites is largely a function of the groundwater source. If radon is delivered by terrestrial groundwater discharge it may include a high concentration of anthropogenic nitrate pollution. A mean of  $590 \text{ }\mu\text{M}$  nitrate was found in the surficial aquifer beneath agricultural fields on the Delmarva Peninsula by Hamilton and Helsel (1995). The removal of a portion of this nitrate enrichment would be expected en route to surface waters due to high rates of denitrification in lagoonal sediments (Anderson et al., 2003). If the excess radon is supplied to surface waters is from brackish or fully saline groundwater discharge, then much of the nitrogen may be recycled from the mineralization of marine- or marsh-derived organic matter. These recycled nutrients could cause the over-enrichment of nitrogen in surface waters nonetheless. The water column of North Inlet, South Carolina is enriched in nitrogen due to the discharge of fully saline groundwater that lies in a hydraulically conductive sand and shell aquifer beneath marsh platforms (Krest et al., 2000). That saline groundwater discharge contained average ammonium concentrations of  $77 \text{ }\mu\text{M}$ . With radium concentrations that correspond to radon activities of one-thirtieth those observed in the fresh and brackish groundwater surveyed in this study, the fully saline groundwater discharge rate could be

thirty times greater than the groundwater rates predicted in this study. This would imply a substantial role for marsh platforms and surficial aquifers beneath them in nitrogen cycling in these waters.

**Literature Cited**

- Anderson IC, McGlathery KJ, Tyler AC. 2003. Microbial mediation of 'reactive' nitrogen transformations in a temperate lagoon. *Marine Ecology Progress Series* 246:73–84.
- Burnett WC, Bokuniewicz H, Huettel M, Moore WS, Taniguchi M. 2003. Groundwater and pore water inputs to the coastal zone. *Biogeochemistry* 66:3–33.
- Burnett WC, Dulaiova H. 2003. Estimating the dynamics of groundwater input into the coastal zone via continuous radon-222 measurements. *Journal of environmental radioactivity* 69:21–35.
- Cable JE, Burnett WC, Chanton JP, Weatherly GL. 1996. Estimating groundwater discharge into the northeastern Gulf of Mexico using radon-222. *Earth and Planetary Science Letters* 144:591–604.
- Charette MA, Sholkovitz ER. 2006. Trace element cycling in a subterranean estuary: Part 2. Geochemistry of the pore water. *Geochimica et Cosmochimica Acta* 70:811–26.
- Cherkauer DS, Nader DC. 1989. Distribution of groundwater seepage to large surface-water bodies: The effect of hydraulic heterogeneities. *Journal of Hydrology* 109:151–65.
- Giblin AE, Gaines AG. 1999. Nitrogen inputs to a marine embayment: The importance of groundwater. *Biodegradation* 10:309–28.
- Hamilton PA, Helsel DR. 1995. Effects of Agriculture on Ground-Water Quality in Five Regions of the United States. *Ground Water* 33:217–26.

- Jähne B, Münnich KO, Börsinger R, Dutzi A, Huber W, Libner P. 1987. On the parameters influencing air-water gas exchange. *Journal of Geophysical Research: Oceans* (1978–2012) 92:1937–49.
- Johannes RE. 1980. Ecological significance of the submarine discharge of groundwater. *Marine Ecology Progress Series* 3:365–73.
- Krest JM, Moore WS, Gardner LR, Morris JT. 2000. Marsh nutrient export supplied by groundwater discharge: Evidence from radium measurements. *Global Biogeochemical Cycles* 14:167–76.
- Lambert MJ, Burnett WC. 2003. Submarine groundwater discharge estimates at a Florida coastal site based on continuous radon measurements. *Biogeochemistry* 66:55–73.
- Lawson SE, Wiberg PL, McGlathery KJ, Fugate DC. 2007. Wind-driven sediment suspension controls light availability in a shallow coastal lagoon. *Estuaries and Coasts* 30:102–12.
- Moore WS, Arnold R. 1996. Measurement of  $^{223}\text{Ra}$  and  $^{224}\text{Ra}$  in coastal waters using a delayed coincidence counter. *Journal of Geophysical Research: Oceans* (1978–2012) 101:1321–9.
- Paerl HW. 1997. Coastal eutrophication and harmful algal blooms: Importance of atmospheric deposition and groundwater as ‘new’ nitrogen and other nutrient sources. *Limnology and oceanography* 42:1154–65.
- Raymond PA, Cole JJ. 2001. Gas exchange in rivers and estuaries: Choosing a gas transfer velocity. *Estuaries and Coasts* 24:312–7.

- Reay WG, Gallagher DL, Simmons Jr GM. 1995. Sediment-water column oxygen and nutrient fluxes in nearshore environments of the lower Delmarva Peninsula, USA. *Marine Ecology Progress Series* 118.
- Taniguchi M, Burnett WC, Smith CF, Paulsen RJ, O'Rourke D, Krupa SL, Christoff JL. 2003. Spatial and temporal distributions of submarine groundwater discharge rates obtained from various types of seepage meters at a site in the Northeastern Gulf of Mexico. *Biogeochemistry* 66:35–53.
- Tyler AC, McGlathery KJ, Anderson IC. 2001. Macroalgae mediation of dissolved organic nitrogen fluxes in a temperate coastal lagoon. *Estuarine, Coastal and Shelf Science* 53:155–68.
- Valiela I, Costa J, Foreman K, Teal JM, Howes B, Aubrey D. 1999. Transport of groundwater-borne nutrients from watersheds and their effects on coastal waters. *Biodegradation* 10:177–97.



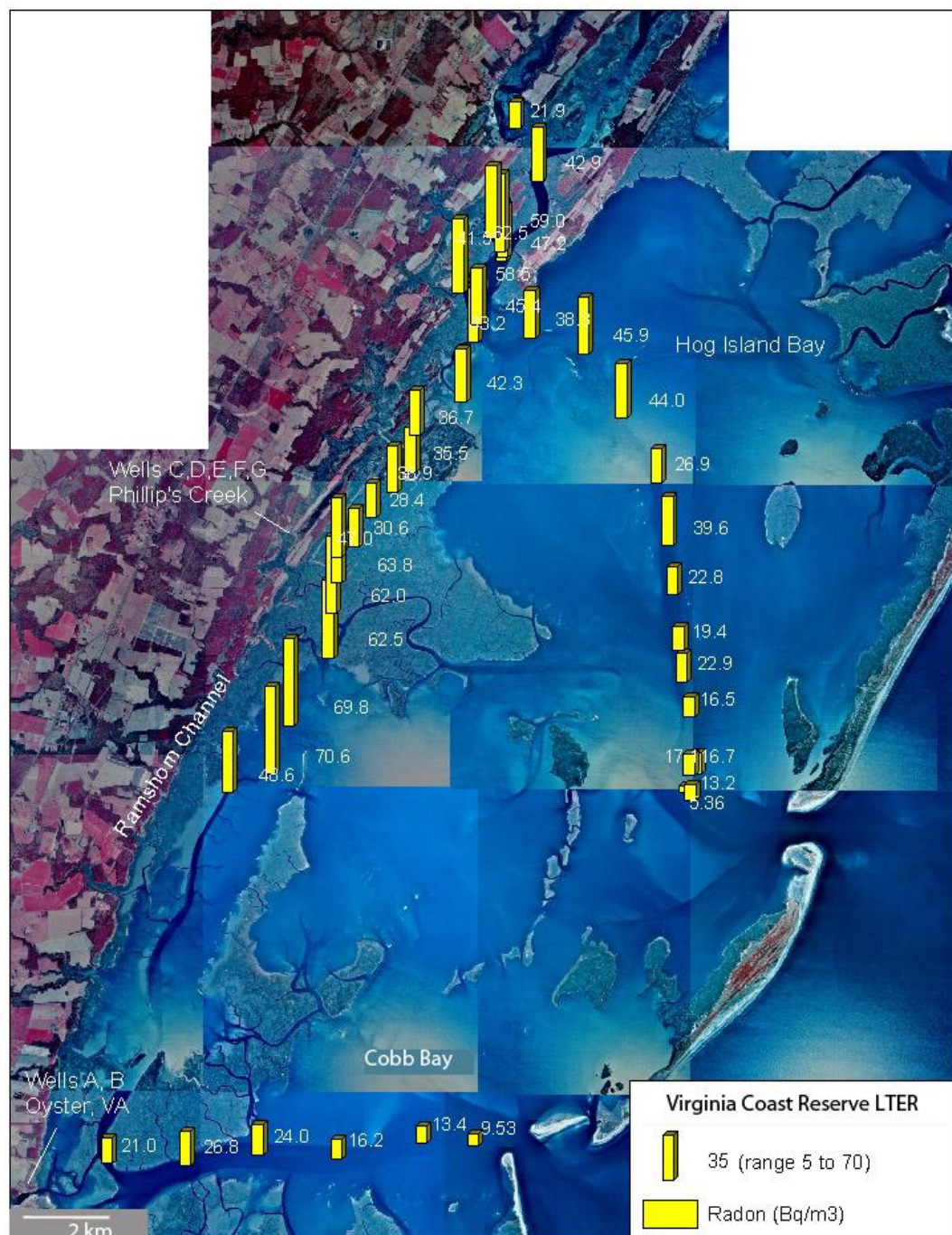


Figure 1: Radon in Hog Island Bay and Cobb Bay, VA. Data collection: Cobb Bay, March 12; Ramshorn Channel, March 13; Hog Island Bay, March 30, 2007. Radon in wells 3300 +/- 1600 Bq/m3.

## Appendix II

Groundwater Discharge to a Coastal Stream Determined from a Heat  
Balance: An Application of the Eddy Correlation Technique

## Overview

The eddy correlation technique has been used for decades to quantify land-atmosphere exchanges of energy, mass, and momentum (Baldocchi, 2003). The advantage of the technique in allowing continuous measurement of exchange under in situ conditions has led to the establishment and continuous operation of over 400 flux towers worldwide. The same in situ advantage of the technique for the measurement of land-atmosphere exchange applies to the underwater eddy correlation technique. Early underwater turbulent flux measurements were made for heat exchange beneath sea ice (McPhee, 1992). More recently, however, the coupling of acoustic Doppler velocimetry (Lohrmann et al., 1994), with fast-responding Clark-type oxygen micro-electrodes (Revsbech, 1986) allowed for the development and application of the eddy correlation technique to the measurement of oxygen fluxes in benthic environments (Berg et al., 2003).

Temperature may be used as a tracer of groundwater wherever a temperature gradient exists between the water column and sediments. As cold groundwater discharges from sediment into the water column turbulence rapidly mixes it into the surrounding water. High frequency measurement of the temperature and vertical water velocity at a location above the sediment surface would reveal the turbulent flux of groundwater (Figure 1), with positive instantaneous deviations in heat corresponding with negative deviations in vertical velocity, as warm overlying water is mixed towards the sediment surface. The mean of the product of these instantaneous deviations is the eddy flux.

## Methods

To determine the groundwater discharge rate an energy balance must be applied to the sediment-water column interface (Figure 2). Heat enters the control volume as groundwater,  $H_g$ , and advective transport due to currents, *inflow*. These inputs are balanced by the vertical eddy correlation of energy ( $H_{ec}$ ) through the top of the control volume, and by the advective horizontal flow of energy out of the control volume, *outflow*. Outflow equals inflow plus an additional energy flux out of the control volume ( $H_a$ ) due to displacement of water out of the control volume by groundwater. This energy balance, presented by Crusius et al., (2008) gives the instantaneous groundwater specific discharge ( $q_g$ ),

$$q_g = \frac{\overline{u'_z T'_s} C_p \rho_s}{\rho_g (\overline{T_g} C_{p_g} - \overline{T_s} C_{p_s})} \quad (1)$$

where  $u'_z$  is the fluctuating vertical velocity,  $T'$  is the fluctuating temperature, over bars indicate the mean value,  $C_p$  is the specific heat, and  $\rho$  is density. The subscripts s and g refer to surface water and groundwater respectively. For details on eddy correlation ( $\overline{u'_z T'_s}$ ) measurements, see Berg et al. (2003). A similar balance can be performed to calculate groundwater discharge from the eddy flux of salt.

## Observations and Discussion

The eddy correlation system was deployed in freshwater creeks, beaches, and tidal creeks to calculate groundwater discharge from the measured eddy flux. Each of these

environments posed unique challenges for quantifying groundwater discharge, but for the focus of this appendix is on the sites where the most deployments were made, in freshwater creeks of the VCR-LTER. In September and October of 2009 and 2010 the eddy correlation system was deployed in Frogstool Branch, near Quinby, VA. Frogstool Branch is a small, sand-bed creek, with a base-flow discharge of approximately 5 liters  $\text{s}^{-1}$ . Diurnal temperature changes in Frogstool Branch were on the order of  $3^{\circ}\text{C}$ , and were driven by diurnal air temperature changes of twice that magnitude or more. This diurnal variation in stream temperature propagated deeply into stream bed sediments, with sediments at a depth of 30 cm varying in temperature by  $0.17^{\circ}\text{C}$  in 10 hours (Figure 3). Due to the depth of diurnal temperature fluctuation, the change in heat stored in stream bed sediments over time was substantial.

To determine groundwater discharge rates through stream beds a notional control volume across the sediment-water interface was developed for mass and energy. Optimal conditions for detecting groundwater discharge by a heat balance are presented in Figure 4. Two millimeters of rain had fallen in the Frogstool watershed in two hours. For forty-eight hours after the rainfall, heat fluxes through the stream bed were consistently positive. Thirty-two of these hours are presented in Figure 4. The heat fluxes appeared to respond to slight fluctuation in the combined atmospheric and hydrostatic pressure recorded by a pressure transducer in the stream, with a maximum heat flux co-occurring with a dip in the pressure. However, the control volume energy balance at the peak of the heat flux (hour 231 to 231.25) failed to close. The eddy flux of heat from the stream bed was  $19.1 \text{ W m}^{-2}$ , yet conduction through the bottom of the control volume added  $12.3 \text{ W}$

$\text{m}^{-2}$  of heat to a source of  $11.9 \text{ W m}^{-2}$  in sediment and an additional source of  $14.3 \text{ W m}^{-2}$  in overlying water.

While the quality and sensitivity of the measurements of heat flux by eddy correlation indicated that the calculated fluxes were real, a large portion of the energy budget that was poorly constrained in these experiments was heat conduction. The  $11.9 \text{ W m}^{-2}$  of heat released by sediments in the control volume was generated by a drop in sediment temperature of  $0.024^\circ\text{C}$ . Fifteen centimeters away from this temperature profile the stream bed temperatures at 5 cm depth were  $0.1^\circ\text{C}$  warmer, and may have exhibited less temperature change with depth.

The hydraulic conductivities of streambed sediments permit significant interaction between overlying water and pore water as well as allowing for lateral transport of groundwater and pore water. Huettel et al., 1996 in flume studies of the flow of water over medium grained sandy sediment (comparable to the bed of Frogstool Branch) observed the entrainment of overlying water in sediment pore waters to a depth of 4.5 cm in 16.5 hours. With horizontal hydraulic conductivities often 3 to 4 times in excess of vertical hydraulic conductivities in streambed sediments (Chen, 2000) it is likely that there is substantial vertical and lateral transfer of heat in these sediments along hyporheic flow paths.

To incorporate the large diurnal fluctuation in heat conduction into the energy balance, a model of heat conduction over time would be advantageous. A growing body of research has demonstrated that temperature gradients in aquatic sediments can be used not only to locate sites of groundwater discharge, but also to quantify the rate from the

shape of the equilibrium temperature profile in sediments (Stallman, 1965). More recent methods have examined diurnally fluctuating sediment temperature profiles and used the rate and direction of heat propagation to quantify groundwater discharge rates (e.g., Keery et al., 2007).

### Literature Cited

- Baldocchi, D. 2003, Assessing the eddy covariance technique for evaluating carbon dioxide exchange rates of ecosystems: past, present and future, *Global Change Biology*, 9, 479-492.
- Berg, P., H. Roy, F. Janssen, V. Meyer, B. B. Jorgensen, M. Huettel, and D. de Beer 2003, Oxygen uptake by aquatic sediments measured with a novel non-invasive eddy correlation technique, *Mar. Ecol. Prog. Ser.*, 261, 75-83.
- Chen, X. 2000. Measurement of streambed hydraulic conductivity and its anisotropy. *Environmental Geology* 39:1317–24.
- Crusius, J., P. Berg, D. J. Koopmans, and L. Erban. 2008. Eddy correlation measurements of submarine groundwater discharge, *Mar. Chem.*, 109, 77-85, doi:10.1016/j.marchem.2007.12.004.
- Huettel, M., W. Ziebis, S. Forster, and G. W. Luther III. 1998. Advective transport affecting metal and nutrient distributions and interfacial fluxes in permeable sediments. *Geochim. Cosmochim. Acta*, 62, 613-631.
- Keery, J., A. Binley, N. Crook, J. W. N. Smith. 2007. Temporal and spatial variability of groundwater-surface water fluxes: development and application of an analytical method using temperature time series, *J. Hydrol.* 336, 1 – 16.
- Lohrmann, A., R. Cabrera, and N. C. Kraus. 1994. Acoustic Doppler velocimeter (ADV) for laboratory use. *Fundamentals and Advancements in Hydraulic Measurements and Experimentation Proceedings*. August 1 – 5, Buffalo, NY.



- McPhee, M. G. 1992. Turbulent heat flux in the upper ocean under sea ice. *J. Geophys. Res.* 97, 5365-5379.
- Revsbech, N. P. 1986. An oxygen microsensor with a guard cathode. *Limnol. Oceanogr.* 34, 474-478.
- Stallman, R. W. 1965. Steady one-dimensional fluid flow in a semi-infinite porous medium with sinusoidal surface temperature, *J. Geophys. Res.* 70, 2821-2827.
- Stanhope, J. W., I. C. Anderson, and W. G. Reay. 2009. Base flow nutrient discharge from lower Delmarva Peninsula watersheds of Virginia, USA. *J. Environ. Qual.* 38, 2070-2083.
- Tyler, A. C., K. J. McGlathery, and I. C. Anderson. 2003. Benthic algae control sediment-water column fluxes of organic and inorganic nitrogen compounds in a temperate lagoon, *Limnol. Oceanogr.* 48, 2125-2137.

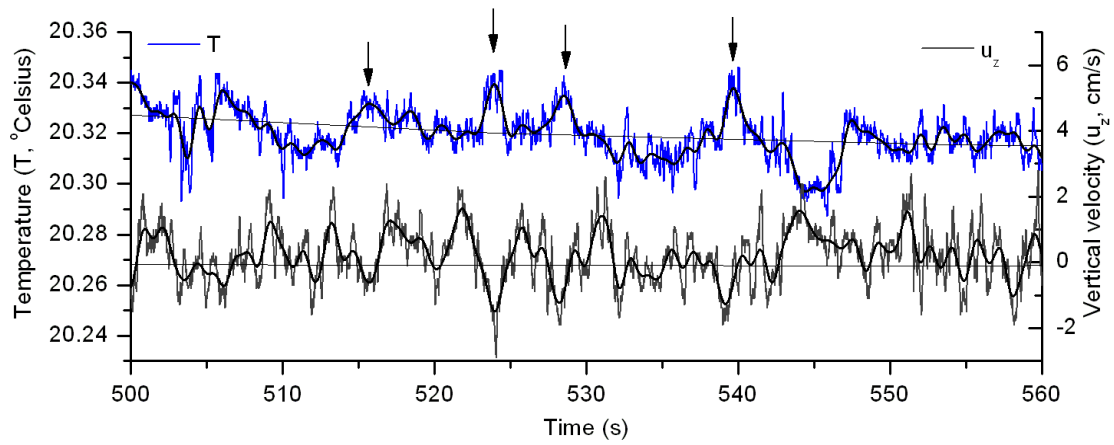


Figure 1. Instantaneous deviations in temperature (top) and vertical velocity (bottom) corresponding to a negative heat flux. Arrows indicate times at which temperature deviates positively from the mean and velocity deviates negatively, resulting in a downward heat flux.

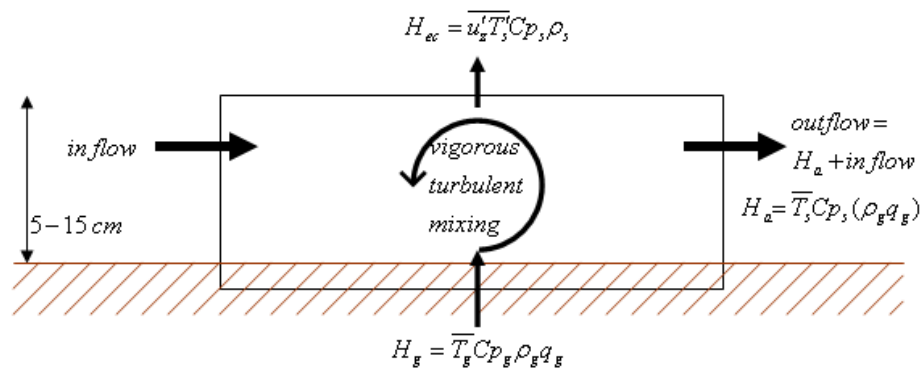


Figure 2. The heat balance across the sediment-water interface that was formulated to calculate the rate of groundwater discharge. The symbol definitions are in the text.

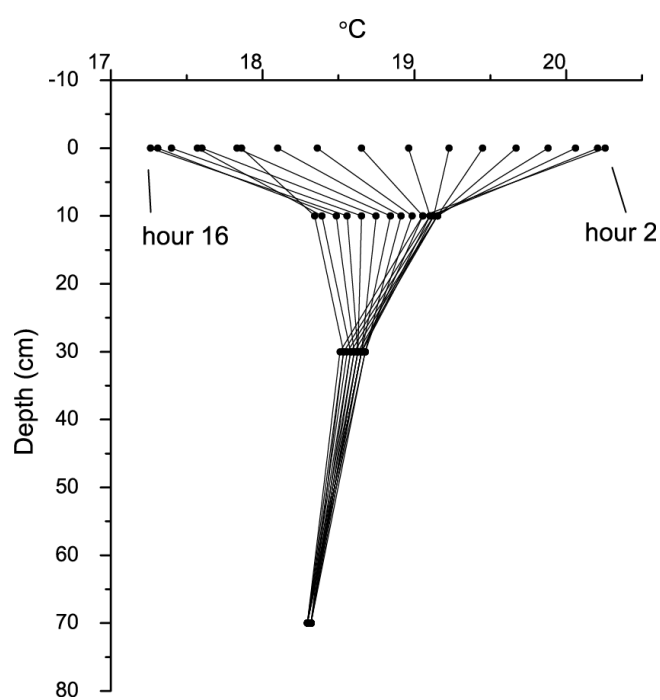


Figure 3. The diurnal temperature fluctuation in stream bed sediments of Frogstool Branch.

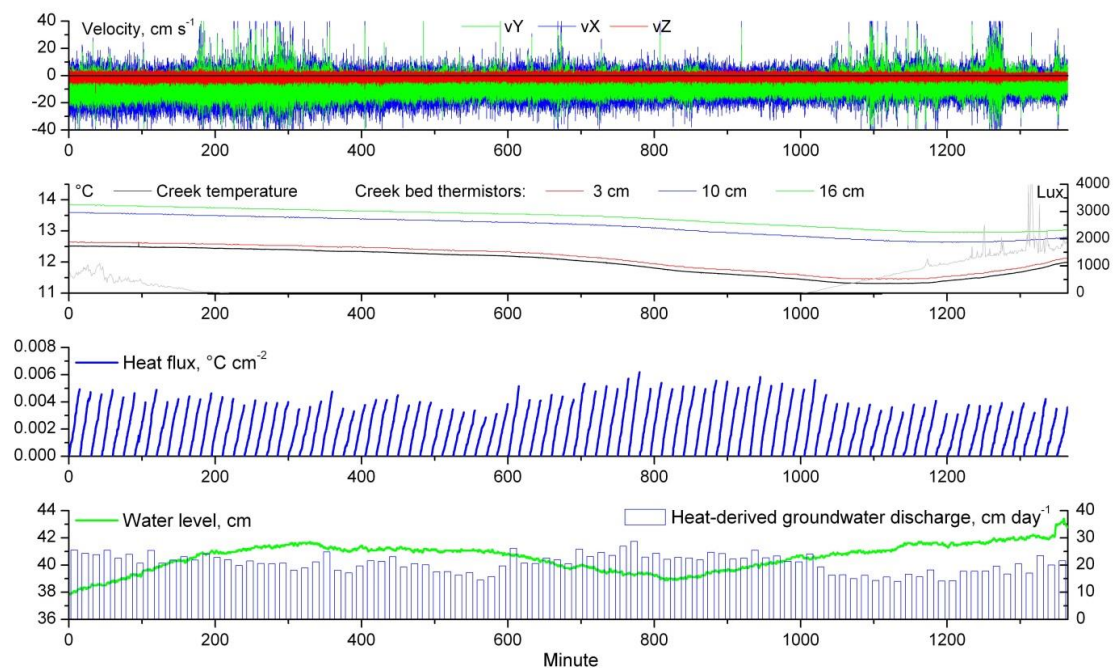


Figure 4. **A** Rainfall caused an increase in Frogstool Branch stream velocity in October of 2009. **B** Temperatures within sediments were higher than those in the stream. **C** Cumulative fluxes calculated from the instantaneous deviation of vertical velocity and temperature were positive, corresponding with expected fluxes due to the discharge of warmer groundwater into colder overlying waters. **D** From the heat flux the rate of groundwater discharge was calculated.

## Appendix III

### Oxygen Exchange and Ice Melt Measured at the Ice-Water Interface by Eddy Correlation

Long<sup>1</sup>, M.H, D. Koopmans<sup>1</sup>, P. Berg<sup>1</sup>, S. Rysgaard<sup>2,3</sup>, R.N. Glud<sup>2,4,5</sup>, and D.H. Sørensen<sup>2,5</sup>

Published in the journal *Biogeosciences*

2012, V. 9

doi: 10.5194/bg-9-1957-2012

<sup>1</sup> Department of Environmental Sciences, University of Virginia, Charlottesville, Virginia

<sup>2</sup> Greenland Climate Research Centre, Greenland Institute of Natural Resources, Nuuk, Greenland.

<sup>3</sup> Centre for Earth Observation Science, CHR Faculty of Environment Earth and Resources, University of Manitoba, Winnipeg, Canada

<sup>4</sup> Scottish Association of Marine Sciences, Oban, Scotland, UK

<sup>5</sup> Southern Danish University and NordCee, Odense M, Denmark

Correspondence to: P. Berg (pb8n@virginia.edu)

**Attribution**

The following chapter was the product of a close collaboration between the first author, Matthew Long, our advisor, Peter Berg, two principle investigators with the Greenland Institute of Natural Resources and other institutions Soeren Rysgaard and Ronnie Glud, and a Scientist & Ph.D. Student advised by Soeren, Dorte Sogaard. The goal of the project was to quantify the respective contribution of physical and biological processes to oxygen production and consumption beneath sea ice as these may reflect a significant component of the regional carbon balance. In order to accomplish that goal field research was conducted from a research vessel in a remote fjord on the western coast of Greenland, and so extensive material and personnel support were required.

Soeren Rysgaard and Ronnie Glud were the lead investigators for the project. The supporting personnel included Dorte Sogaard who quantified rates of gross primary production under sea ice using an independent method. Soeren and Ronnie were involved in oxygen and heat flux measurements and analysis day-to-day at the field site. Matthew Long and I were responsible for determining oxygen fluxes and heat fluxes beneath the sea ice, respectively. Matt used the oxygen flux data to determine the metabolic response of the algal community beneath the sea ice to light, while from heat fluxes I calculated the corollary rates at which sea would ice melt. Once the rate of ice melt had been quantified the proportion of oxygen flux due to biological processes could be determined. Our advisor, Peter Berg, conducted the extensive hydrodynamic interpretation and analyses required. Matt Long was the principle author of the manuscript.

## Abstract

This study examined fluxes across the ice-water interface utilizing the eddy correlation technique. Temperature eddy correlation systems were used to determine rates of ice melting and freezing, and O<sub>2</sub> eddy correlation systems were used to examine O<sub>2</sub> exchange rates driven by biological and physical processes. The study was conducted below 0.7 m thick sea-ice in mid-March 2010 in a southwest Greenland fjord and revealed low rates of ice melt at a maximum of 0.80 mm d<sup>-1</sup>. The O<sub>2</sub> flux associated with release of O<sub>2</sub> depleted melt water was less than 13% of the average daily O<sub>2</sub> respiration rate. Ice melt and insufficient vertical turbulent mixing due to low current velocities caused periodic stratification immediately below the ice. This prevented the determination of fluxes 61% of the deployment time. These time intervals were identified by examining the velocity and the linearity and stability of the cumulative flux. The examination of unstratified conditions through vertical velocity and O<sub>2</sub> spectra and their cospectra revealed characteristic fingerprints of well-developed turbulence. From the measured O<sub>2</sub> fluxes a photosynthesis/irradiance curve was established by least-squares fitting. This relation showed that light limitation of net photosynthesis began at 4.2 μmol photons m<sup>-2</sup> s<sup>-1</sup>, and that algal communities were well-adapted to low-light conditions as they were light saturated for 75% of the day during this early spring period. However, the sea-ice associated microbial and algal community was net heterotrophic with a daily gross primary production of 0.69 mmol O<sub>2</sub> m<sup>-2</sup> d<sup>-1</sup> and a respiration rate of -2.13 mmol O<sub>2</sub> m<sup>-2</sup> d<sup>-1</sup> leading to a net ecosystem metabolism of -1.45 mmol O<sub>2</sub> m<sup>-2</sup> d<sup>-1</sup>. This application of the eddy correlation technique produced high temporal resolution O<sub>2</sub> fluxes and ice melt



rates that were measured without disturbing the in situ environmental conditions while integrating over an area of approximately 50 m<sup>2</sup> which incorporated the highly variable activity and spatial distributions of sea-ice communities.

## **Introduction**

Sea-ice associated microbial communities can be an important component of marine polar food webs (Arrigo 2003) and when sea-ice is present it can host 30-65 % of the ecosystem primary production (e.g. Mikkelsen et al. 2008, McMinn et al. 2010). Primary production and phototrophic growth in sea-ice is largely limited by the amount of light that transmits through the ice and snow cover (Arrigo 2003, McMinn et al. 2010). Therefore production is tightly linked to photosynthetic efficiency, with sea-ice algae being well-adapted to low light conditions (Mock and Gradinger 1999, Kuhl et al. 2001, Rysgaard et al. 2008). Oxygen (O<sub>2</sub>) fluxes are commonly used to determine photosynthetic production and respiration in aquatic ecosystems, however at the ice-water interface such measurements are complicated by an additional O<sub>2</sub> flux contribution driven by the physical processes of melting and freezing (Glud et al. 2002). Specifically, sea-ice formation can cause a release of O<sub>2</sub> supersaturated brines, while sea-ice melt can generate a release of O<sub>2</sub> undersaturated melt water (Glud et al. 2002, Rysgaard et al. 2008), confounding measurements of primary production and respiration during periods of rapid freeze or melt. Therefore, to estimate the biotic O<sub>2</sub> flux it is necessary to quantify the physical contribution from freezing and melting.

Sampling at the ice-water interface presents a number of challenges for traditional techniques for quantifying primary production and respiration. The techniques presently used to study sea-ice primary production sample at either one point on the ice surface or within an ice core, though algal patchiness and activity have been reported to vary across a much wider range (Gosselin et al. 1986, Rysgaard et al. 2001). This may lead to misrepresentation of the actual sea-ice environment and requires that many replicates are taken over a large area. A further limitation of conventional methods is their poor resolution of temporal variation, which has limited the studies of short-term variations in production and respiration in sea-ice microbial communities. The  $^{14}\text{C}$  tracer method and  $^3\text{H}$  labeled thymidine approach are the most widely applied techniques to determine primary production and bacterial production in sea-ice, respectively. However, both methods are time consuming, making multiple samples and a wide spatial coverage difficult (McMinn and Ashworth 1998, Sørensen et al. 2010). Both approaches also require melting the ice to evenly distribute the tracers, which grossly changes the natural conditions experienced by the microalgae and bacteria (e.g. nutrient levels, light, and  $\text{O}_2$  gradients) (Glud et al. 2002, Rysgaard et al. 2008).

Pulse amplitude modulated (PAM) fluorometry represents a promising alternative to study the primary production of natural communities. However, when PAM is applied to intact ice cores the depth integrated signal is poorly defined and depends on variations in algae biomass as well as the optical properties of the ice (Rysgaard et al. 2001, Glud et al. 2002). The conversion of PAM data into carbon (or  $\text{O}_2$ ) fluxes further complicates the method as frequent intercalibration to poorly constrained empirical relationships are

required. Microsensor profiling using both Clark-type O<sub>2</sub> microsensors and O<sub>2</sub> micro-optodes has also been used to examine ice-water O<sub>2</sub> fluxes but can suffer from calibration problems due to temperature and salinity gradients and spatial micro-variability in the ice (McMinn and Ashworth 1998, Glud et al. 2002, Mock et al. 2003, McMinn et al. 2007).

Eddy correlation in aquatic environments is a technique typically used for measuring fluxes across the sediment-water interface by correlating high temporal resolution measurements of velocity and a scalar quantity of interest (Berg et al. 2003). Oxygen eddy correlation systems have been used to determine photosynthesis and respiration in muddy marine benthic systems and river bottoms (Berg et al. 2003), sandy sediments (Kuwae et al. 2006, Berg and Huettel 2008, Reimers et al. 2012), the deep ocean (Berg et al. 2009), lakes (Brand et al. 2008, McGinnis et al. 2008, Lorrai et al. 2010), hard-bottom arctic substrates (Glud et al. 2010), and seagrass beds (Hume et al. 2011). With the eddy correlation technique measurements are conducted under true in situ conditions, i.e. without disturbing the surface and under natural light and hydrodynamic conditions (Berg et al. 2003). The technique also integrates over a large surface area, typically tens of meters long and a few meters wide (Berg et al. 2007). For these reasons, the technique is ideal for applications under sea-ice allowing fluxes across the ice-water interface to be examined non-invasively. The eddy correlation technique has been used to determine fluxes of momentum, heat, and salt beneath sea-ice (McPhee 1992, Shirasawa et al. 1997, Widell et al. 2006, MCPhee et al. 2008) but has not previously been used to quantify O<sub>2</sub> exchange and thereby production and respiration of sea-ice microbial communities. In this study we present results obtained with O<sub>2</sub> eddy

correlation systems and temperature eddy correlation systems that are used collectively to determine true in situ O<sub>2</sub> exchange rates and thereby non-invasively determine the primary production and respiration of sea-ice algal communities.

## Methods

### *Site Description*

Measurements were performed in a small tributary fjord near Kapisigdlit, Greenland from 12-17 March, 2010. The sub-Arctic fjord is located in southwest Greenland and is part of the Nuup Kangerlua Fjord. The fjord was partially covered with ice at a thickness of ~70 cm and a snow cover of ~2 cm during the sampling period. Measurements were conducted 100 m from the ice edge. Air temperatures during the study period ranged from -8.8 °C to +2.9 °C with an average temperature of -3.2 °C. Water depth at the deployment location varied between 40 and 45 m. The concentration of chlorophyll *a* in the bottom 12 cm of ice was  $2.8 \pm 0.4 \mu\text{g L}^{-1}$  (SE,  $n = 3$ ) and the average concentration across the entire ice thickness was  $1.0 \pm 1.2 \mu\text{g L}^{-1}$  (SE,  $n = 3$ ).

### *Eddy Correlation Measurements*

Two O<sub>2</sub> eddy correlation systems and two temperature eddy correlation systems were deployed beneath the ice. The O<sub>2</sub> eddy correlation system consists of an acoustic Doppler Velocimeter (ADV) (Nortek AS, Norway) that has been modified to record measurements made with a high-resolution custom-made pA amplifier (Max Planck

Institute for Marine Microbiology, Germany) to which a fast responding ( $< 0.2$  sec) Clark-type  $O_2$  microsensor is mounted (Berg and Huettel 2008, Berg et al. 2009, Hume et al. 2011). The temperature eddy correlation system consists of a standard ADV coupled to a rapid-response ( $< 0.1$  sec) temperature and conductivity sensor (Fast CT sensor, Precision Measurement Engineering, USA) (Crusius et al. 2008). Damage to the conductivity sensors prevented simultaneous measurement of the salt flux.

The systems were positioned under the sea-ice by lowering them through a 0.25 by 0.60 m rectangular hole (Fig. 1). This new deployment tactic, compared to traditional tripod mounted systems, was very simple and did not require any diver support. The ADV and scalar sensors were mounted to a stainless steel T rod with the sensors positioned at the edge of the ADV's  $\sim 1 \text{ cm}^3$  measuring volume that was located 22 cm below the ice-water interface. Water velocity ( $x$ ,  $y$ , and  $z$  components), time,  $O_2$  concentration and temperature were recorded by the ADVs at a frequency of 64 Hz in intervals of 0.25 h. Total measurement periods were typically 24 h long to capture diurnal fluctuations. An  $O_2$  optode (Hach, USA) measured the mean  $O_2$  concentration as a calibration check of the Clark-type  $O_2$  microsensors. Photosynthetically active radiation (PAR) was determined using a self-contained cosine-corrected integrating PAR logger (Odyssey, New Zealand) which was deployed just below the ice-water interface.

### *Data Analysis*

Fluxes of  $O_2$  and heat across the ice-water interface were calculated from high resolution measurements of the vertical velocity and either the  $O_2$  concentration or temperature as:

$$\overline{Flux} = \overline{u'_z C'} \quad (1)$$

where  $u'_z$  is the instantaneous fluctuating component of the vertical velocity,  $C'$  is the instantaneous fluctuating component of the O<sub>2</sub> concentration or temperature, and the bars symbolize averaging over time (Berg et al. 2003). The fluctuating components were separated from the means by Reynolds Decomposition as  $u'_z = u_z - \overline{u_z}$  and  $C' = C - \overline{C}$  where  $u_z$  and  $C$  are the instantaneous measurements, and the means ( $\overline{u_z}$  and  $\overline{C}$ ) were determined by linear least squares fits (linear detrending) over each 0.25 h measuring period (Berg et al. 2009). The three-dimensional velocity field was rotated to orient the  $x$ -axis into the mean flow direction and to bring the mean perpendicular and vertical velocities to zero to correct for any sensor tilt. The O<sub>2</sub> concentration, temperature, and velocities in each burst were examined carefully for anomalous variations due to sensor malfunctions caused by disturbances of the sensors, for example due to debris floating in the water. Furthermore, the mean current velocity, the cumulative flux (O<sub>2</sub> or heat), the spectra (vertical velocity and heat or O<sub>2</sub> concentration), and the cospectra (vertical velocity vs. heat or O<sub>2</sub> concentration) were used to identify periods with well-developed turbulence under the ice where trustworthy eddy fluxes could be determined (see results and discussion).

The rate of ice melt ( $h$ ) was calculated from the temperature flux (Eq. 1) as:

$$h = \frac{\overline{u'_z T'} c_{pw} \rho_w}{\Delta H_f \rho_i} \quad (2)$$

where  $c_{pw}$  is the specific heat capacity of seawater,  $\rho_w$  is the density of seawater,  $\Delta H_f$  is the specific heat of fusion of ice, and  $\rho_i$  is the density of the ice. The numerator of Eq. 2 constitutes the heat flux. For the purposes of this first order calculation of the melt rate we assumed the conduction of heat up through the ice was negligible. This assumption makes the calculated rates represent an upper limit for ice melt. Furthermore, due to the difficulty in determining the  $O_2$  concentration of the melt water, an  $O_2$  flux due to ice melt was determined with the assumption that the melt water from sea-ice was anoxic. This also results in an overestimate of the  $O_2$  flux due to ice melt as bulk ice  $O_2$  concentrations were found to range between 40 and 280  $\mu\text{mol L}^{-1}$  at a bulk salinity of 4.6 during the campaign (Tison et al. unpublished data).

Assuming a small, constant contribution of ice melt to the total  $O_2$  exchange rate, a constant respiration rate, and that  $O_2$  metabolism occurs predominantly at the ice-water interface, simple relationships between measured  $O_2$  fluxes, rates of  $O_2$  production ( $P$ ) and respiration ( $R$ ), and the irradiance were developed:

$$\overline{O_2 \text{ flux}} = P - R \quad (3)$$

$$P = P_0 (1 - e^{(-I/I_k)}) \quad (4)$$

where  $P_0$  is the maximum primary production rate in the photosynthesis to irradiance (P/I) curve for sea-ice algae,  $I$  is irradiance and  $I_k$  is the photoadaptation parameter or the irradiance level at which photosynthesizing organisms begin to become saturated with light (Platt et al. 1980, Smith et al. 1988, Suzuki et al. 1997).

## Results

During periods of low current flow, vertical turbulent mixing was not consistently adequate to prevent density stratification from forming immediately below the ice. However, well-developed turbulence was generally found at current velocities greater than  $1 - 2 \text{ cm s}^{-1}$ . Figure 2 shows an example of how current velocity changed the turbulent transport and mixing under ice. At low current velocities there was little or no vertical mixing, which resulted in the formation of density stratification. As the velocity increased there was a point when this stratification was eroded and allowed the water column immediately below the ice to be mixed. The onset of mixing events were evident in large  $\text{O}_2$  and temperature fluctuations and were not used in the flux calculations because of the incompatibility with linear detrending over these periods with widely fluctuating  $\text{O}_2$  and temperature signals. Furthermore, the mixing of the stratified layer was not indicative of the actual flux at that point in time, and the period leading up to this integrated signal is poorly constrained. The erosion of stratification was followed by periods of stable and linear cumulative flux signals that were suitable for flux determination. Finally, as the velocity and associated turbulence decreased, the stratification was re-established. Stratification prevented the determination of fluxes approximately 61% of the total deployment time.

Stratified conditions were identified by examining the current velocity and the corresponding flux signal. Under low flow conditions the cumulative flux became highly nonlinear and erratic, indicating a weak flux signal. Under high flow conditions a consistent and linear trend in the cumulative flux indicated a strong flux signal. Well-



mixed conditions where fluxes could be accurately determined were found 26% of the time. Due to broken or malfunctioning sensors, fluxes were not determined during the remaining 13% of the time despite likely turbulent conditions (i.e. velocity  $> 2 \text{ cm s}^{-1}$ ). Unstratified conditions were further examined in the frequency domain through the vertical velocity spectrum, where fully developed turbulence was indicated by a characteristic  $-5/3$  slope (Fig. 3A)( Kundu and Cohen 2008). Similarly the  $\text{O}_2$  spectrum shows an initial  $-5/3$  slope at lower frequencies and the expected  $-1$  slope at higher frequencies where viscous forces gain importance (Fig. 3B)(Kundu and Cohen 2008). The normalized cumulative cospectrum of the vertical velocity and  $\text{O}_2$  concentration (Fig. 3C) also shows the typical fingerprint of turbulent transport where eddies with frequencies less than 0.1 Hz dominate the vertical turbulent transport of  $\text{O}_2$ . Under well-mixed conditions the fluxes of  $\text{O}_2$  and heat were highly reproducible. For example, Figure 4 shows a typical example of  $\text{O}_2$  eddy correlation data at night over 2.5 h, with an average flux of  $-2.99 \pm 0.26 \text{ mmol m}^{-2} \text{ d}^{-1}$  (SE,  $n = 10$ ) where a negative flux is a net flux of  $\text{O}_2$  towards the ice. The consistent and linear cumulative fluxes indicate a strong flux signal (Fig. 4C).

All trustworthy mean  $\text{O}_2$  fluxes for the entire study period are shown in Fig. 5. The smallest net  $\text{O}_2$  flux towards the ice occurred during peak irradiance. No correlation between current direction and the  $\text{O}_2$  flux was found ( $R^2 = 0.021$ ,  $p = 0.816$ ,  $n = 123$ ). The white circles in Fig. 5A are the model results determined by simultaneously fitting Eq. 3 and 4 ( $R^2 = 0.923$ ) to the mean fluxes as described below.

The P/I curve (Eq. 3) resulted from the fitting of the eddy correlation data in Figure 5, with  $R$  being the average  $O_2$  flux in the dark ( $R^2 = 0.923$ , Fig. 6). The maximum  $P$  rate was  $1.76 \pm 0.27 \text{ mmol } O_2 \text{ m}^{-2} \text{ d}^{-1}$  (SE,  $n = 8$ ) and  $I_k$  was  $4.2 \text{ } \mu\text{mol photons m}^{-2} \text{ s}^{-1}$  (based on irradiance measured just below the ice-water interface). Using Eq. 3 and 4 and the measured light values, 0.25 h  $O_2$  exchange rates were calculated across 4 days of the study period (Fig. 7). From these model results the daily values of  $R$ , gross primary production (GPP), and net ecosystem metabolism (NEM) were calculated with the rates weighted by the hours of daylight and darkness and assuming that respiration was the same day and night. This resulted in a value of  $R$  of  $-2.13 \text{ mmol } O_2 \text{ m}^{-2} \text{ d}^{-1}$  while GPP averaged  $0.69 \pm 0.02 \text{ mmol } O_2 \text{ m}^{-2} \text{ d}^{-1}$  (SE,  $n = 4$ ), and NEM averaged  $-1.45 \pm 0.02 \text{ mmol } O_2 \text{ m}^{-2} \text{ d}^{-1}$  (SE,  $n = 4$ ). Light saturation (based on  $I_k$ ) occurred at an average of  $1.47 \pm 0.09 \text{ h}$  (SE,  $n = 8$ ) after first light and before darkness. With an average day length of  $11.69 \pm 0.24 \text{ h}$  (SE,  $n = 4$ ) the bottom ice algal communities were therefore light saturated for 75 % of the day.

The mean heat flux was  $2.83 \pm 0.30 \text{ W m}^{-2}$  (SE,  $n = 31$ ), giving a calculated rate of ice melt (Eq. 2) of  $0.80 \pm 0.09 \text{ mm d}^{-1}$  (SE,  $n = 31$ ). The mean observed temperature of seawater during the measuring period was  $-0.05 \text{ }^\circ\text{C}$  and the salinity 33. The specific heat capacity of the seawater was assumed to be  $3.999 \text{ J g}^{-1} \text{ }^\circ\text{C}^{-1}$  and the density was assumed to be  $1.026 \text{ g cm}^{-3}$  (Fofonoff and Millard 1983). In our first-order calculation of melting rates we assumed that the entire heat flux towards the sea-ice was used to melt pure ice, and thus, neglected any portion of the flux that might have been lost by heat conduction up into the ice interior. As explained above, this leads to an overestimation of

the ice melt rate and of the O<sub>2</sub> flux associated with it. Based on this assumption we used a heat of fusion for pure ice of 333.6 J g<sup>-1</sup> (Harvey 2010) and a density of ice of 0.917 g cm<sup>-3</sup> (Eicken 2003). The average ice melt rates shown in Figure 8 varies from  $0.49 \pm 0.11$  (SE,  $n = 6$ ) to  $0.99 \pm 0.25$  mm d<sup>-1</sup> (SE,  $n = 8$ ). The ice melt rates were not significantly different between each period ( $F_4 = 2.040$ ,  $p = 0.111$  at 0.01 level). There were no correlations between the observed 0.25 h heat fluxes and velocity ( $R^2 = 0.002$ ,  $p = 0.833$ ), temperature ( $R^2 = 0.022$ ,  $p = 0.450$ ), light ( $R^2 = 0.016$ ,  $p = 0.492$ ), or current direction ( $R^2 = 0.001$ ,  $p = 0.866$ ). The O<sub>2</sub> flux that was calculated based on the ice melt rates, through the melting of de-oxygenated ice, averaged  $-0.28 \pm 0.03$  mmol O<sub>2</sub> m<sup>-2</sup> d<sup>-1</sup> (SE,  $n = 31$ ). This flux amounts to less than 13 % of the daily  $R$  rate derived from fitting Eq. 3 and 4 to the data in Fig. 5.

The footprint, or the area of the ice surface that contributes 90 % of the measured flux (Fig. 9), was calculated from estimated values of the friction velocity ( $u^*$ ), the surface roughness ( $z_o$ ), and the measuring height as described by Berg et al. (2007). This first order calculation revealed a value of  $u^*$  of  $0.098 \pm 0.007$  cm s<sup>-1</sup> (SE,  $n = 20$ ) and a hydraulically smooth ice surface with a  $z_o$  of  $0.023 \pm 0.002$  cm (SE,  $n = 20$ ) (see Berg et al. 2007 for details). The oval shaped footprint was about 2.8 m wide by 67 m long with a point of maximum flux contribution at 3.2 m upstream from the eddy correlation instrument (Fig. 9).

The level of anisotropy in the turbulent flow below the sea-ice, as reflected in the ratios between the eddy diffusivities ( $E_x$ ,  $E_y$ , and  $E_z$ ) in the  $x$ ,  $y$ , and  $z$  directions, was

estimated as described by Berg et al. (2007) (Fig. 10). Anisotropy was clearly evident ( $E_x/E_z = 6.2 \pm 1.0$ ,  $E_y/E_z = 3.8 \pm 0.5$ ,  $E_z/E_z = 1 \pm 0.0$ ; SE,  $n = 5$ ).

## Discussion

The eddy correlation technique is in many respects superior to traditional flux methods (Berg et al. 2003, Kuwae et al. 2006, Berg and Huettel 2008) and this study conducted at the ice-water interface further exhibits the adaptability and advantages of the technique. The first measurements of O<sub>2</sub> eddy correlation fluxes at the ice-water interface presented here are controlled by ice melt, and to a much larger extent, the biological activity of the microbial communities. However, the ice-water interface also produces conditions that must be addressed when sampling eddy correlation ice-water fluxes such as low current velocities, density stratifications, and instrument deployment. Despite this, the eddy correlation technique is well suited for flux measurements at the ice-water interface and has previously been applied and validated for momentum, heat, and salt fluxes (McPhee 1992, Shirasawa et al. 1997, Widell et al. 2006, MCPhee et al. 2008).

Measured O<sub>2</sub> exchange rates across the ice-water interface do not directly represent primary production and respiration, as physical processes may also contribute to the exchange during periods of rapid freezing or melting. These physical processes include the release of O<sub>2</sub> supersaturated brine during freezing or the release of O<sub>2</sub> undersaturated water during melting (Glud et al. 2002, Rysgaard et al. 2008). Although these physical processes only contributed a minor portion of the total O<sub>2</sub> flux in this study due to very low melt rates, this will not always be the case. Heat fluxes can be measured

and translated into melting rates, but the relevant ice  $O_2$  concentration, as well as the fraction of the measured heat flux that is conducted up into the ice rather than melting it, must be known to accurately calculate the associated  $O_2$  flux.

The release of melt or brine flows may also cause stratification immediately below the ice and therefore a careful examination of the state of turbulence and mixing below the ice-water interface is required. The eddy correlation technique assumes that the dominant form of vertical transport is turbulent mixing. Therefore, the technique may produce inaccurate results at very low current velocities when there is also insufficient turbulence. Ice freeze and melt may also cause convection to occur, which has been reported as a problem for measuring  $O_2$  fluxes from profiles generated with microelectrodes (Glud et al. 2002, McMinn et al. 2010). However, with the eddy correlation technique these convective processes are included in measurements, and with the concurrent determination of ice melt rates we can estimate the net  $O_2$  flux due to primary production and respiration.

The lack of vertical mixing under low-flow conditions allowed density stratification to build up immediately below the ice due to ice melt (Fig. 2). This stratification caused the effects of the flux to be confined within the stratified layer near the ice, as evidenced by the large pulse in the signal when the stratification was later eroded (Fig 2). As a result, accurate fluxes could only be derived when the vertical mixing due to turbulent flow was strong enough to erode and prevent density stratifications. The mean current velocity provided a benchmark for determining when stratification would occur, and this was further evaluated by examining the cumulative

flux, as little or no flux was recorded during periods of weak turbulence, while stable and linear cumulative fluxes were derived during periods of well-developed turbulence (Fig. 2). The presence of well-developed turbulence was also examined through the spectra of the vertical velocity and the O<sub>2</sub> concentration (Fig. 3A and 3B). The presence of the inertial sub-range with a characteristic  $-5/3$  slope is indicative of well-developed turbulence (Kundu and Cohen 2008). The cospectrum of the vertical velocity and O<sub>2</sub> concentration was also examined to determine the frequency of the turbulent eddies that contributed to the flux. The example shown in Fig. 3C indicated that the contributing eddies had frequencies less than 0.1 Hz, and that larger eddies, with a significant portion below the initial sub-range, were responsible for the vertical transport.

An examination of the eddy diffusivities (Fig. 10) revealed that the turbulent mixing below the ice was clearly anisotropic as expected in flows near solid boundaries. The relatively small ratio between the longitudinal ( $E_x$ ) and vertical ( $E_z$ ) eddy diffusivity of 6:1 suggests that the water column was fully mixed, at least within the upper meters below the ice-water interface. For comparison, a ratio of 12:1 was found for a 1 m deep river that was fully vertically mixed (Berg et al. 2007). If stratification had been present under the ice it would reduce the vertical mixing and therefore give a much larger ratio. However, we stress that both the strength and depth of the density stratification are highly dynamic properties that change across time, and that intermittent low-flow conditions represent a challenge for eddy correlation measurements across the ice-water interface.

The footprint of the eddy correlation technique (Fig. 9), defined as the area from which the flux is obtained, is very large compared to that of other flux methods (Berg et al. 2007) and is expected to integrate most variability commonly observed at the ice-water interface (McMinn and Ashworth 1998, Rysgaard et al. 2001). It has been suggested that to include all horizontal variations in light, algal biomass and algal activity it is necessary to measure across distances of 20 to 100 m as dictated by variations in light availability below melting ponds and snow drifts (Gosselin et al. 1986, Rysgaard et al. 2001, Sørensen et al. 2010). Figure 9 shows the size of the footprint to be over 60 m long, and therefore it integrates over most of this variability. However, given the narrow width of the footprint its composition will change with even a small change in current direction. This variability can easily be investigated by examining the correlations between the fluxes and the current direction, and in this study none were found ( $R^2 = 0.021$ ,  $n = 166$ ).

Given the small difference between the mean seawater temperature and its freezing point, low rates of ice melt were expected. Throughout the study period low ice melt was observed (Fig. 8), and the measured  $O_2$  exchange rates indicated a net consumption of  $O_2$  (Fig. 5), which represent both the consumption by organisms and to a lesser degree the melting of deoxygenated ice crystals (Glud et al. 2002, Rysgaard and Glud 2004). Specifically, the  $O_2$  flux associated with ice melting was shown to be less than 13% of the average daily respiration rate (see Fig. 5 and 8). This calculated potential  $O_2$  flux due to melting assumes that all of the heat flux results in ice melting and that melt water is anoxic. The  $O_2$  concentration of water released during melting remains

an uncertainty, especially considering that brine channels may advect O<sub>2</sub> depleted or enriched water from anywhere within the ice. The ice also had a significantly lower temperature than that of the water column (McGinnis et al. in progress) and therefore the conduction of heat into the colder ice likely accounted for some heat flux without causing melt. Considering these uncertainties we were only able to put an upper limit on how much ice melt could affect the total O<sub>2</sub> flux. Thus, this maximum O<sub>2</sub> flux due to ice melt rates cannot account for any significant differences in fluxes during the study period. However, it is expected that physical processes during rapid ice growth and melting during other periods of the year may greatly affect the O<sub>2</sub> exchange and could potentially exceed the biological contribution.

The O<sub>2</sub> flux showed a strong correlation to light (Fig. 5) as GPP reduced the net flux of O<sub>2</sub> toward the ice during the day. However, at all times the ice was net heterotrophic, which has been observed by others (Rysgaard and Glud 2004, Rysgaard et al. 2008). The calculation of GPP uses the standard convention that the daytime and nighttime respiration rates are equal, as it is not possible to separate the two. However, this may lead to an underestimate of daytime respiration due to the stimulation of respiration by the release of photosynthates (Fenchel and Glud 2000, Glud et al. 2009).

The P/I curve established through model fitting (Fig. 5 and 6) revealed that the ice algae were well adapted to low light conditions with an  $I_k$  of about 4  $\mu\text{mol photons m}^{-2} \text{s}^{-1}$ . This is supported by many other studies that show sea-ice algae to be low-light adapted with values of  $I_k$  between 0.5 and 35  $\mu\text{mol photons m}^{-2} \text{s}^{-1}$  (Cota 1985, Kuhl et al. 2001, Rysgaard et al. 2001). Based on continuously measured light levels under the ice



and the  $I_k$  value, the primary producers appear to be light saturated for 75 % of the day below the snow-covered ice. From the PAR measurements and the model fit to the derived  $O_2$  fluxes (Fig. 5,  $R^2 = 0.923$ ) it was possible to estimate the net  $O_2$  flux throughout several days including periods of insufficient turbulent mixing (Fig. 7). Because the primary producers were light saturated for most of the day, other variables could potentially control ice algae production. Gradingier (2009) found that nutrients were the major limiting factors for sea-ice algae production while others suggest that transient photoinhibition could occur at higher PAR levels (Kuhl et al. 2001, Rysgaard et al. 2001) or that high salinities may reduce primary production (Mock and Gradingier 1999, Mock et al. 2003, Manes and Gradingier 2009).

Our GPP rates are supported by three recent studies at comparable sites in southwest Greenland by Mikkelsen et al. (2008), Sogaard et al. (2010), and Sogaard et al. (in preparation) who estimated maximum GPP rates using the  $^{14}C$  tracer method. The first two studies were conducted in March through April and the third was conducted parallel with our eddy correlation measurements at a location approximately 100 m away from the eddy correlation site. The  $^{14}C$  method is drastically different from the eddy correlation technique because the ice is disturbed by melting the ice cores, the cores cover a much smaller and different ice area, and they are incubated ex situ for a specific time period. However, all three studies gave similar maximum GPP rates of 1.75, 1.39, and 1.46 mmol  $O_2$  m $^{-2}$  d $^{-1}$  (assuming a 1:1 ratio of C: $O_2$  for comparison purposes), respectively, which compared surprisingly well with our estimate of 1.76 mmol  $O_2$  m $^{-2}$  d $^{-1}$ . The average GPP rates in March varied between the studies from 0.07 mmol  $O_2$

$\text{m}^{-2} \text{d}^{-1}$  (Søgaard et al. 2010) to  $1.75 \text{ mmol O}_2 \text{ m}^{-2} \text{d}^{-1}$  (Mikkelsen et al. 2008) and our measurement of average GPP falls within this range ( $0.69 \text{ mmol O}_2 \text{ m}^{-2} \text{d}^{-1}$ ). However, the average GPP rate determined at the same time and location by Søgaard et al. (in preparation) of  $0.30 \text{ mmol O}_2 \text{ m}^{-2} \text{d}^{-1}$  was lower than our rate. Given the differences in methods we are not surprised by these differences in the results; a point that is further confirmed by bacterial production rates by Søgaard et al. (2010) and Søgaard et al. (in preparation) using the  $^3\text{H}$  thymidine incorporation method. The estimated respiration rates from  $^3\text{H}$  thymidine incubations, which exclude microalgal respiration and involve a number of other assumptions that vary significantly in the literature (see Søgaard et al. 2010), of  $-0.16$  and  $-0.21 \text{ mmol O}_2 \text{ m}^{-2} \text{d}^{-1}$ , respectively, were an order of magnitude less than the respiration rate of  $-2.13 \text{ mmol O}_2 \text{ m}^{-2} \text{d}^{-1}$  we found. We believe that these rates are highly dependent on the method used and that to some degree the differences are caused by the intrusive nature of slurry incubations in altering important parameters such as  $\text{O}_2$ , nutrients, and salinity and their distributions within the ice. Furthermore, tracer incubations and eddy correlation may integrate the activity of different sections of the sea-ice and are conducted over different time scales. These differences need further investigation as they have significant implications for determining carbon turn-over in sea-ice.

In summary, the combined temperature and  $\text{O}_2$  eddy correlation flux measurements made it possible to evaluate and separate  $\text{O}_2$  exchange rates at the ice-water interface due to biological production and respiration from that caused by melting. In the future these rates may be further elucidated by eddy correlation salt fluxes for

which fast and reliable sensors are available. We see eddy correlation measurements as an important tool in future studies of sea-ice metabolism as it represents the closest we can currently come to truly in situ measurements.

### **Acknowledgments**

This study received financial support from the Danish Agency for Science, Technology and Innovation; the Canada Excellence Research Chair (CERC) program; and the National Science Foundation, Chemical Oceanography, grant OCE-0536431. The study is a part of the Greenland Climate Research Center's activities (GCRC6507).

### Literature Cited

- Arrigo, K. R. Primary Production in Sea Ice. In: Sea Ice, An Introduction to its Physics, Chemistry and Biology. Eds. D. N. Thomas and G. S. Dieckmann. Blackwell Publishing, Oxford 402 pp, 2003.
- Berg, P., H. Roy, F. Janssen, V. Meyer, B.B. Jorgensen, M. Huettel, and D. de Beer. Oxygen uptake by aquatic sediments measured with a novel non-invasive eddy correlation technique. *Mar. Ecol. Prog. Ser.* 261: 75-83, 2003.
- Berg, P., H. Roy and P.L. Wiberg. Eddy correlation flux measurements: The sediment surface area that contributes to the flux. *Limnol. Oceanogr.* 52: 1672-1684, 2007.
- Berg, P. and M. Huettel. Monitoring the seafloor using the noninvasive eddy correlation technique. *Oceanography* 21: 164-167, 2008.
- Berg, P, R.N. Glud, A. Hume, H. Stahl, K. Oguri, V. Meyer and H. Kitazato. Eddy correlation measurements of oxygen uptake in deep ocean sediments. *Limnol. Oceanogr. Meth.* 7: 576-584, 2009.
- Brand, A., D.F. McGinnis, B. Wehrli, and A. Wuest. Intermittent oxygen flux from the interior into the bottom boundary of lakes as observed by eddy correlation. *Limnol. Oceanogr.* 53: 1997-2006, 2008.
- Cole, J.J., M.L. Pace, S.R. Carpenter, and J.F. Kitchell. Persistence of net heterotrophy in lakes during nutrient addition and food web manipulations. *Limnol. Oceanogr.* 45: 1718-1730, 2000.
- Cota, G.F. 1985. Photoadaptation of high Arctic ice algae. *Nature* 315: 219-222.

- Crusius, J., P. Berg, D.J. Koopmans, and L. Erban. Eddy correlation measurements of submarine groundwater discharge. *Mar. Chem.* 109: 77-85, 2008.
- Eicken, H. From the microscopic, to the macroscopic, to the regional scale: Growth, microstructure and properties of sea ice. In: *Sea Ice, An Introduction to its Physics, Chemistry and Biology*. Eds. D. N. Thomas and G. S. Dieckmann. Blackwell Publishing, Oxford 402 pp, 2003.
- Fenchel, T., and R.N. Glud. Benthic primary production and O<sub>2</sub>-CO<sub>2</sub> dynamics in a shallow-water sediment: spatial and temporal heterogeneity. *Ophelia* 53: 159-171, 2000.
- Fofonoff, N., and R. Millard. Algorithm for computation of fundamental properties of seawater, UNESCO Technical Papers in Marine Science, No. 44, 1983.
- Glud, R.N., S. Rysgaard, and M. Kuhl. A laboratory study on O<sub>2</sub> dynamics and photosynthesis in ice algal communities: Quantification by microsensors, O<sub>2</sub> exchange rates, <sup>14</sup>C incubations and a PAM fluorometer. *Aquat. Microb. Ecol.* 27: 301-311, 2002.
- Glud, R.N., J. Woelfel, U. Karsten, M. Kuhl, and S. Rysgaard. Benthic microalgal production in the Arctic: Applied methods and status of the current database. *Bot. Mar.* 52: 559-571, 2009.
- Glud, R.N., P. Berg, A. Hume, P. Batty, M.E. Blicher, K. Lennert, S. Rysgaard. Benthic oxygen exchange across hard-bottom substrates quantified by eddy correlation in a sub-Arctic fjord. *Mar. Ecol. Prog. Ser.* 417: 1-12, 2010.

- Gosselin M, Legendre L, Therriault J-C, Demers S, Rochet M. Physical control of the horizontal patchiness of sea ice microalgae. *Mar. Ecol. Prog. Ser.* 29: 289–298, 1986.
- Gradinger, R. Sea-ice algae: Major contributions to primary production and algal biomass in the Chukchi and Beaufort Seas during May/June 2002. *Deep-Sea Res. II* 56: 1201-1212, 2009.
- Harvey, A.H. Properties of Ice and Supercooled Water In: *CRC Handbook of Chemistry and Physics* 92nd Edition. Lide, D.R. Ed. CRC Press. Boca Raton, FL. 2656 pp, 2010.
- Hume, A.C., P. Berg, and K.J. McGlathery. Dissolved oxygen fluxes and ecosystem metabolism in an eelgrass (*Zostera marina*) meadow measured with the eddy correlation technique. *Limnol. Oceanogr.* 56: 86-96, 2011.
- Kuhl, M. R.N. Glud, J. Borum, R. Roberts, and S. Rysgaard. Photosynthetic performance of surface-associated algae below sea ice as measured with a pulse amplitude-modulated (PAM) fluorometer on O<sub>2</sub> microsensors. *Mar. Ecol. Prog. Ser.* 223: 1-14, 2001.
- Kundu, P.K. and I, M.Cohen. *Fluid Mechanics*, 4th ed. Academic Press, 2008.
- Kuwae, T., K. Kamio, T. Inoue, E. Miyoshi, and Y. Uchiyama. Oxygen exchange flux between sediment and water in an intertidal sandflat, measured in-situ by the eddy-correlation method. *Mar. Ecol. Prog. Ser.* 307: 59-68, 2006.
- Lorrai, C. D.F. McGinnis, P. Berg, A. Brand. Application of oxygen eddy correlation in aquatic systems. *J. Atmos Oceanic Technol.* 27: 1533-1546, 2010.

- Manes, S.S. and R. Gradinger. Small scale vertical gradients of Arctic ice algal photophysiological properties. *Photosynth. Res.* 102: 53-66, 2009.
- McGinnis, D.F., P. Berg, A. Brand, C. Lorrai, T. Edmonds, and A. Wuest. Measurements of eddy correlation oxygen fluxes in shallow freshwaters: Towards routine applications and analysis. *Geophys. Res. Lett.* 35: 1-5, 2008.
- McMinn, A. and C. Ashworth. The use of oxygen microelectrodes to determine the net production by an Arctic sea ice algal community. *Antarctic Sci.* 10: 39-44, 1998.
- McMinn, A., K.G. Ryan, P.J. Ralph, and A. Pankowski. Spring sea ice photosynthesis, primary production and biomass distribution in eastern Antarctica, 2002-2004. *Mar. Biol.* 151: 985-995, 2007.
- McMinn, A. A. Pankowskii, C. Ashworth, R. Bhagooli, P. Ralph, and K. Ryan. In situ net primary productivity and photosynthesis of Antarctic sea ice algal, phytoplankton and benthic algal communities. *Mar. Biol.* 157: 1345-1356, 2010.
- McPhee, M. G. Turbulent heat flux in the upper ocean under sea ice. *J. Geophys. Res.* 97: 5365-5379, 1992.
- McPhee, M.G., J.H. Morison, and F. Nilsen. Revisiting heat and salt exchange at the ice-ocean interface: Ocean flux and modeling considerations. *J. Geophys. Res.* 113, 2008.
- Mikkelsen, D.M., S. Rysgaard, and R.N. Glud. Microbial composition and primary production in Arctic sea ice: A seasonal study from Kobbefjord (Kangerluarsunnguaq), West Greenland. *Mar. Ecol. Prog. Ser.* 368: 65-74, 2008.

- Mock, T. and R. Gradinger. Determination of Arctic ice algal production with a new in situ incubation technique. *Mar. Ecol. Prog. Ser.* 177: 15-26, 1999.
- Mock, T. M. Kruse, and G.S. Dieckmann. A new microcosm to investigate oxygen dynamics at the sea ice-water interface. *Aquat. Microb. Ecol.* 30: 197-205, 2003.
- Platt, T. C.L. Gallegos, and W.G. Harrison. Photoinhibition of photosynthesis in natural assemblages of marine phytoplankton. *J. Mar. Res.* 38: 687-701, 1980.
- Reimers, C.E., H. Tuba Ozkan-Haller, P. Berg, A. Devol. K. McCann-Grosvenor, and R.D. Sanders. Benthic oxygen consumptions rates during hypoxic conditions on the Oregon continental shelf: Evaluation of the eddy correlation method. *J. Geophys. Res.* 117: 1-18, 2012.
- Shirasawa, K., R.G. Ingram, and E.J.J. Hudier. Oceanic heat fluxes under thin sea ice in Saroma-ko Lagoon, Hokkaido, Japan. *J. Mar. Sys.* 11: 9-19, 1997.
- Smith, R.E.H., Anning, J., Clement, P. and G. Cota. Abundance and production of ice algae in Resolute Passage, Canadian Arctic. *Mar. Ecol. Prog. Ser.*, 48: 251-263, 1988.
- Søgaard, D.H., M. Kristensen, S. Rysgaard. R.N. Glud. P.J. Hansen, and K.M. Hilligsoe. Autotrophic and heterotrophic activity in Arctic first-year sea ice: Seasonal study from Malene Bight, SW Greenland. *Mar. Ecol. Prog. Ser.* 419: 31-45, 2010.
- Suzuki, Y., S. Kudoh, and M. Takahashi. Photosynthetic and respiratory characteristics of an Arctic ice algal community living in low light and low temperature conditions. *J. Mar. Syst.* 11: 111-121, 1997.



- Rysgaard, S., M. Kuhl, R.N. Glud, J.W. Hansen. Biomass, production and horizontal patchiness of sea ice algae in a high-Arctic fjord (Young Sound, NE Greenland). *Mar. Ecol. Prog. Ser.* 223: 15-26, 2001.
- Rysgaard, S., and R.N. Glud. Anaerobic N<sub>2</sub> production in Arctic sea ice. *Limnol. Oceanogr.* 49: 86-94, 2004.
- Rysgaard, S., R.N. Glud, M.K. Sej, M.E. Blicher, and H.J. Stahl. Denitrification activity and oxygen dynamics in Arctic sea ice. *Polar Biol.* 31: 527-537, 2008.
- Widell, K., I. Fer, and P. M. Haugan. Salt release from warming sea ice. *Geophys. Res. Lett.* 33. L12501, 2006.

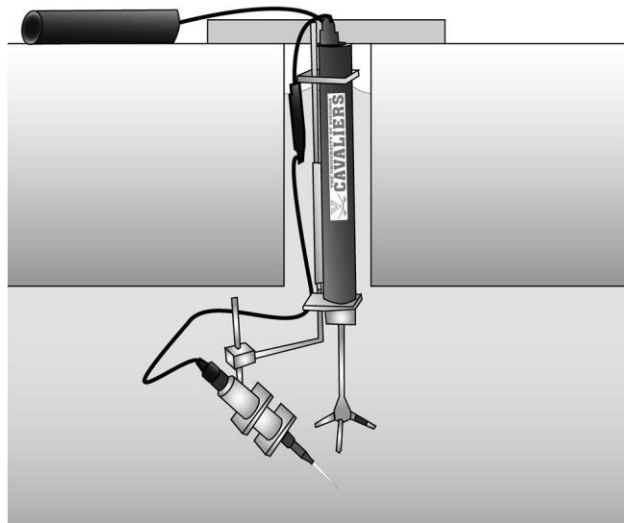


Figure 1. Eddy correlation instrument deployed under sea-ice through a rectangular-shaped hole and secured with a T bar at the ice-air interface. The instrument may freeze into the ice but the power supply (top left) and communication port (top center) remained accessible from above (image credit to Luke Cole).

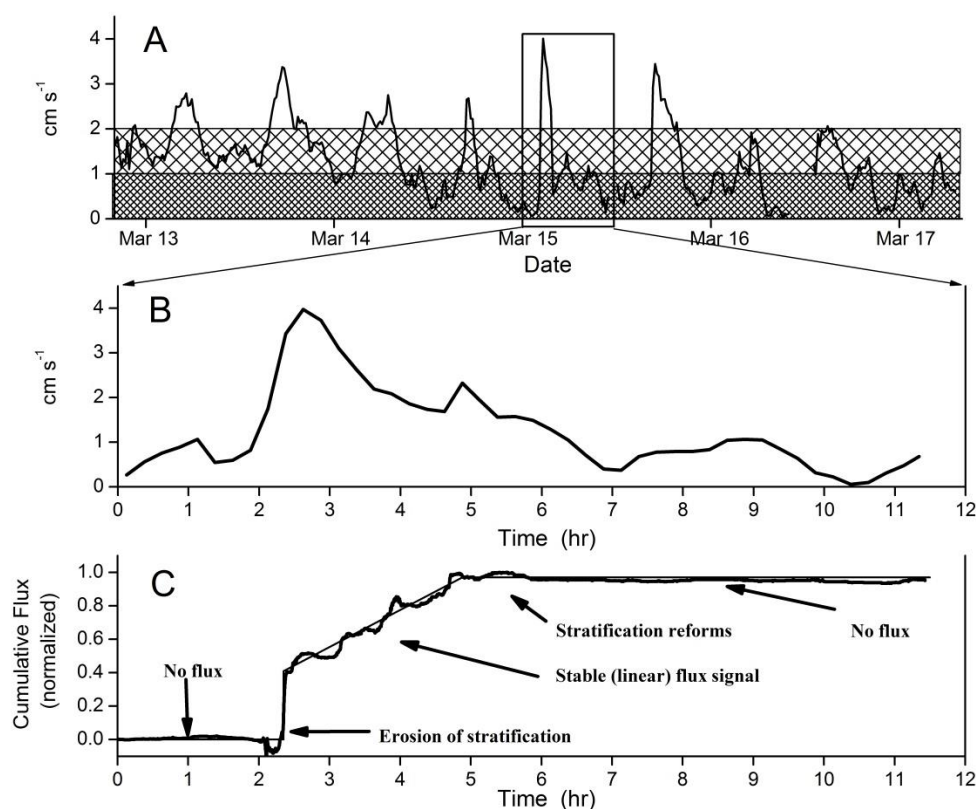


Figure 2. Fig. **A** shows the mean current velocity measured 22 cm below the ice-water interface over 4.5 d. The dark shaded region ( $< 1 \text{ cm s}^{-1}$ ) represents conditions where density stratification in the water column appeared to be persistently present while the lightly shaded region ( $1 - 2 \text{ cm s}^{-1}$ ) represents conditions where stratification was occasionally observed. The presence of stratification was evaluated by examining the mean velocity and the stability and linearity of the cumulative flux signal. Fig. **B** shows a 12 h segment of the velocity data in Fig. **A**. Fig. **C** shows that during this segment the flux signal was strongly dependent on current velocity. The magnitude of the vertical rise at hour 2.3, when stratification eroded due to an increase in velocity, was not indicative of any true flux and therefore was not included in the flux measurements.

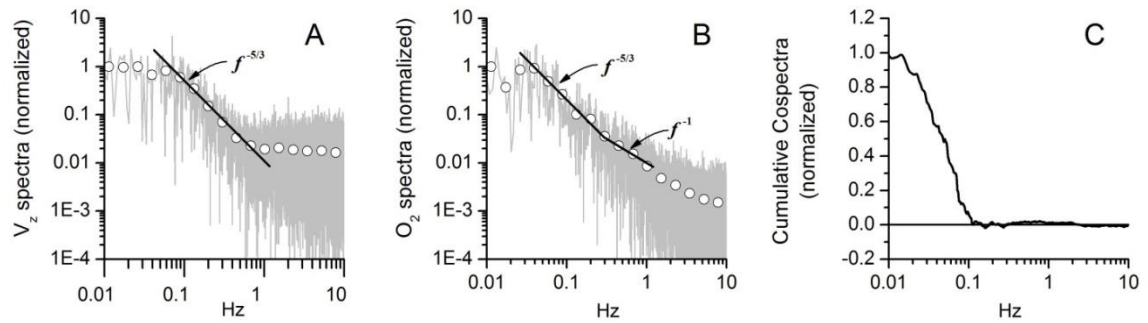


Figure 3. Typical spectra for current-driven turbulent flow under sea-ice (current velocity:  $1.86 \text{ cm s}^{-1}$ ). Fig. **A** and **B** show the normalized spectra of the vertical velocity and the  $O_2$  concentration, respectively. The  $-5/3$  slope is indicative of well-developed turbulence and represents the inertial subrange where inertial forces dominate transport, according to Kolmogorov's theory of turbulence. The  $-1$  slope at higher frequencies in the  $O_2$  spectrum indicates the transport of  $O_2$  by both viscous and convective forces. Fig. **C** shows the normalized cumulative cospectrum of vertical velocity and  $O_2$  and revealed that eddies with frequencies  $< \sim 0.1$  Hz contributed most of the vertical turbulence-driven  $O_2$  transport.

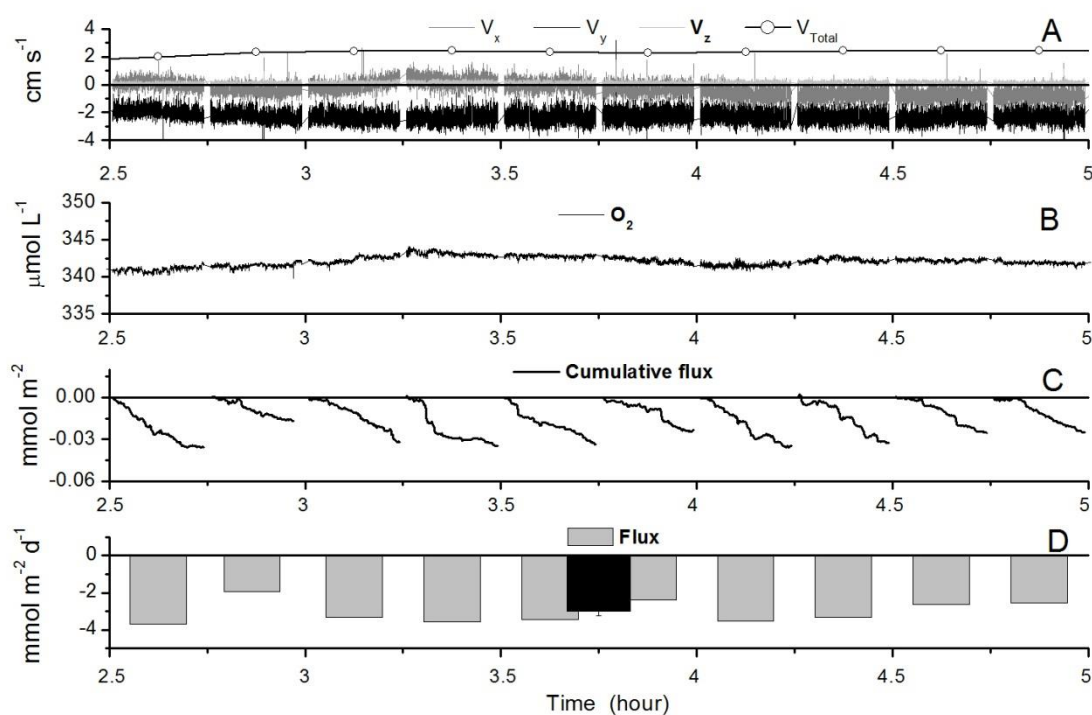


Figure 4. A typical example of eddy correlation data measured in 0.25 h segments 22 cm below the ice-water interface through 2.5 h. Fig. **A** shows the  $x$ ,  $y$ , and  $z$  components of the velocity at 16 Hz and the mean current velocity. Fig. **B** shows the corresponding  $\text{O}_2$  concentration at 16 Hz. Fig. **C** shows the cumulative flux calculated for each 0.25 h segment and Fig. **D** is the average  $\text{O}_2$  flux for each 0.25 h segment. A negative flux is a net flux of  $\text{O}_2$  towards the ice. The black bar is the  $\text{O}_2$  flux averaged across 2.5 h where the error bar represents the standard error.

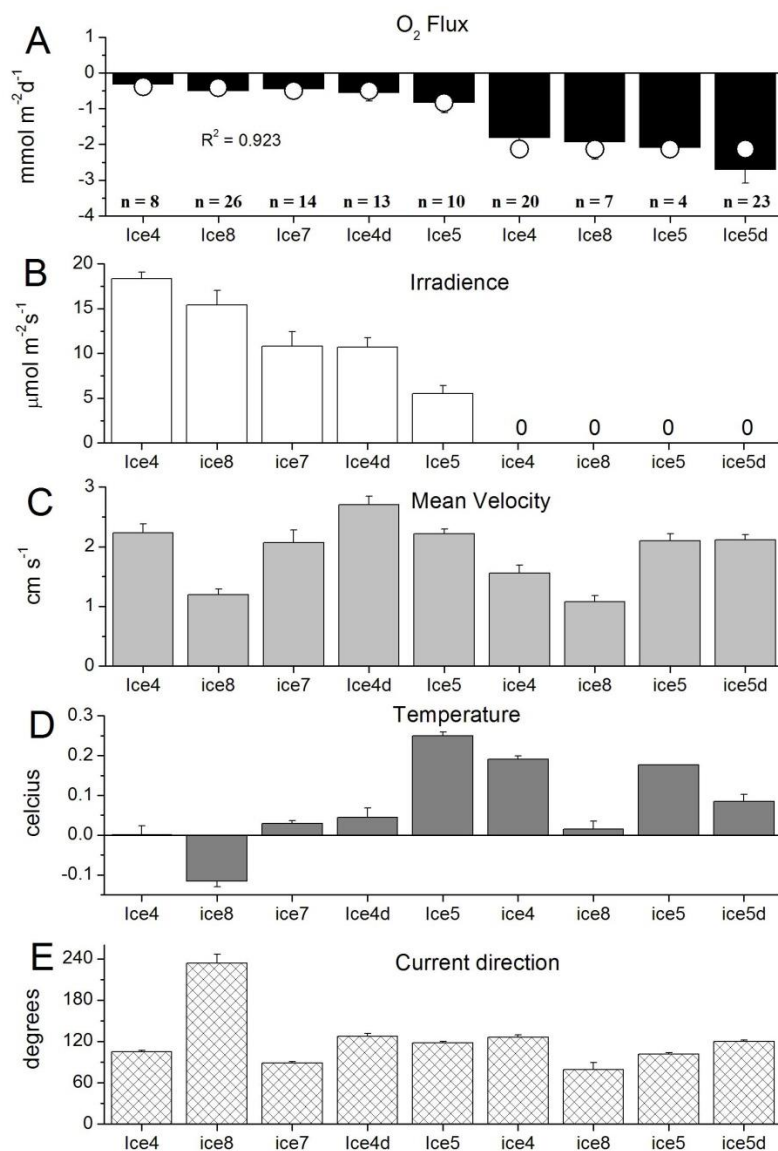


Figure 5. Averaged O<sub>2</sub> fluxes for periods with well-developed turbulence under the ice-water interface are shown in Fig. A, where  $n$  represents the number of 0.25 h data segments included in each average. The open circles in Fig. A represent the flux determined by fitting Eq. 3 and 4 simultaneously ( $R^2 = 0.923$ ) to the averaged fluxes. Figs. B, C, D, and E show the averages of under ice irradiance, mean current velocity, temperature and current angle over each period, respectively. All error bars represent standard errors.

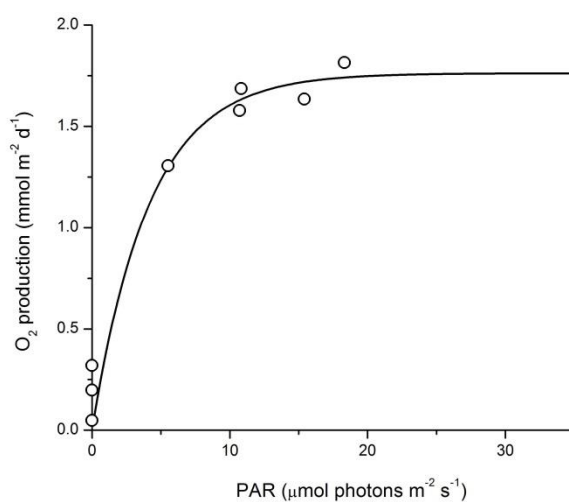


Figure 6. P/I curve calculated by fitting Eq. 3 and 4 simultaneously ( $R^2 = 0.923$ ) to the averaged O<sub>2</sub> fluxes in Fig. 5A. The open circles represent the GPP determined from the averaged fluxes in Fig. 5A. This P / I curve had an  $I_k$  value of 4.2  $\mu\text{mol photons m}^{-2} \text{s}^{-1}$  which represents the point where light saturation begins to occur.

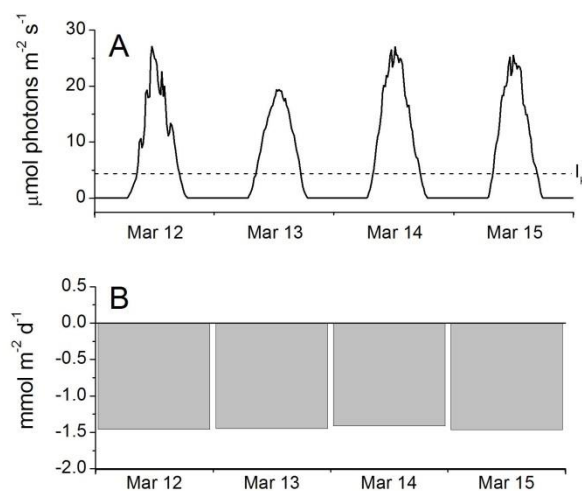


Figure 7. Fig. A shows four days of irradiance measured immediately below the sea-ice. The dashed line is the  $I_k$  value determined from the P/I curve and indicates that light saturation is present over much of the daylight hours. Fig. B shows the 24 h integrated  $\text{O}_2$  fluxes calculated from the irradiances in Fig. A and Eq. 3 and 4. The small variations between these daily  $\text{O}_2$  fluxes resulted from the ice algae being light saturated over most of the day.



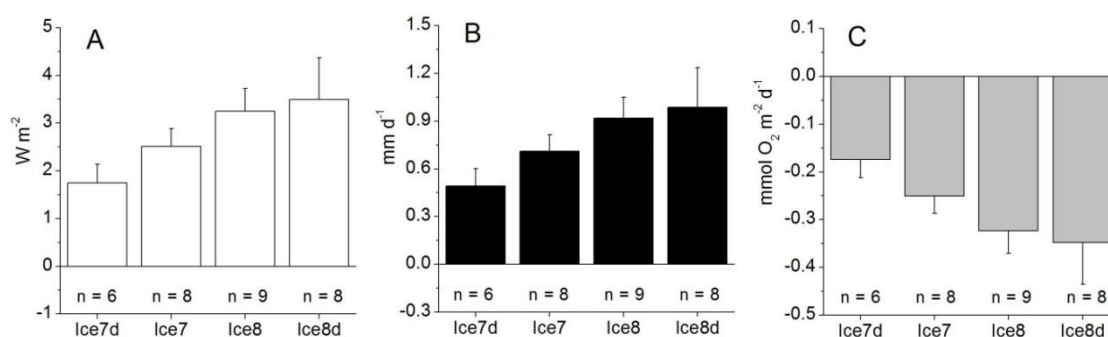


Figure 8. Fig. **A** shows the averaged heat fluxes for periods with well-developed turbulence under the ice-water interface. The maximum potential ice melt rate derived from the heat flux is shown in Fig. **B** and the maximum  $O_2$  flux calculated from this melt rate is shown in Fig. **C**. The  $n$  represents the number of 0.25 h measuring periods and error bars represent standard errors.

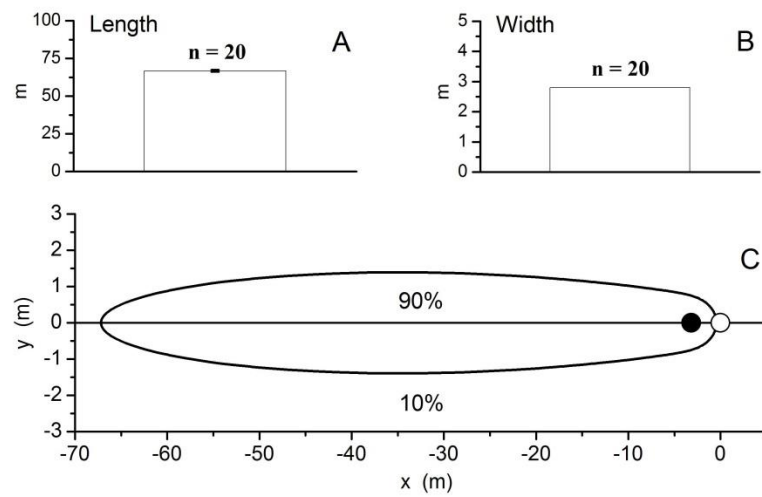


Figure 9. The estimated length, width and shape of the eddy correlation footprint are shown in Fig. **A**, **B**, and **C**, respectively. The error bars represent standard error and  $n$  represents the number of 0.25 h measuring periods. Fig. C shows the footprint or the area that contributes 90% of the flux (note the difference in axis scales). The open circle represents location of the eddy correlation instrument and the solid circle indicates the point of maximum flux contribution.

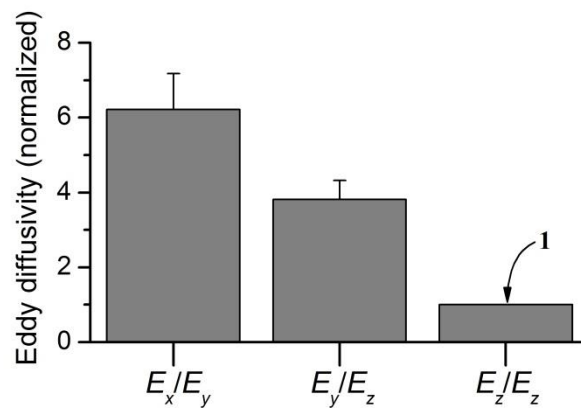


Figure 10. Level of anisotropy in the turbulent flow below the sea-ice, as reflected in the ratios between the eddy diffusivities ( $E_x$ ,  $E_y$ , and  $E_z$ ) in the  $x$ ,  $y$ , and  $z$  directions.